Doctoral Dissertation
Doctoral Program in Energy Engineering (35th Cycle)

Design and realization of a novel device for straightness measurement

Andrea Egidi
* * * * * *

Supervisor
Ing. Alessandro Balsamo

Politecnico di Torino
June 28, 2023

I hereby declare that, the contents and organisation of this dissertation constitute my own original work and does not compromise in any way the rights of third parties, including those relating to the security of personal data.

…….....

Andrea Egidi

Turin, June 28, 2023

Summary

The conceptualization of a novel technique aimed to straightness measurements and the practical realization of a mechanical device able to perform them without contact is presented. Such device –called InPlanT– is based on the acquisition of the luminous signal backscattered by a spherical dielectric target by means of a photodiode placed in the backward beam; the device proved capable of extracting the information about the lateral position of the target with respect to the onward beam. Three different prototypes were built, all of them based on the mechanical modulation of the signals retroreflected by the target. Suitable mathematical approaches to deal with the peculiar patterns of the signals (changing with the longitudinal distance of the sphere) were implemented, an acquisition procedure and a processing strategy of the data were implemented in order to extract the sought spatial information from them by means of a proper software expressly written. Quantitative evaluations –carried on with a statistical approach– of the factors affecting the accuracy of the measurements (primarily the jitter and the air turbulence, especially over large distances) were key to gain a better knowledge of the dynamics of the phenomena involved, and proper software adaptations to deal with these issues were applied.

The last versions of the device were preliminary tested on a high-accuracy CMM to evaluate their response in terms of maximum error of indication with respect to targets exploring a nearly perfect straight line in space. Experimental results showed that the achieved accuracy is better than ±2.1 μm within the measuring range of $\sim(0 \div 1.7)$ m. A straightness measurement on a simulated sinusoidal path was also performed, obtaining a peak-to-peak indication error of ±7 μm.

Acknowledgments

I would like to acknowledge Alessandro Balsamo for his invaluable mentorship over the last years, Marco Pisani for his precious suggestions about many theoretical and procedural aspects of this work and Davide Corona for his helpful experience in optomechanical setups.

I would like to dedicate this thesis to my beloved parents Giuseppe and Beatrice, and to my life partner Inna, for their love and support over the years.

Contents

List of Tables

List of Figures

Chapter 1

Straightness measurement in Large Volume Metrology

1.1 Introduction

Straightness – and its associated tolerance – is a feature that belongs to an ideal straight line, and characterizes a line extrapolated by an artifact (e.g. an edge, the intersection of an ideal plane or a section plane with the volume of a body, a median line etc.), when there is no need to explore its whole surface, or when sampling a large portion is unpractical; it is a form characteristic of a profile that can be extracted either from a surface by intersecting it with a reference plane (nominally orthogonal to the surface itself) or from a path in 3D space by projecting it onto a straightness plane: the first case is applied to material workpieces and standards, and it is an aspect investigated in inspections; the second case is crucial for machines, such as CMMs (coordinate measuring machines) and machine tools, since it contributes to their performance: a proper straightness of their guides ensures a good performance in their motion along their linear axes; its importance stems from the fact that, in mechanics, straightness (and other features too, of course, like flatness that is simply its extension to 3D space) evaluation of a workpiece helps to assess its conformity to some fundamental specifications. Emblematic cases can be found in industry both in manufacturing of products (like in machine tool control systems, where a tight tolerance in motion straightness is required in order to ensure a high machining quality and, consequently, a low percentage of discarded pieces), and in their inspection: the accuracy of a dimensional measurement carried on through coordinate measuring machines cannot indeed prescind from the goodness of the guideways' straightness).

Straightness error – whose tolerance zone is specified by the International Standard Organization (1) – is defined as the maximum orthogonal deviation with

respect to a reference straight line fitting the profile under examination: if a reference line is extrapolated in the assessment of a profile, the local straightness deviation Δs_l can be seen as the distance of each point of the studied profile from the chosen reference line, which should comply with the specificity of the straightness characterization; usual reference lines found both in literature and in common practice are minimum zone (MZ) and least-squares (LS) reference lines, but also the reference line passing through two points defining the profile extremes is also used, since this strategy is strictly reminiscent of the procedure of zeroing the instrument at the extremes of its stroke in a normal alignment process. The derived measured parameters – such as the peak-to-valley straightness deviation (STRt) or the root-mean-square straightness deviation (STRq) – quantify the total amount of deviation of the profile from ideal straightness.

The correct estimation of this particular class of form errors, together with the evaluation of other geometrical errors, allows to implement proper techniques of compensation both in machining and in measurement processes. The practical methods for straightness error measurement ordinarily rely on two basically different strategies: measuring the angle or measuring the length (2); this thesis work, after the description of the mathematical model formulated to apply the concepts of straightness error measurement to machine tools, explains the efforts carried on to design and build a device able to a contactless estimation of the straightness error of a linear path on the base of a totally new paradigm. A fundamental role in the assessment of form errors in general and, specifically, of the straightness error is played by the algorithm chosen to perform the calculation on the available dataset, traditionally based on least squares method or on minimum zone principle ((3), (4)), but also optimization algorithms (like the genetic algorithm (5) and particle optimization algorithm (6)) are recently gaining popularity.

The approach of measuring the angle is principally used to estimate the straightness of a rail, a guide or, generically, other artifacts; a common method relies on fixing a mirror on a square support which is in contact with the guide undergoing measurement: the tilts of the same mirror are evaluated by means of a fixed remote optical assembly, with the square continuously or in discrete steps scanning the profile; by analyzing the measured tilts it is possible to reconstruct the tilts of the surface, and consequently the straightness. Instruments based on angle sensors (7), autocollimators (8), angular interferometers ((2), (9)) are typically used in research applications and industry, but also a simple level (10) can fit the purpose. For what concerns optically machined surfaces, the same surface can function as a reflective mirror, leading to even greater precision in results; however, this particular circumstance is rarely applicable on a large scale (11). Also machine vision-based techniques are worth to be mentioned, and are gaining popularity (12).

Two main approaches to measure the straightness with reference to a machine moving along an ideally straight line are suitable: by reference to a material standard (13) or to a laser beam. The first approach relies on the installation of a straightness standard near the axis under investigation, and the distance between them is measured along the path by using dedicated sensors such as optical or

mechanical probes (14), capacitive sensors (15) or interferometric techniques. These procedures are eventually affected by the accuracy of the straightness standard and of its calibration, resulting in a mix of contributions due both to the imperfection of the measuring machine and to the artifact to be measured; sometimes the combined straightness deviations can be separated by reversal technique (14). The use of a laser beam is in general the most practical, and is at the foundation of the presented work. One of the most common realizations consists in an interferometric arrangement where a Wollaston prism splits the incident beam along the measurement axis into two sub-measurement beams diverging by a small angle, impinge onto a pair of reflectors installed on the moving stage under test, travel back towards the Wollaston prism and interfere with each other; the interference fringes measure the optical path difference, and hence quantify the straightness (16). This technique is complex, expensive due to the high accuracy interferometric set up required, and is sensitive to yaw. Another approach is based on the estimation of the lateral displacement of the testing machine with respect to the center of mass of a laser beam; it is based on a certain type of detector (e.g. a CMOS camera, a 4-quadrant photodetector or a position sensitive device) connected to the machine capable of extracting the sought information on the transversal position of a representative portion of the laser beam (like the center of mass). Another strategy relies on the application of a retroreflector (17) on the moving machine, with a detector placed to the still machine component (18). Sometimes, when a high level of accuracy is required, the non-perfect straight nature of the laser beam should be accounted for, especially when air turbulence randomly influences the beam stability; likewise, a bending of the beam caused by an orthogonal gradient of the air refractivity should be evaluated, since it introduces a systematic effect in the measurement that needs to be compensated (19). To conclude this review, another technique is focused on the evaluation of transverse acceleration while the axis is moving at constant speed (20).

Independently on the peculiar approach used to manage the obtained data, the algorithm used to infer the sought information on straightness is a key factor for the success of the whole measurement process. The results of the work described in this thesis arise from the application of a custom algorithm that converts the phase information of a laser beam retroreflected by a special target (sampling the signal in a grid of aligned points) into a spatial information; after a proper calibration, the obtained datum is subsequently translated into the sought straightness error of the trajectory followed by the same target with respect to the reference beam (propagating along a “perfect” straight line) impinging on target itself.

1.2 Background and motivation

Large Volume Metrology (LVM) – the ability of measuring size, shape, location and orientation of large objects, assemblies or machine tools – has a key role in many fields involving advanced technology and engineering, manufacturing

and scientific research. Several issues had recently been spotted requiring significant improvements: geometric inspection in production technology (in accordance with geometrical product specifications - GPS), new techniques for the simultaneous measurement of multiple targets with accuracy better than photogrammetry, need for traceability in absolute distance meters, how to guarantee a proper compensation of refractive index (responsible for bending effects in laser propagation), how to achieve better compensation for thermal expansion/contraction in presence of temperatures different from standard, dynamic acquisition of target positions, and so on. LVM also plays a role in several critical processes of alignment in such facilities as CERN and ESRF, in surveying industries, in automotive and aeronautics factories, often in non-cooperative environment, where optical techniques relying on the use of electromagnetic beams propagating in ambient air; however, these techniques generally suffer from lack of proper traceability to primary standards of length, and the difficulty of estimation of measurement uncertainties often constitute a limit to a large-scale diffusion and applicability. LVM technologies are vital in several industrial contexts, where the items to be measured or aligned are so bulky in size that they cannot fit with conventional measuring machines, nor their transportation to a laboratory is viable due to their mass or because they are part of an infrastructure: this means that these items necessarily need to be measured *in situ*, requiring complex strategies to be implemented in order to satisfy the metrological needs which arise from time to time. Nowadays, novel system are required to be engineered to be a compromise between costly yet precise laser trackers and more affordable yet less precise photogrammetry, alongside an ongoing requirement for highly accurate and traceable large-scale references (such as telemeters) for increasingly expansive photogrammetry networks. This will facilitate broader adoption of LVM by small and medium-sized enterprises (SMEs), resulting in new applications; the expressed requests involve the need for extra innovative LVM instruments relying on unconventional and/or affordable sensors and methodologies to address the continuously growing range of end user situations, such as enhanced precision photogrammetry, and three-dimensional coordinates measurement over extended distances, to be exploited in harsh conditions.

As stated by the International Federation of Robotics and the IEEE Robotics and Automation Society, real-time feedback is an essential necessity for complex manufacturing tasks, like robotic drilling machines that require precise measurement across extensive volumes. Present large-scale factory measurement networks, for example those based on iGPS, lack the necessary level of accuracy. On the other hand, local solutions based on laser trackers are either too costly or too slow. Moreover, there is a lack of integration between localized and factory-wide metrology, hindering the seamless transition between different measurement devices during the manufacturing process. In order to achieve autonomous and efficient production, it is crucial to integrate various layers of measurement systems that vary in range, speed, accuracy, and cost per target. This combination of integrated and diverse LVM systems enables the control system to oversee the

entire production or assembly process, allowing flexibility in robot positioning and part placement based on measured data. These requirements align with the concepts of a "smart factory," "factory of the future," or "industry 4.0." However, for such applications, there is currently no standardized and procedural method to estimate uncertainty. Simply querying a measurement device for uncertainty estimates based on the device model is not feasible.

The need for improved geometrical performance in machining large parts can be divided into two aspects: firstly, the challenging task of determining the error map of a large machine tool, which is essential for compensating for geometrical errors; secondly, the verification of machine performance during production. Large machine tools fall outside the scope of classical Coordinate Measuring Machine (CMM) systems, where laser error mapping is feasible, and do not fit into the realm of true large volume metrology (ranging in tens or hundreds of meters). Measuring volumes of, for example, (6 × 3 × 2) m^3 require error mapping and compensation, along with the need for high-speed metrology checks during production cycles (within maximum cycle times of 20 to 40 seconds). Achievable accuracy is at the limit (100 μm) in such applications, and it poses significant challenges in terms of traceability and testing. While research exists for small machine tools, the same level of investigation is lacking for very large tools and certainly not readily available.

1.3 InPlanT: the conceptual starting point

The work described in this thesis drew inspiration from EMPR project IND53 LUMINAR (21), and in its context several new tools and facilities were developed, tested and demonstrated in a live factory environment at Airbus (Filton, UK). In that project, INRIM had developed a device (whose acronym is “InPlanT” – Intersecting Planes Technique – (22)) to measure the spatial coordinates of a spherical retroreflector contactless in harsh conditions, such as aerospace and automotive industry (Figure 1). It relies on the idea that a point target in 3D space can be seen as the intersection of three non-parallel planes: the coordinates of the target, when using a Cartesian coordinate system, are the Cartesian triad expressing the positions of the mutually orthogonal planes.

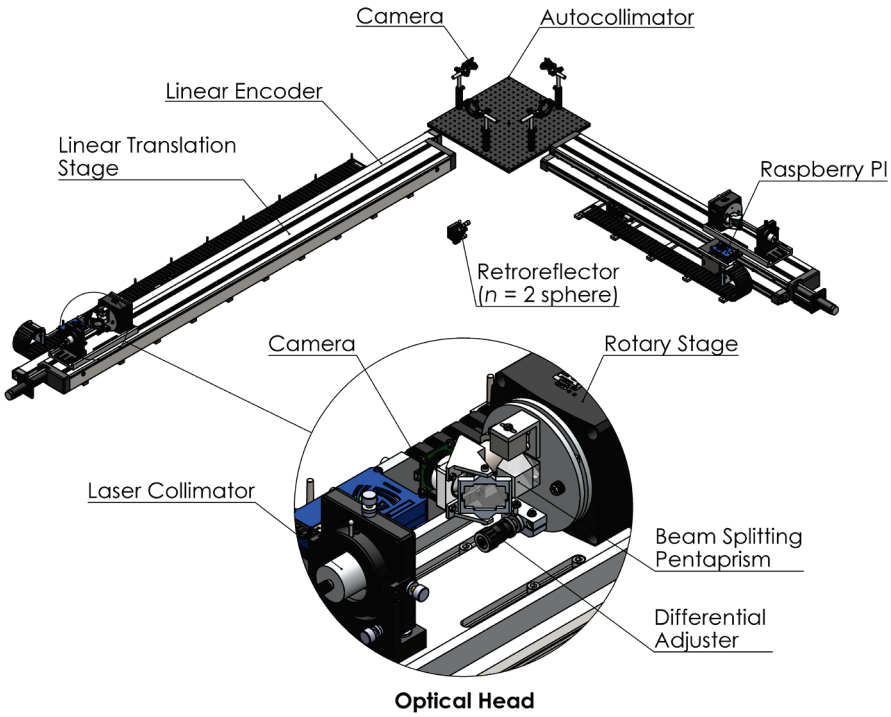

Figure 1. CAD design of measurement axes.

For each coordinate axis, an independent device realized an orthogonal optical coordinate plane through the retroreflecting target. The two degrees of freedom necessary for the tracking are realized by a linear and a rotary stage; the former effectively measures one coordinate of the target. The coordinate of the coordinated plane was then one of the sought target coordinates. This was measured by the linear stage. The yaw and pitch errors of each moving carriage and the squareness error between axes were measured by a common autocollimator and compensated for. The beam of a laser is separated in two by a pentaprism mounted on a hollow rotary table. The reflected beam impinges on the target, and the retroreflected beam is observed by a camera. The passing beam is detected by an autocollimator at the end of the linear axis stroke, to detect yaw and pitch errors of the linear stage. In a 2D measurement, the autocollimator is common for the two axes to provide the squareness reference. Figure 2 and Figure 3 illustrate both the concept and working principle of the device.

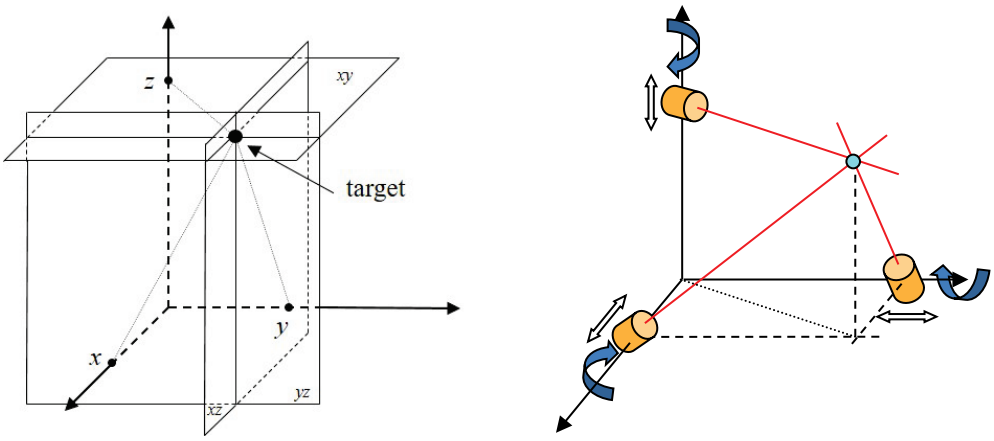

Figure 2. Concept of InPlanT (source: link)

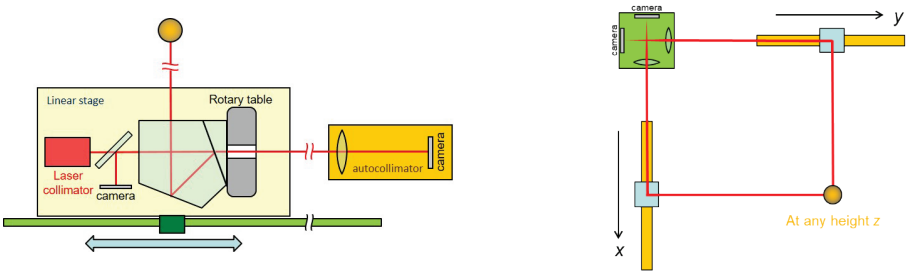

Figure 3. Working scheme of each InPlanT device.

Several designs of rotary light beam were considered: a beam source with tracking capability (like a laser tracer); a continuously tracking rotating stage; and a light blade, distributed in space (e.g. using a cylindrical lens or mirror). Preliminary tests settled on the second option of a tracking, rotating stage. This required further development in order to optimize both the beam launching and return beam detection arrangements – tests were performed using a pentaprism mounted onto a hard disk motor assembly with a four-quadrant detector for the return beam. A final design was arrived at, based on a commercial linear slideway onto which is mounted a carriage with commercial rotation stage which holds the pentaprism. Light is collimated onto the prism from a nearby lens source. In order to maintain orthogonality of the planes, and to compensate for pitch and yaw errors of the linear stages an assembly of crossed autocollimators was designed and aligned. These achieved a sensitivity of 12 microradians per pixel.

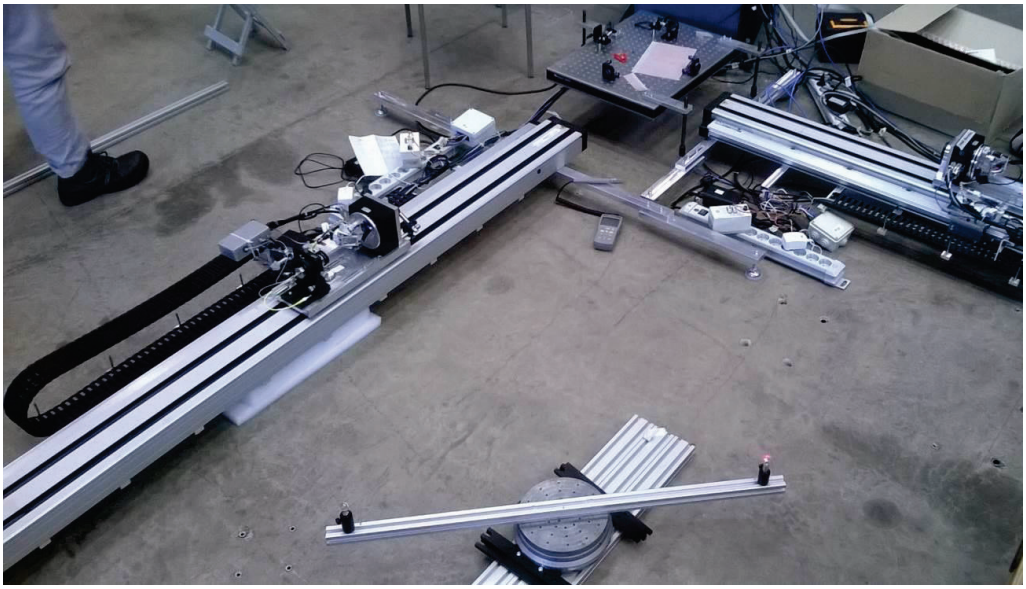

Figure 4. A 2D version of the INRIM InPlanT system tested at the Airbus facilities as two measuring axes (sliders, diagonal on left and right). The two axes are angularly linked by an orthogonal pair of autocollimators (rectangular table supporting the optics) (source: QMT Magazine, Spring 2017).

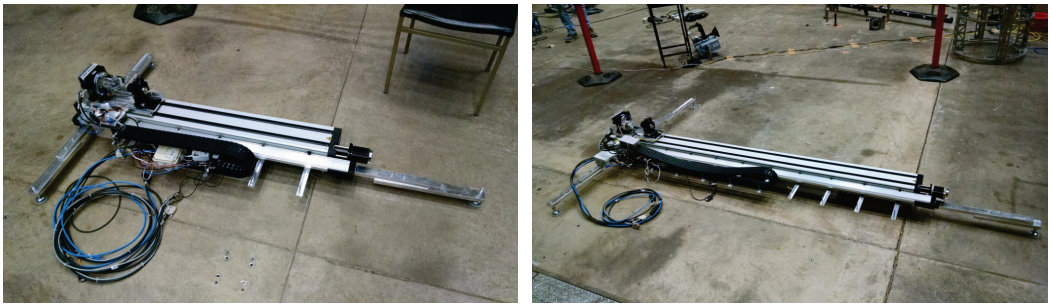

(a) (b)

Figure 5. Details of 1 m (a) and 2 m (b) strokes.

The images in Figure 4 and Figure 5 show the final pair of linear axes with their rotating carriages – the project budget was only sufficient to manufacture a two-axis prototype - the key elements of the design can be easily seen. A moving linear stage carries: a rotary table with rotation axis aligned to the measurement axis, a laser collimator (fed by a fibre) aligned to the rotation axis, a pentaprism attached to the rotary table which deflects the beam 90° regardless of its orientation. The beam impinges onto a retro-reflecting target and the returning beam is deflected back by the pentaprism and impinges through a beam splitter onto a camera. The camera sees the luminous image of the retro-reflecting sphere and the position of the sphere in the camera image drives: vertically, the rotary table; horizontally, the linear stage. When the image is centred – possible residuals are compensated –, the linear position is measured by a linear encoder and constitutes the sought coordinate

for that axis. The mechanical and optical systems were integrated by linking the rotary stage controller to a Raspberry Pi computer using Ethernet. The Pi also linked to the camera and the linear stage controllers using USB interfaces. A web server interface was used to provide user access to the system. Figure 6 and Figure 7 schematically illustrate the (hardware and software) architecture of the developed system.

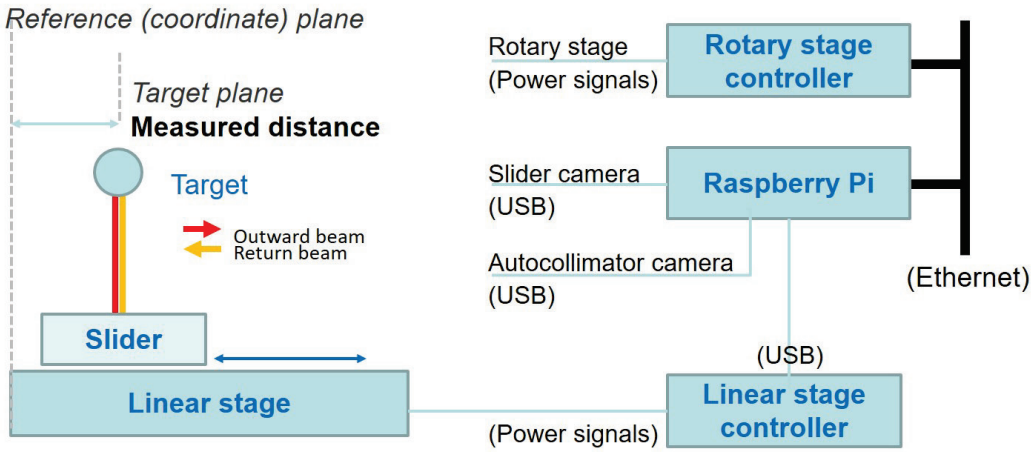

Figure 6. Hardware architecture of the prototype.

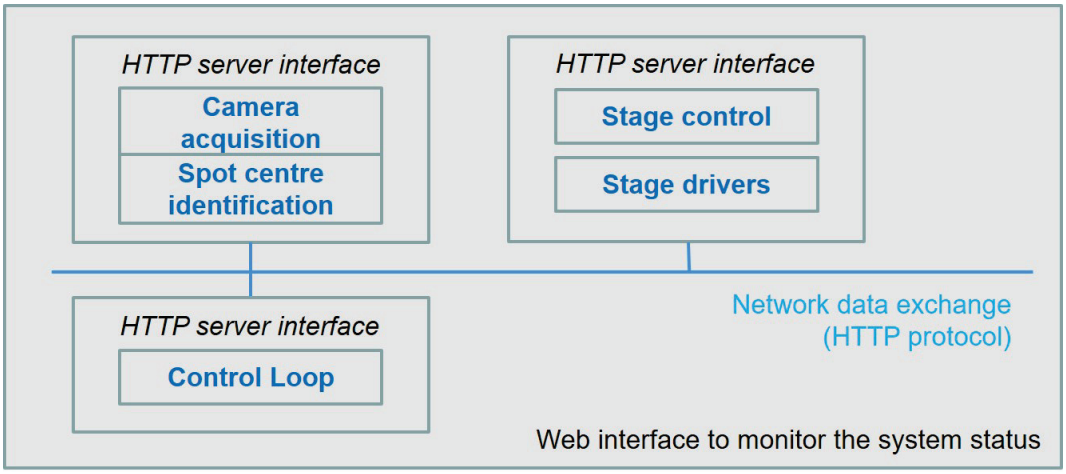

Figure 7. Software architecture of the prototype.

Testing in the laboratory at INRIM was completed very shortly before the transportation for the tests at Airbus. The pentaprism pose was adjusted on the rotary stage to obtain a residual angle of (111 ± 46) microradians. The squareness error was measured as 935 µm but was reduced down to 97 µm. The sensitivity of an axis system was demonstrated as 0.31 pixels/µm. For these prototypes, maximum tracking speed is about 1 cm/s because of limited control bandwidth (general purpose LabVIEW setup), however the residual error is below 25 µm when target is stopped. Granularity in position due to actuator step size is similarly 25 µm.

Linear position maximum tracking noise of around 10 µm at 7 m target range was demonstrated. In principle, to achieve a (10 × 10 × 5) m³ measuring volume, two 10 m and one 5 m axes were required. Due to the budget limitation, the project prototype was limited to two axes only, with strokes of 1 m and 2 m, respectively. Only the 2D coordinates of the projection of the target over a measuring plane could be measured at that moment, limited to an area of (1 × 2) m². However, measurements in a 3D space at full distance (e.g. at 10 m) were possible thanks to the mutual independence among axes. For the measurement campaign, a pre-calibrated ball-bar (of two $n = 2$ targets) was attached to a precision rotary indexing table, then the table was rotated to 8 different locations and in each location the two InPlanT axes were used to measure 2D coordinates of the two targets (Table 1). The resulting data were used for a data fit of the parameters (x_0, y_0) being the centre of the circle, and R_1 and R_2 being the radii of an ellipse (an ellipse was used rather than a circle to allow for non-planarity of the experiment) (Figure 8). Initial standard deviation of the fit was 276 µm using only the linear encoders on the axes, and this was improved to 45 µm by including the measured yaws & pitches of the axes' rails and thermal compensation of the rail distances (Figure 9).

Ball bar nominal length	500 mm
Rotation axis (*x*,*y*) coordinates	(450 mm, 450 mm)
No of angular positions	8+
No of points	19
No of outliers (discarded)	1
Temperature	(17.0 – 18.2) °C
Geometrical parameters to fit	(x_0, y_0, R_1, R_2) concentric fit

Table 1. Testing conditions for the InPlanT final experiment.

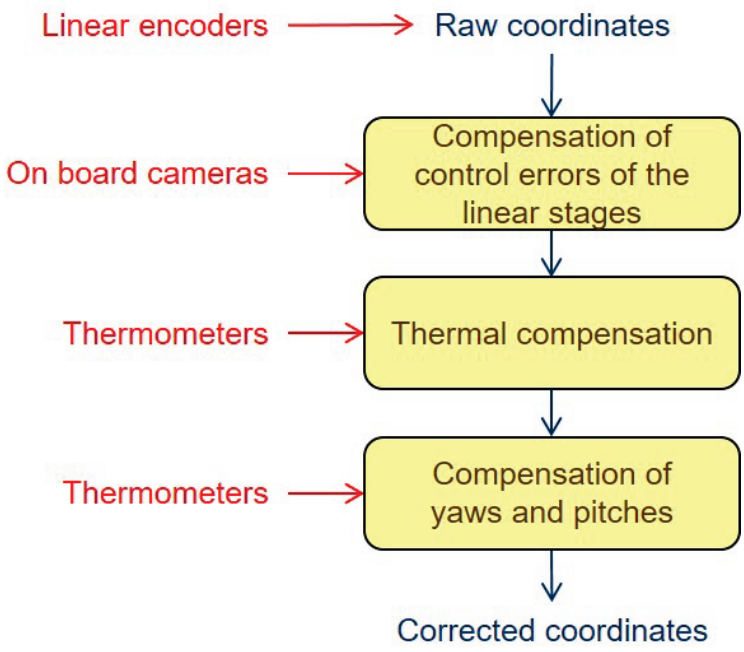

Figure 8. Strategy for the derivation of the results.

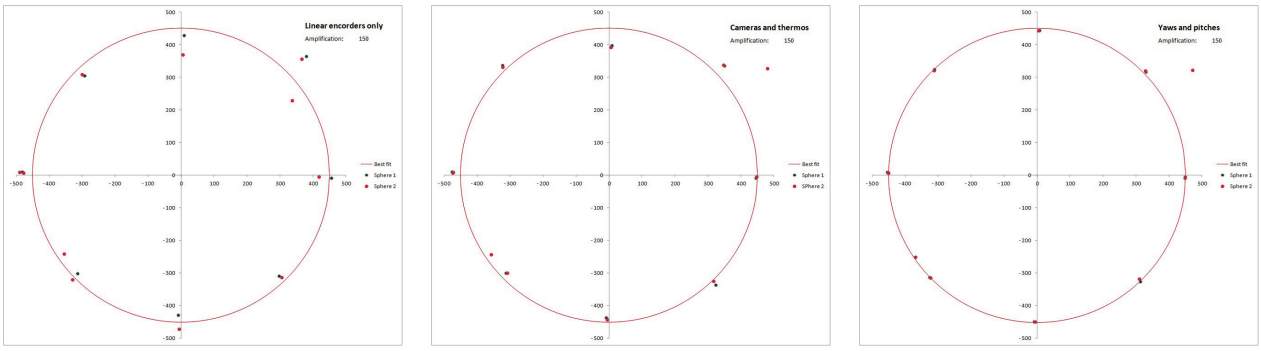

(a) (b) (c)

Figure 9. Results obtained in the experiment; (a): without any compensation (σ = 276 µm), (b): correcting with cameras and thermometer data (σ = 196 µm); (c): compensating for yaws and pitches (σ = 45 µm).

1.4 InPlanT concept applied to machine tools

LUMINAR project ended with encouraging results, and its follow-up project EMPIR-17IND03 “LaVA” (23) was at the base of this thesis work, whose intention was to apply the explored concepts and the gained experience to a real application field. The geometry error compensation of medium/large volume machine tools was identified as the target application. The axes of Cartesian machine tools are in fact precision linear stages. To implement the new InPlanT concept, the rotary table only had to be added as an additional device. The most suitable location to install

the rotary table at was initially identified at the machine tool ram, but afterwards it was recognized that a mechanical simplification was necessary and the device could be installed outside the working space of the machine tool, with just the target connected to the spindle (Figure 10).

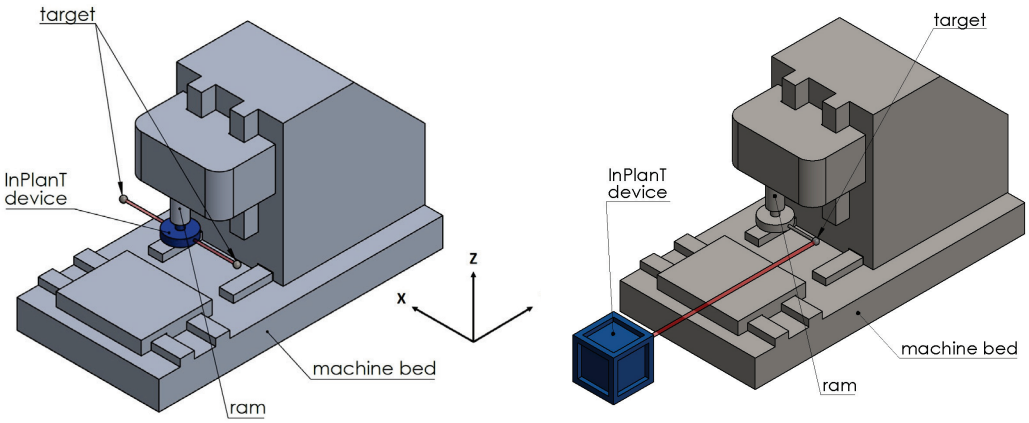

(a) (b)

Figure 10. Concepts of InPlanT applied to a machine tool.

Let's stay with the InPlanT implementation depicted in Figure 10 (a). As the device has sensitivity only along the rotary table axis, the rotary table had to be reoriented in subsequent measurements.

An important question about the application was: does a set of measurements carried out with such a device gather enough information to detect all machine tool geometry errors? Let us take an axis at a time; for illustration, let x be the stroke and let z be the alignment of the rotary table axis, coincident with the direction of sensitivity. Let us take two targets at the extremes of the x stroke, as depicted in Figure 10 (a); they can be illuminated by a rotation of 180° of the rotary table. The InPlanT device is effectively a zero detector with a limited measuring range. Its zero signal drives the machine tool to adjust its position finely. The extremely good measuring capability of the machine axes is then exploited to detect the position in space and eventually the geometry errors.

Two geometry errors give contributions in the direction of sensitivity, the x vertical straightness (t_{xz}) and pitch (r_{xy}). At each carriage coordinate, the former results in the same error at either opposite targets, while the latter in opposite errors, as a function of the current distance to the target (that is, the optical arms). By comparing the measurements of either targets, the two geometry errors can be separated. After 90° repositioning of the rotary table axis to align it to y axis (sensitivity along y), the same applies to the x horizontal straightness (t_{xy}) and the yaw (r_{xz}). Therefore, four geometry error functions of the x carriage (t_{xy}, t_{xz}, r_{xz}, r_{xy}) out of six can be derived. The remaining two are the roll r_{xx} and the scale error t_{xx}. The roll can be detected with the two targets at the same extreme of the x stroke, at the same z coordinate, but y separated as much as possible, that is, at the extremes of the measuring volume. The ram supporting the rotary table is moved along x at

the same z coordinate as the targets and at a y coordinate nominally mean of the targets. Again, each target can be illuminated with a proper rotation of the table. At any position of the carriage, three geometry error components give effects: the vertical straightness t_{xz}, the pitch r_{xy} and the roll r_{xx}. However, the former two are already known from the previous measurement and can be compensated for. In addition, their errors are equal at either target (or at least have the same sign), while that of the roll has opposite signs, and a direct separation is also possible.

InPlanT is admittedly unable to detect the scale error. In fact, the scale error has effect in the same direction of the stroke, whereas InPlanT has sensitivity in an orthogonal direction only. In addition, the scale errors are the link to the traceability to the SI unit, the metre. There is no calibrated standard of length or length measuring instrument in InPlanT, so the scale error cannot be derived through it. The scale error should be taken care of separately. This is not deemed as a major obstacle, as checking machine tools along their axes e.g. by an interferometer is common practice in industry (see (24)). Similar reasoning, set up and derivation of results is then applied in turn to the other machine axes, y and z.

What remains is the joint effect of the axes, the squarenesses. They are three angular values and can be easily derived separately after InPlanT compensation of all other geometry errors. Conventional techniques exist, such as the comparison of the measurement of a same length (either a gauge or an interferometric distance) when oriented on two diagonals of each coordinate plane. This is also common practice, particularly for Coordinate Measuring Machines (25).

The above reasoning is not necessarily mirrored by the experimental procedure; it is rather intended to provide confidence that the measurements convey enough information. In practice, measurement data taken along a set of measurement lines are collected and the geometry errors are derived by best fit adjustment to the data. In this view, the above reasoning proves that at least a possible set of data (that is, an experimental procedure) exists that makes the adjustment possible without encountering singularities and/or ill conditioning.

The adjustment of the geometry errors to the measurement data by best fitting required an error model. This section describes it. We may separate two constituent blocks: the rigid body model, which describes the geometry errors itself, and the procedural model, which mirrors the measurement set up. The following subsections describe them separately.

1.4.1 The first error model for the InPlanT approach: the rigid body error model

The machine tool error model is assumed to follow the conventional rigid body model (26), here reported in the formulation first given in (27) and then endorsed in (28):

$$\boldsymbol{e} = \boldsymbol{t}_x + \boldsymbol{t}_y + \boldsymbol{t}_z + \boldsymbol{r}_x \times \boldsymbol{h}_x + \boldsymbol{r}_y \times \boldsymbol{h}_y + \boldsymbol{r}_z \times \boldsymbol{h}_z, \tag{1}$$

where

$$\boldsymbol{t}_x = \begin{pmatrix} t_{xx} \\ t_{xy} \\ t_{xz} \end{pmatrix}, \boldsymbol{t}_y = \begin{pmatrix} t_{yx} \\ t_{yy} \\ t_{yz} \end{pmatrix}, \boldsymbol{t}_z = \begin{pmatrix} t_{zx} \\ t_{zy} \\ t_{zz} \end{pmatrix}, \boldsymbol{r}_x = \begin{pmatrix} r_{xx} \\ r_{xy} \\ r_{xz} \end{pmatrix}, \boldsymbol{r}_y = \begin{pmatrix} r_{yx} \\ r_{yy} \\ r_{yz} \end{pmatrix}, \boldsymbol{r}_z = \begin{pmatrix} r_{zx} \\ r_{zy} \\ r_{zz} \end{pmatrix} \tag{2}$$

are the 9 translational error functions *t*'s and the 9 rotational error functions *r*'s. The first subscript of each *t* or *r* indicates the pertaining axis and the second the orientation of the error: the direction of translation for translational ones, or the rotation axis for rotational ones. For example, t_{xy} is the translation along y of the *x* carriage, and r_{yz} is the rotation about *z* of the *y* carriage[1].

$\boldsymbol{h}_x$, $\boldsymbol{h}_y$, $\boldsymbol{h}_z$ in equation (1) are referred to as the *effective Abbe arms*, i.e. the arms that transform rotations to translations, while × indicates the cross product. Due to the seriality of the machine kinematic, the expression of the effective Abbe arms is not the same for all axes:

$$\boldsymbol{h_x} = \begin{pmatrix} p_x \\ p_y + s_y \\ p_z + s_z \end{pmatrix}, \boldsymbol{h_y} = \begin{pmatrix} p_x \\ p_y \\ p_z + s_z \end{pmatrix}, \boldsymbol{h_z} = \begin{pmatrix} p_x \\ p_y \\ p_z \end{pmatrix} \tag{3}$$

where $\boldsymbol{p}$ (and its components p_x, p_y, p_z) is the probe offset[2], and $\boldsymbol{s}$ (and its components s_x, s_y, s_z) is the machine scale readings. Equation (3) can be interpreted as follows. Let us consider the reference point attached on the ram when $\boldsymbol{s} = \boldsymbol{0}$, i.e. at homing[3]. Let us regard it as three coincident points, each attached to the *x*, *y*, *z* carriage, respectively. After the machine moves away from homing, the three points separate, each following its own carriage. The effective Abbe arm of an axis is the offset of the stylus tip/effective point to the point of that axis. The probe tip/effective point always keeps its position relative to the *z* reference point: the *z* effective Abbe arm is equal to the probe offset. Its position relative to the *y* reference point instead changes when the *z* axis slides: this introduces the term s_z in equation

[1] The ISO 230 1 (33) provides a different notation. For instance, t_{xy} is indicated as E_{YX} instead and r_{yz} as E_{BX}. The two notations have coincident meanings, including the positive directions. The notation above is used for reasons of tradition, as INRIM initiated the investigation of geometry error compensation many years ago (34) specifically for coordinate measuring machines (CMMs), for which no such standard existed at the time.

[2] The term *probe offset* is used to follow an established practice with CMMs. It is the vectorial displacement of the probe tip (for CMMs) or of the functional point ((33) § 3.4.2, for machine tools) from a reference point established on the ram.

[3] In some machines, the homing occurs at different values: $\boldsymbol{s} \neq \boldsymbol{0}$ at homing and the scale are preset to predefined values rather than reset. Regardless of this, a point in space exists where $\boldsymbol{s} = \boldsymbol{0}$. In some cases, this point cannot be reached, i.e. it is outside the measuring/working volume, e.g. the *z* axis is always negative. This is immaterial for what follows.

(3). Finally, its position relative to the x reference point changes when the y and z axes slide: this introduces the terms s_y and s_z in equation (3).

In conclusion, the geometry error model requires 18 error functions. Each one, in turn, requires a parametric description such as a tabular form with linear interpolation. The full set of parameters describing the 18 error functions constitutes the complete description of the geometry error, and is in fact the sought outcome of the optimization, so called "error map".

Previous studies ((27), (29), (30)) indicated that the set of unknown error parameters are not linearly independent and that they cannot be separated by best fitting. To solve this, arbitrary constraints must be introduced. In spite of being arbitrary, they do not alter the compensation, rather select one out the infinite equivalent solutions resulting from the observations. A typical example of such constraints is as follows: all 18 error functions are constrained vertically (e.g. null at the left extreme of their domain), the straightnesses are constrained in their slope (e.g. they are null at the right extreme too of their domain) and three constant values are added to the model to account for the axis squarenesses. Another typical example is as before, but with three straightnesses only out of six constrained in their slopes, with no need for additional squareness values. In all cases, 21 degrees of freedom are to be constrained: 18 constant values + 6 slopes – 3 squarenesses in the first example, 18 constant values + 3 slopes in the second.

1.4.2 The procedural model

Even if the rotary table is capable of angular measurement, the following model does not rely on this and the table is regarded merely as a precision handler rather than as a measuring instrument. Counting on the table measurements would require a very accurate piece of equipment due to the long optical arms involved, resulting in an expensive device, affordable in this research work but not suited for the industrial target.

The most basic property of rotations is that the geometrical relation to the rotation axis of anything attached to the rotating body remains the same regardless of the rotation angle.

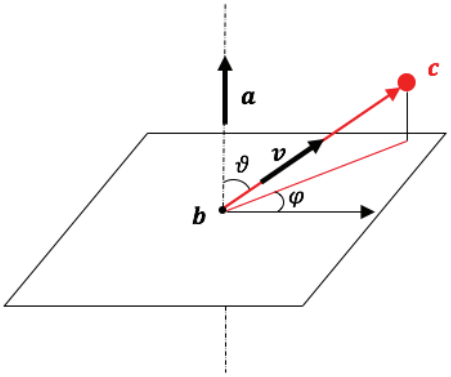

Figure 11. Scheme of the laser beam as rotated by the rotary table.

Let $\boldsymbol{a}$ and $\boldsymbol{v}$ be the unit vectors of the rotation axis and of the laser beam pointing to the target $\boldsymbol{c}$, respectively (Figure 11). Then the simple equation holds:

$$\boldsymbol{a}^{\mathrm{T}}\boldsymbol{v} = q, \quad q = \cos\vartheta, \tag{4}$$

regardless of the rotation angle φ. Only the inclination angle of the beam to the rotation axis, ϑ, counts. This angle is nominally right, i.e. $\vartheta \approx \frac{\pi}{2}$, $q \approx 0$. The table is attached to the ram and is then subject to its parasitic rotations. Let $\boldsymbol{r} = \boldsymbol{r}_x + \boldsymbol{r}_y + \boldsymbol{r}_z$ be such parasitic rotation, sum of those introduced by each carriage; then

$$\boldsymbol{a} = \boldsymbol{a}_0 + \boldsymbol{r} \times \boldsymbol{a}_0 = [\boldsymbol{I} + (\boldsymbol{r}\times)]\boldsymbol{a}_0, \tag{5}$$

where $\boldsymbol{a}_0$ is the table rotation axis in the absence of parasitic errors, i.e. when the machine is in a position where they are null, and the rotations are assumed to be small.

Let us assume at first that the laser line $\boldsymbol{v}$ intersects the rotary table axis $\boldsymbol{a}$, i.e. it is not skew to it; we will consider later the effect of skewness. Then

$$\boldsymbol{v} = \frac{\boldsymbol{c} - \boldsymbol{b}}{\|\boldsymbol{c} - \boldsymbol{b}\|}, \tag{6}$$

The point $\boldsymbol{b}$ can be considered as the localization point of the device and is conceptually similar to that of a stylus tip in a CMM or of the effective point in a machine tool. It is affected by the geometry error. Equation (6) becomes then

$$\boldsymbol{v} = \frac{\boldsymbol{c} - \boldsymbol{s} - \boldsymbol{p} - \boldsymbol{e}}{\|\boldsymbol{c} - \boldsymbol{s} - \boldsymbol{p} - \boldsymbol{e}\|} = \frac{1}{d}(\boldsymbol{c} - \boldsymbol{s} - \boldsymbol{p} - \boldsymbol{e}), \qquad d = \|\boldsymbol{c} - \boldsymbol{s} - \boldsymbol{p} - \boldsymbol{e}\| \tag{7}$$

where $\boldsymbol{s}$ is the position of the reference point on the ram as measured by the scale readout triplet, $\boldsymbol{p}$ is the probe offset, $\boldsymbol{e}$ is the geometry error of equation (1) and d is the distance of the target to the point $\boldsymbol{b}$.

By introducing equations (5) and (7), equation (4) becomes

$$\boldsymbol{a}_0^{\mathrm{T}}[\boldsymbol{I} - (\boldsymbol{r}\times)](\boldsymbol{c} - \boldsymbol{s} - \boldsymbol{p} - \boldsymbol{e}) \approx \boldsymbol{a}_0^{\mathrm{T}}[\boldsymbol{I} - (\boldsymbol{r}\times)](\boldsymbol{c} - \boldsymbol{s} - \boldsymbol{p}) - \boldsymbol{a}_0^{\mathrm{T}}\boldsymbol{e} = dq, \tag{8}$$

where the minus sign for the rotation $\boldsymbol{r}$ stems from the antisymmetry of the matrix $(\boldsymbol{r}\times)$ and the second order product $\boldsymbol{r} \times \boldsymbol{e}$ of the small rotation and the small geometry error is neglected.

Let us extend to the case that the laser line $\boldsymbol{v}$ is skew to the rotary table axis $\boldsymbol{a}$, due to an imperfect adjustment of the device. Let us decompose the probe offset in its components along and orthogonal to $\boldsymbol{a}$:

$$\boldsymbol{p} = p\boldsymbol{a} + \boldsymbol{p}_\perp, \; p = \boldsymbol{a}^{\mathrm{T}}\boldsymbol{p}, \; \boldsymbol{p}_\perp = (\boldsymbol{I} - \boldsymbol{a}\boldsymbol{a}^{\mathrm{T}})\boldsymbol{p}. \tag{9}$$

Let us observe that

$$\boldsymbol{a}_0^{\mathrm{T}}[\boldsymbol{I}-(\boldsymbol{r}\times)]\boldsymbol{a}=\boldsymbol{a}_{\boldsymbol{0}}^{\mathrm{T}}[\boldsymbol{I}-(\boldsymbol{r}\times)][\boldsymbol{I}+(\boldsymbol{r}\times)]\boldsymbol{a}_0= \\ =\boldsymbol{a}_{\boldsymbol{0}}^{\mathrm{T}}[\boldsymbol{I}-(\boldsymbol{r}\times\boldsymbol{r}\times)]\boldsymbol{a}_0\approx 1, \tag{10}$$

where we neglected the second order term $(\boldsymbol{r}\times\boldsymbol{r}\times\boldsymbol{a}_0)$ ($\boldsymbol{r}$ is a vector of small angles). By introducing equations (9) and (10) in equation (8), and by remembering that $\boldsymbol{a}_0^{\mathrm{T}}\boldsymbol{p}_\perp=0$ by definition, the procedural model becomes

$$\boldsymbol{a}_0^{\mathrm{T}}[\boldsymbol{I}-(\boldsymbol{r}\times)](\boldsymbol{c}-\boldsymbol{s}-\boldsymbol{p}_\perp)-p-\boldsymbol{a}_0^{\mathrm{T}}\boldsymbol{e}= \\ =\boldsymbol{a}_{\boldsymbol{0}}^{\mathrm{T}}\{[\boldsymbol{I}-(\boldsymbol{r}\times)](\boldsymbol{c}-\boldsymbol{s})+\boldsymbol{r}\times\boldsymbol{p}_\perp\}-p-\boldsymbol{a}_0^{\mathrm{T}}\boldsymbol{e}=dq. \tag{11}$$

Any small error $\delta\boldsymbol{p}_\perp$ of the estimate of $\boldsymbol{p}_\perp$ gets multiplied by the small rotation vector $\boldsymbol{r}$ and results in a negligible second order term. Consequently, any accidental misalignment of the laser beam causing skewness to the rotation axis would be sensed negligibly by the model equation. This is understood physically by considering the kinematic redundancy introduced by the rotary table, which is in fact a fourth axis: a small movement of the ram orthogonal to the rotation axis can be recovered by a small table rotation. A further consequence is that the value of $\boldsymbol{p}_\perp$ does not need to be refined by fitting to the data – i.e. to be an unknown in the fitting – and an a priori estimation suffices.

The model delivers an equation for each measurement. We can index each measurement by three attributes:

- Which of the M table orientations: let us indicate this with the index i, $1\le i\le M$.
- Which of the N targets: let us indicate this with the index j, $1\le j\le N$.
- The ordinal index, given an i and a j. A same target can be pointed at from different angles and machine positions. Let us indicate this with the index k_{ij}, $1\le k_{ij}\le O_{ij}$ where O_{ij} is the number of measurements done with the i-th table orientation and the j-th target. To avoid a second level index, k_{ij} will be abbreviated to k whenever unambiguous for sake of simplicity.

Based on the above, let us attribute proper subscripts to each variable in equation (11):

- $\boldsymbol{a_0}$ depends only on (effectively is) the orientation of the table; as in the equation there is no more need to distinguish between when it is unaffected ($\boldsymbol{a_0}$) or affected ($\boldsymbol{a}$) by the geometry errors, let us use the symbol $\boldsymbol{a_i}$, with no subscript 0 for sake of simplicity.
- $\boldsymbol{r}$ and $\boldsymbol{e}$ depend on the position of the carriages (and on the probe offset): $\boldsymbol{r}_{ijk}$ and $\boldsymbol{e}_{ijk}$.
- $\boldsymbol{c}$ depends only on (effectively is) the position of the targets: $\boldsymbol{c}_j$.
- $\boldsymbol{s}$ depends only on (effectively is) the position of the carriages: $\boldsymbol{s}_{ijk}$.
- $\boldsymbol{p}_\perp$ and p define the table position imposed by wrist articulation: $\boldsymbol{p}_{\perp i}$ and p_i.

- d is the distance to the target and depends on the position of the carriages: d_{ijk}.
- q is a global scalar which is a characteristic of the coupling of the pointer to the table: no subscripts.

As a result, equation (11) becomes

$$\boldsymbol{a}_i^{\mathrm{T}}\{[\boldsymbol{I} - (\boldsymbol{r}_{ijk}\times)](\boldsymbol{c}_j - \boldsymbol{s}_{ijk}) + \boldsymbol{r}_{ijk}\times\boldsymbol{p}_{\perp i}\} - p_i - \boldsymbol{a}_i^{\mathrm{T}}\boldsymbol{e}_{ijk} = d_{ijk}q \quad (12)$$

Equation (12) is the sought procedural model.

1.5 The error model for the straightness approach

The rigid body model is equally valid for this approach as it was for the previous one (see § 1.1.1). What changes and is of interest in this section is the procedural model.

Let $\boldsymbol{v}$ be the unit vector of the direction of sight of the instrument and $\boldsymbol{n}$ the orthogonal unit vector in the direction of sensitivity, $\boldsymbol{n}^{\mathrm{T}}\boldsymbol{v} = 0$. Let $\boldsymbol{b}$ be a point on the line $\boldsymbol{v}$ where the device indicates zero and $\boldsymbol{\ell}$ the device reading. The following equation holds:

$$\ell = \boldsymbol{n}^{\mathrm{T}}(\boldsymbol{c} - \boldsymbol{b}), \quad (13)$$

where $\boldsymbol{c}$ is the position of the target, given by the combination of the scale readings $\boldsymbol{s}$, the probe offset $\boldsymbol{p}$ and the geometry error $\boldsymbol{e}$:

$$\boldsymbol{n}^{\mathrm{T}}(\boldsymbol{s} + \boldsymbol{p} - \boldsymbol{b} + \boldsymbol{e}) = \ell, \quad (14)$$

We made the point earlier that the device is mostly a zero detector, and that the machine is driven finely to search a nearly null reading of the device. As a consequence, we expect ℓ to be small at any measurement point. Also, the device reading ℓ and the position of the machine along the sensitivity direction $\boldsymbol{n}^{\mathrm{T}}\boldsymbol{s}$ are coupled: a small movement of the machine along $\boldsymbol{n}$ causes an equivalent increment of the reading ℓ.

Let us investigate the sensitivity unit vector $\boldsymbol{n}$ and particularly whether its two degrees of freedom (orientation angles) are equally important to the model.

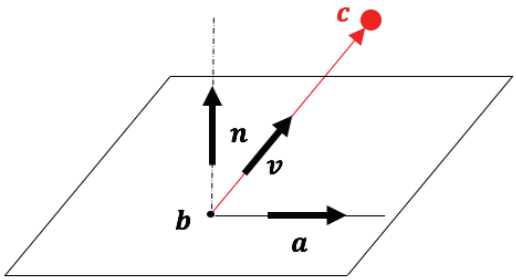

Figure 12. The direction of sight $\boldsymbol{v}$, the direction of sensitivity $\boldsymbol{n}$ and the auxiliary unit vector $\mathbf{a} = \boldsymbol{v} \times \boldsymbol{n}$ form a right-handed orthogonal triple.

Let us apply a small rotation to $\boldsymbol{n}$ about either $\boldsymbol{v}$ or $\boldsymbol{a}$ (Figure 12):

$$\begin{aligned} \boldsymbol{n}'_{\boldsymbol{v}} &\approx \boldsymbol{n} + \alpha \boldsymbol{a}, \\ \boldsymbol{n}'_{\boldsymbol{a}} &\approx \boldsymbol{n} - \beta \boldsymbol{v} \end{aligned} \tag{15}$$

where α and β are two small rotation angles. Substitution of equations (15) in equation (14) yields

$$\begin{aligned} (\boldsymbol{n} + \alpha \boldsymbol{a})^{\mathrm{T}} (\boldsymbol{s} + \boldsymbol{p} - \boldsymbol{b} + \boldsymbol{e}) &= \ell, \\ (\boldsymbol{n} - \beta \boldsymbol{v})^{\mathrm{T}} (\boldsymbol{s} + \boldsymbol{p} - \boldsymbol{b} + \boldsymbol{e}) &= \ell \end{aligned} \tag{16}$$

The first equation (16) indicates that an error α in the planar orientation about $\boldsymbol{n}$ introduces sensitivity to the straightness in the orthogonal direction $\boldsymbol{a}$. This contribution is second order, being the product of such straightness and the small angle α.

In the second equation (16), $(\boldsymbol{s} + \boldsymbol{p} - \boldsymbol{b} + \boldsymbol{e})$ is mostly directed along the line of sight $\boldsymbol{v}$ and the product $\boldsymbol{v}^{\mathrm{T}}(\boldsymbol{s} + \boldsymbol{p} - \boldsymbol{b} + \boldsymbol{e})$ results in a linear coordinate along the line of sight $\boldsymbol{v}$. We may take the origin of this coordinate in the centroid of all points measured along the line:

$$\beta \boldsymbol{v}^{\mathrm{T}} (\boldsymbol{s} + \boldsymbol{p} - \boldsymbol{b} + \boldsymbol{e}) \approx \beta \xi, \text{ where } \xi = \boldsymbol{v}^{\mathrm{T}} (\boldsymbol{s} - \bar{\boldsymbol{s}}), \text{ with } \bar{\boldsymbol{s}} = \frac{1}{N} \sum_{i=1}^{N} \boldsymbol{s}_i. \tag{17}$$

In other words, a linear term with slope β gets added due to the misalignment, as expected.

The conclusion is that the two degrees of freedom of $\boldsymbol{n}$ are not equally important: the spatial orientation (about $\boldsymbol{a}$) is important and is then to be included as an unknown in the optimization, whereas an a priori estimation of the planar orientation (about $\boldsymbol{v}$) is sufficient with no need to be refined in the optimization. We can capture this by transforming equation (14) to

$$\boldsymbol{n}_0^{\mathrm{T}} (\boldsymbol{s} + \boldsymbol{p} - \boldsymbol{b} + \boldsymbol{e}) + \beta \xi = \ell, \tag{18}$$

where $\boldsymbol{n}_0$ is an approximation of the sensitivity direction no more subject to optimization.

Let us consider now the probe offset $\boldsymbol{p}$ and the localisation point of the device $\boldsymbol{b}$. They never occur separately, always do as $\boldsymbol{p} - \boldsymbol{b}$. This means that in fact they are a single model parameter. Also, only its component along $\boldsymbol{n}$ is of interest. As a consequence, it is a scalar unknown for each measurement line. This effectively captures the location of the reference line (e.g., the intercept) in the straightness measurement. Let us call this $h = \boldsymbol{n}_0^{\mathrm{T}}(\boldsymbol{p} - \boldsymbol{b})$. Equation (18) transforms to

$$\boldsymbol{n}_0^{\mathrm{T}}(\boldsymbol{s} + \boldsymbol{e}) + \beta\xi + h = \ell. \tag{19}$$

Let us rearrange it as

$$\boldsymbol{n}_0^{\mathrm{T}}\boldsymbol{s} - \ell + \beta\xi + h + \boldsymbol{n}_0^{\mathrm{T}}\boldsymbol{e} = 0, \tag{20}$$

to highlight the correlation of $\boldsymbol{n}_0^{\mathrm{T}}\boldsymbol{s}$ and ℓ, as illustrated earlier on.
The model delivers an equation for each measurement. We can index each measurement by two attributes:

- Which of the M lines: let us indicate this with the index j, $1 \le j \le M$.
- The ordinal index, given a j. Let us indicate this with the index i_j, $1 \le i_j \le N_j$ where N_j is the number of measurements along the j-th line. To avoid a second level index, i_j is abbreviated to i whenever unambiguous for sake of simplicity.

Based on the above, let us attribute proper subscripts to each variable in equation (20).

- $\boldsymbol{n}_0$ depends only on (effectively is) the orientation of the device (and then of the measurement line): $\boldsymbol{n}_{0j}$.
- $\boldsymbol{s}$, $\boldsymbol{e}$ and ℓ depend on the position of the carriages (and on the probe offset): $\boldsymbol{s}_{ij}$, $\boldsymbol{e}_{ij}$ and ℓ_{ij}.
- β and h depend on (effectively are) the measurement reference line: β_j and h_j.
- ξ is the abscissa of individual points along a measurement line: ξ_{ij}.

As a result, equation (20) becomes

$$\boldsymbol{n}_{0j}^{\mathrm{T}}\boldsymbol{s}_{ij} - \ell_{ij} + \beta_j\xi_{ij} + h_j + \boldsymbol{n}_{0j}^{\mathrm{T}}\boldsymbol{e}_{ij} = 0, \tag{21}$$

Apart from the unknowns directly related to the rigid body model introduced by the term $\boldsymbol{e}_{ij}$ (that is, the sought optimization outcome), $2M$ additional unknowns are introduced, namely β_j and h_j, $1 \le j \le M$. They are clustered according to the measurement line j: if and only if points are on the same measurement line share the same (β_j, h_j) values. This leads to separation of the variables in the optimization, resulting in

$$\boldsymbol{n}_{0j}^{\mathrm{T}}\boldsymbol{e}_{ij} = \hat{\ell}_{ij}, \quad \text{where} \quad \hat{\ell}_{ij} = -\boldsymbol{n}_j^{\mathrm{T}}\boldsymbol{s}_{ij} + \ell_{ij} - \beta_j\xi_{ij} - h_j. \tag{22}$$

$\widehat{\ell}_{ij}$ are the joint readings of the machine and of the device after subtraction of a least squares line.

Equation (22) is the sought procedural model. The optimization is exclusively about unknowns of interest, that is, the machine geometry error $\boldsymbol{e}$.

Even a first glance comparison of equations (22) and (12) shows the great simplification this approach has enabled in the procedural model.

Chapter 2

Implementation of the concept

The old InPlanT concept investigated in LUMINAR project suffered from two major drawbacks:

- the distance of the target sphere influenced the shape and size of the backscattered pattern dramatically;
- the accurate processing of the image was time consuming and heavily affected by acquisition noise.

A new paradigm was then implemented to overcome the cited limitations. As the measured lateral displacement is 1D only, the camera was replaced by a fast photodiode integrating the total intensity through a focusing lens. To improve the resolution, a mechanical modulation was introduced by a controlled and cyclic movement of a slit chopping the laser beam.
It was proven that the signal coming from the sphere were mainly influenced by two parameters: the distance between laser source and the target itself, and the slit width. To estimate their contribution, some optical simulations were carried out using a proper software (Figure 13), replicating a suitable optomechanical set up: a collimated gaussian source (which constitutes the pointing direction of the instrument) impinging onto a S-LAH79 glass sphere, backscattering ~15 % of the signal, with a beam splitter directing the return signal towards a detector; to estimate the signal behaviour, several distances of the sphere were investigated in the range (0 ÷ 5) m, with a variable-aperture (0.5 ÷ 8) mm slit placed in the return branch of the signal at different transversal positions (-1 ÷ 1 mm). Figure 14 shows the results, with (a) and (b) exhibiting the total luminous intensity received by the detector: in (a) the dependence of attenuation on the distance between sphere and target is linear, with a rate of 1 dB/m; in (b) the response at different slit widths shows a saturation (-17 dB represent the amount of attenuation of backward signal in the absence of the slit, namely with any portion of the signal masked).
Figure 15 shows the dependence of the backscattered signal on the lateral movement of the target, in correspondence with three different working distances of the sphere and three slit widths (with the lateral distance normalized to the radius R of the sphere); this new simulation proved that slit widths in the range (1 – 2) mm could be considered as eligible for the purpose.

In the performed simulations, the intensity profile of the retroreflected beam exhibits a central symmetry with a distinct peak in the center. This peak propagates along the line from the target center parallel to the instrument pointing direction and conveys the information of the target lateral position.
The backscatter image and total power were investigated to predict whether enough resolution was achievable in different optomechanical layouts; the results were encouraging and validated the concept.

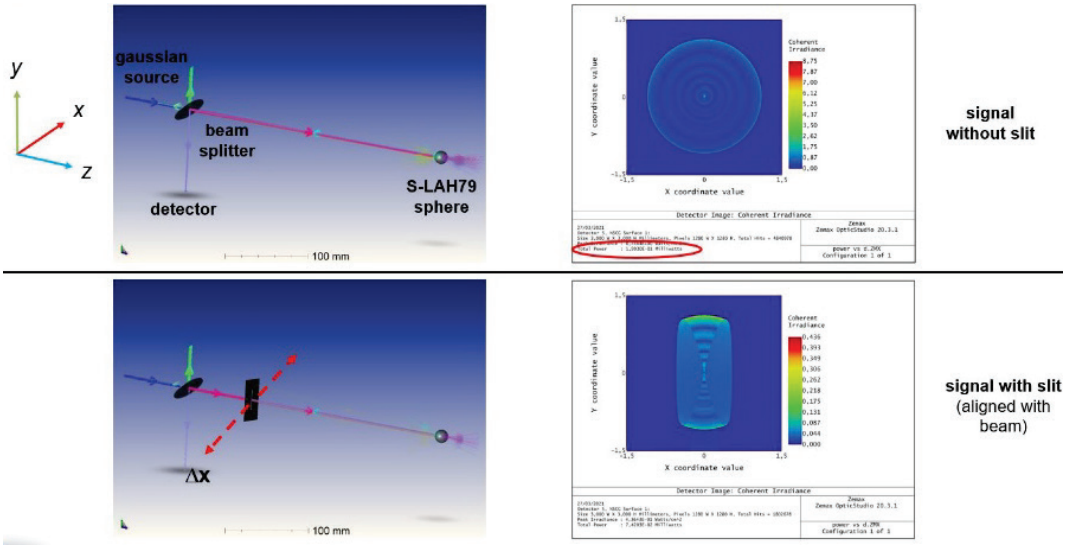

Figure 13. Example of simulation with Zemax Optic Studio software.

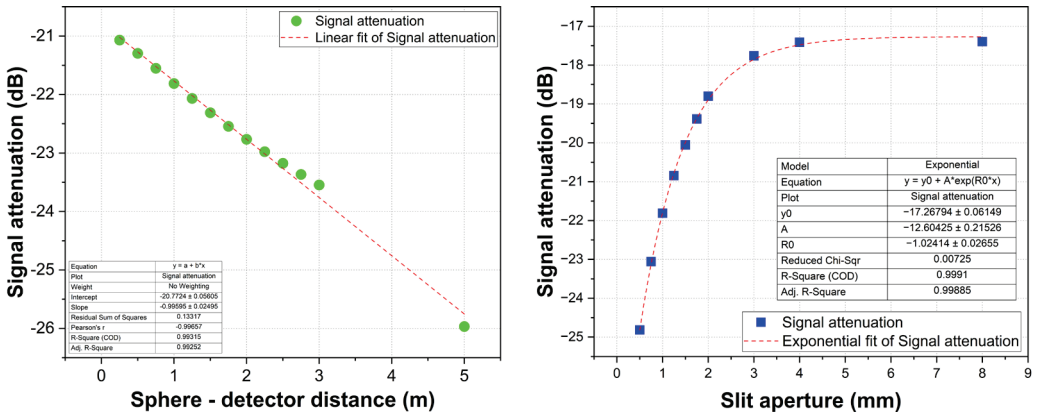

(a) (b)

Figure 14. (a): simulated attenuations of the signal backscattered from the sphere as a function of the distance of the detector in case of null lateral displacement of the slit (31); input power = 10 mW, slit aperture = 1 mm, detector size = (3 × 3) mm^2, ϕ_{sphere} = 16 mm, slit in axis with beam; (b): attenuation as a function of the slit width at a fixed distance of 1 m, same layout as (a).

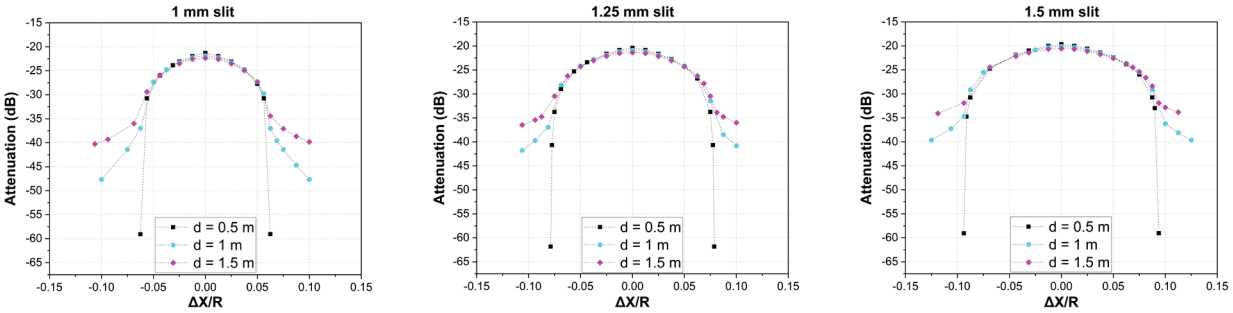

Figure 15. Simulated attenuation as a function of the sphere lateral displacement, with three slit widths (1 mm, 1.25 mm and 1.5 mm) at three different distances of the target (0.5 m, 1 m and 1.5 m). The apparent asymmetry is due to unequal spacing of the sampled points.

Figure 16 shows the very first set up implemented on a breadboard to study the raw signals backscattered by the sphere, with a CMOS camera used as a sensor to digitally acquire and process the patterns; Figure 17 shows the peculiarity of the patterns to deal with (also in the continuation of the work) (see (32) for an extensive description of the peculiar backscattered patterns from high-index ball lenses), with and without the slit masking a portion of the signal.

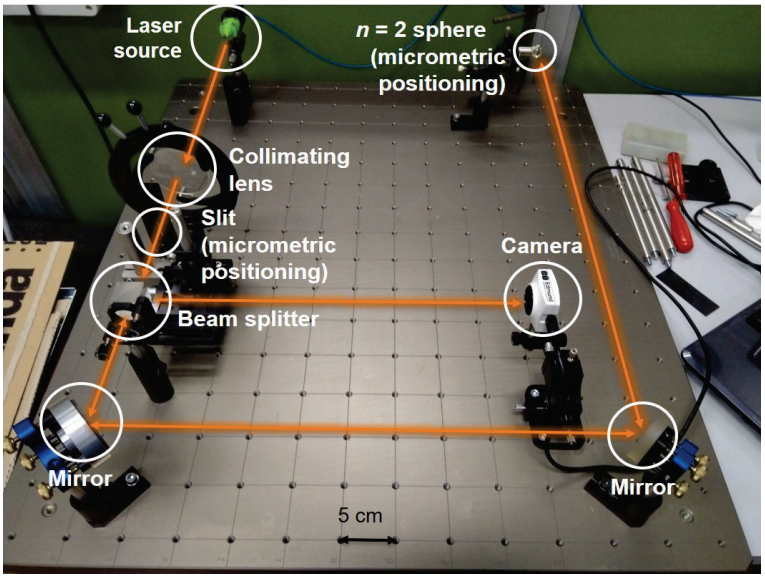

Figure 16. "Static" experimental set up used to test the concept.

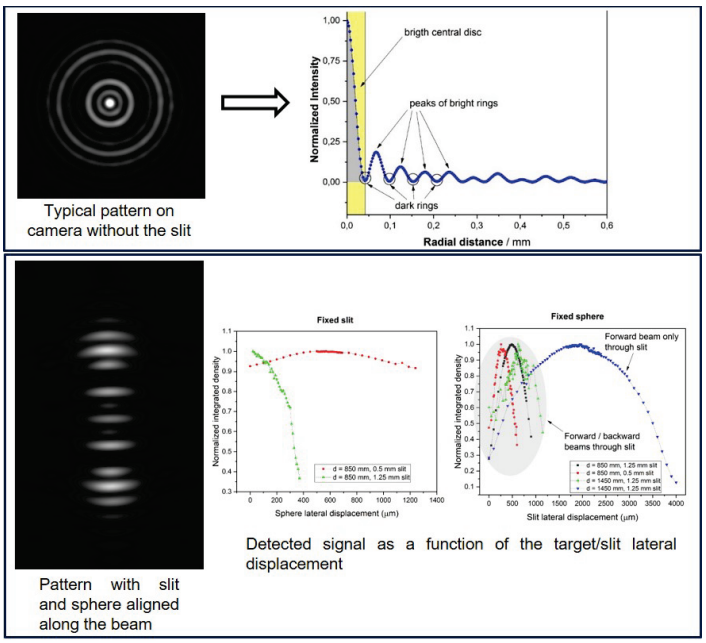

Figure 17. Typical signals backscattered from the sphere, placed at approximately 90 cm away from the camera, without (figure above) and with (figure below) a slit initially positioned in axis with the onward signal and then moved aside.

With the aim of improving the resolution and reducing the effects of noise, a mechanical modulation was introduced, moving from a static signal processing in the space domain to a dynamic processing in the time domain. Since the modulation has a periodic nature, the analysis of data was turned into a phase measurement, thus allowing the rejection of some factors affecting the uncertainty of the data themselves; moreover, averaging over an arbitrary number of modulation cycles permitted to compress the noise, as it will be explained in detail in §2.3.1.

Two different strategies were investigated to implement the slit movement and consequently the modulation of the signal: a rotating disc and an oscillating stage (33). These mechanisms were totally different in design, each of them requiring peculiar components and different approaches; they also generated different signal in different positions of the target (one peak per cycle in the case of the rotating disc and two peaks per cycle for the oscillating stage, as shown in Figure 18), so efforts were made to face the complications of managing such a variability of situations (in turn related to many different patterns of the signals based on the location of the sphere). Anyway, both for the rotating disc and the oscillating stage, the strategy for the achievement of the sought information about the lateral position of the sphere relied on the analyses of the peak phase: within the cycle in the former situation, in reference to each other in the latter.

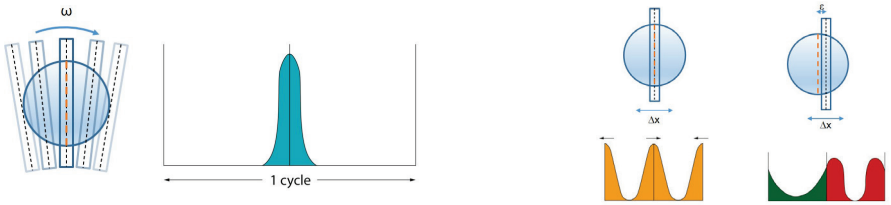

(a) (b)

Figure 18. Patterns of the photodiode signals as a function of time: with rotating disc (a) and periodically oscillating stage

2.1 Built prototypes

2.1.1 First prototype ("P1"): description and characterization

P1 was implemented on the basis of a light source consisting in a collimated laser diode, with the necessary optics to focus the retroreflected signal on a photodiode (a commercial Newport model[4]), a 200 mm diameter plastic disc driven by a DC motor, and an Optek optical switch[5] placed at the edge of the disc and in charge of generating the reference signal. A Picoscope 4424[6] was chosen as the oscilloscope to acquire the signals. Various slits of different widths were made on the surface of the disc to investigate their effect on the pattern of the backscattered signals, but only one at a time was used during the measurements (Figure 19), occasionally covering the others. Figure 20 shows the pattern of the signals acquired by Picoscope, and Figure 21 shows preliminary the set up used for testing the concept. Four different chopping schemes were tested, labelled A, B1, B2 and C depending on the chosen position of the slit in the layout: A and C chopped both the onward and backward beam, while B1 and B2 chopped the backward beam only (Figure 22).

[4] Model 2051-FS-M
[5] Datasheet link for optical switch
[6] Datasheet link for oscilloscope

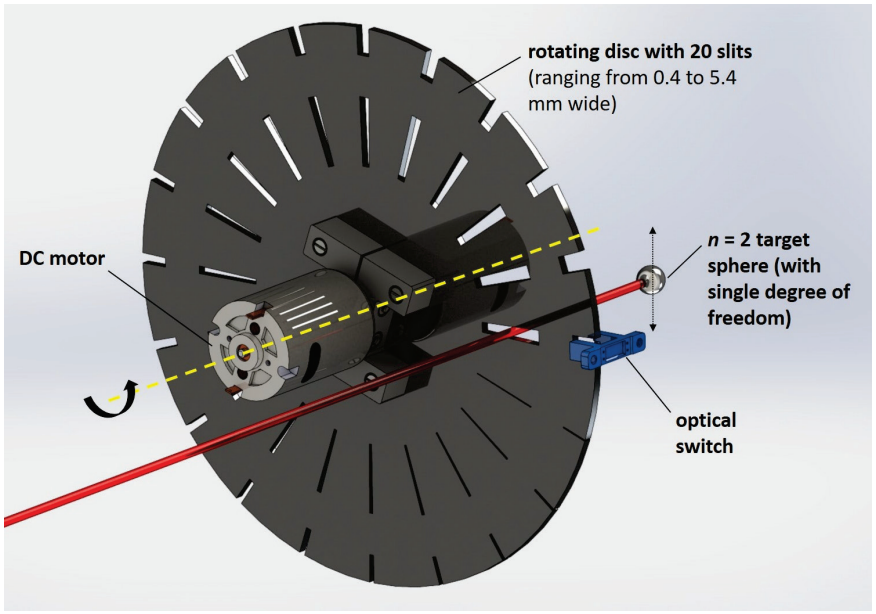

Figure 19. Rotating disc for the modulation of the signals.

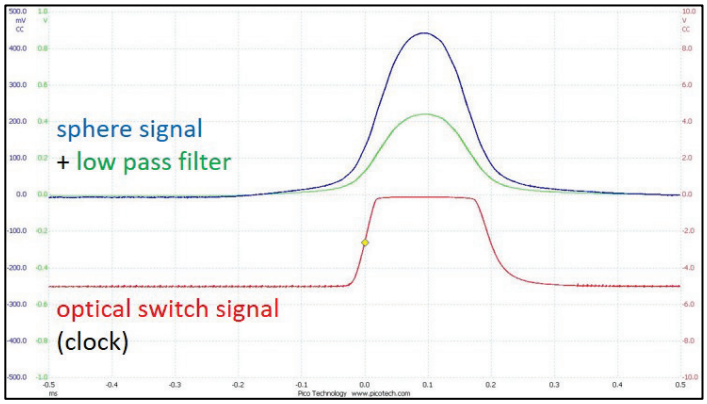

Figure 20. Signals acquired by Picoscope (no phase displacement between sphere and optical switch signal – "perfect" alignment).

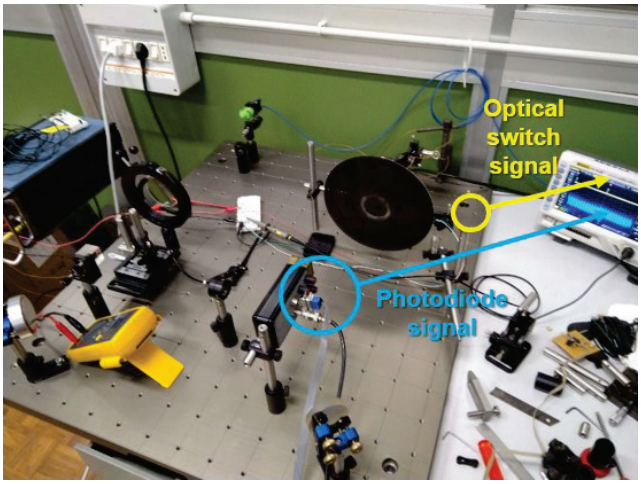

Figure 21. Set up for testing the modulation of photodiode signal by rotating disc.

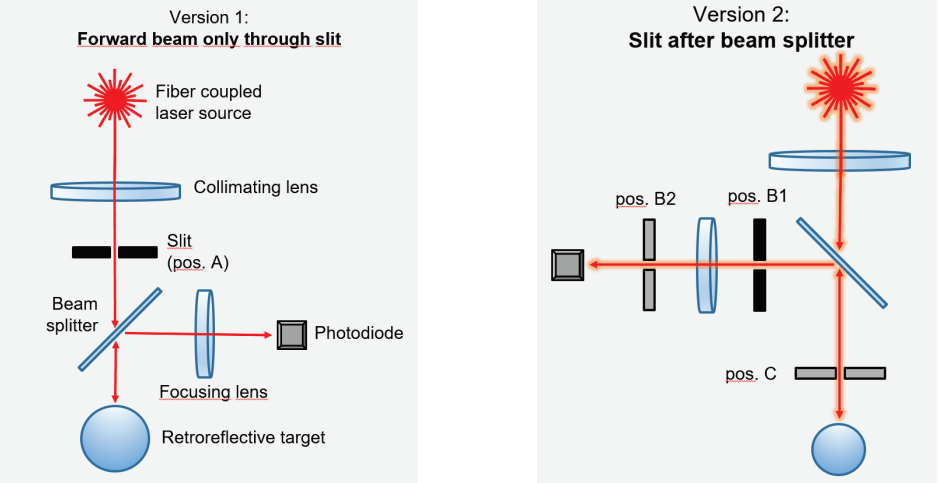

(a) (b)

Figure 22. Tested layouts and corresponding chopping schemes.

The optical switch detected the rotation of the disc, without taking into account the position of the target; the phase measurement was referred to the time base provided by the optical switch, with the photodiode signal conveying the information about the lateral displacement of the sphere. The relative phase was obtained by cross-correlating the detected peak with a reference peak that was in phase with the clock signal (Figure 23): that was possible by implementing a software written in Python. The next step was to estimate the resolution of the system; the implemented procedure can be described in this way: the target was moved laterally (with respect to the impinging beam) in controlled steps of 200 µm using a micrometric stage, and the signals were acquired (Figure 24 (a)). Their cross-correlations with a reference signal were calculated (Figure 24 (b)), so that the response characteristic could be best fitted, allowing the determination of the sensitivity k (Figure 24 (c)). For the evaluation of the noise, ten signals were acquired with the sphere always in the same position; the standard deviation σ_t^{noise} of the cross-correlations maxima was calculated (Figure 24 (d)), so that the resolution could finally be evaluated as $\sigma_t^{\text{noise}}/k$ (Table 2).

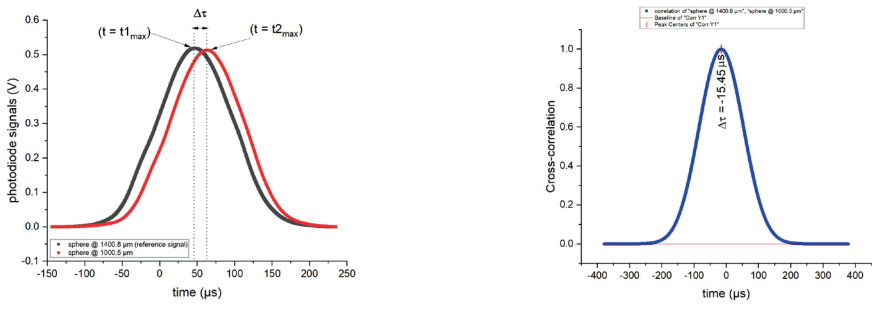

(a) (b)

Figure 23. Example of cross-correlation strategy implemented on real sphere signals; (a): sphere in a reference position (black curve) and sphere moved aside (red curve). (b): cross correlation of the same signals; the peak position identifies the time displacement $\Delta\tau$ between the acquired signals.

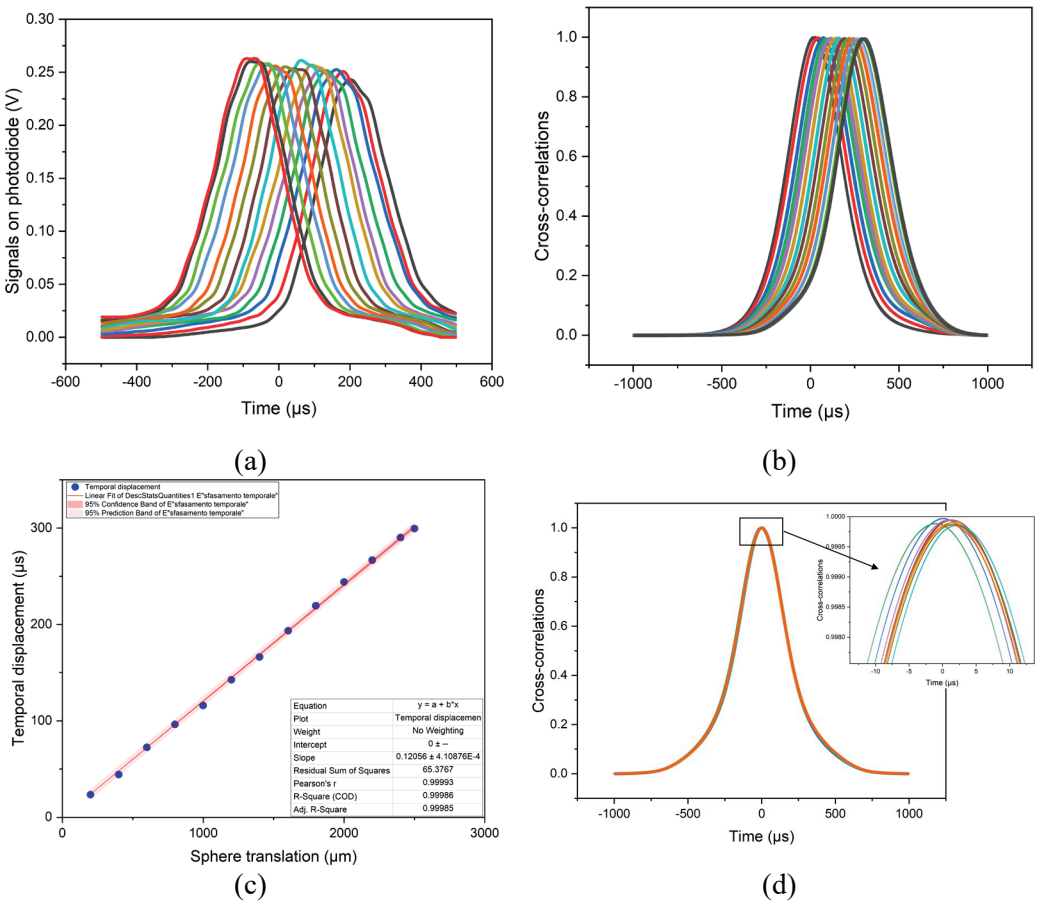

Figure 24. Strategy for the evaluation of the resolution.

Layout	Sensitivity k / (μs/μm)	Noise σ_τ^{noise}/μs	Resolution / μm	Target distance d / cm
A	0.04	0.65	15.77	135
B1	0.12	0.92	7.60	145
B2	0.03	0.86	27.55	135
C	0.13	1.05	7.87	135
B1 bis[7]	0.09	0.79	8.46	297

Table 2. Resolution of P1 prototype.

2.1.2 Second prototype ("P2"): description and characterization

P1 suffered from two major limitations: the overall size and the resolution that could be achieved. To minimize the effects connected to the rotation (especially the vibrations), a large diameter (∅ 200 mm) disc was necessary; in addition, the

[7] Same chopping scheme as B1, but with higher target distance.

device was substantially blind over most of the time during its rotation, detecting a signal only when the slit intercepted the beam, and this occurred in a tiny time fraction: that required a fast signal detection or a low rotation speed, forcing us to a compromise between resolution and throughput. For these reasons, the ideal modulation mechanism for our application turned out to be a pure translating instead of rotating slit. This awareness triggered the need of a completely new design, where the modulation could be achieved by means of a slit moving with oscillating motion.

In order to realize a reciprocating motion, three strategies were investigated (34): cam and follower mechanism, Scotch Yoke (or slotted link) and the slider-crank linkage. Custom solutions that could be adapted to our specific needs were designed (Figure 25), but the slider-crank proved to be the most practical to be realized.

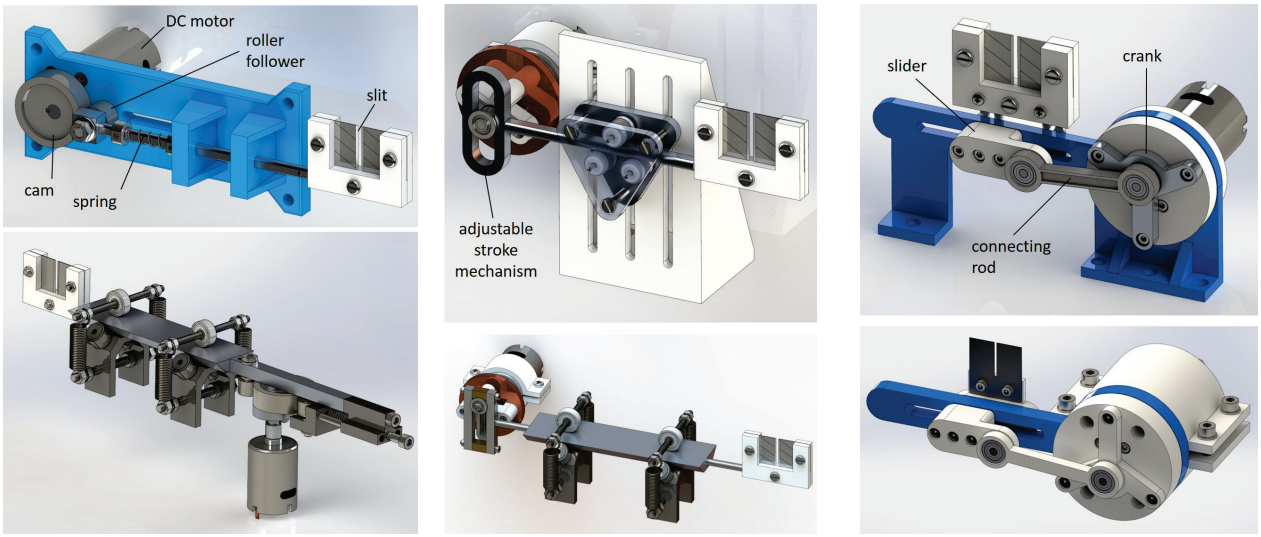

Figure 25. Various strategies for the implementation of the reciprocating motion of the slit: with cam and roller follower (a), Scotch-Yoke (b) and slider-crank (c).

A preliminary ABS 3D-printed prototype, consisting in a connecting rod, bearings and a slotted guide, propelled by a DC motor, was followed by an upgraded one based on the same concept, with a lubricated steel guide and an accurate hard disc motor used to drive the slit (Figure 26).

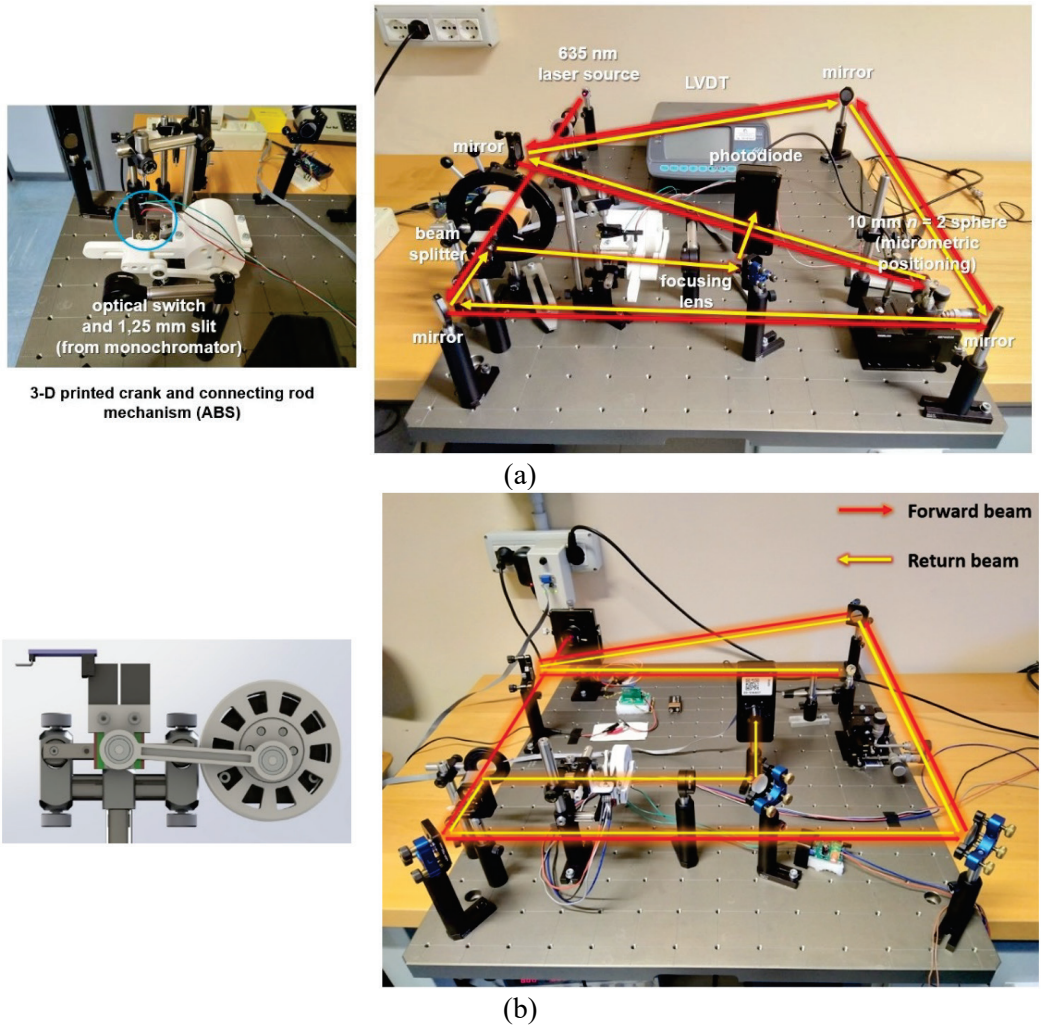

Figure 26. Prototype P2. First 3D printed version, with its test bed (a); second implementation of the same concept, with upgraded parts and its test bed (b).

P2 yelded two peaks per cycle, unlike P1 (yelding just one), while the slit crossed the center of symmetry of the back-reflected beam in both directions of motion. The derivation of the lateral displacement of the target is conceptually possible with some modelling.

Let t_1 and t_2 the times corresponding to the occurrence of the first and second peak, T the period, t_0 the initial time and φ_1 and φ_2 the phases of the peaks. The following relations hold:

$$\varphi_1 = 2\pi\frac{t_1 - t_0}{T};\ \varphi_2 = 2\pi\frac{t_2 - t_0}{T}, \tag{23}$$

$$\Delta\varphi = \varphi_2 - \varphi_1 = 2\pi\frac{t_2 - t_1}{T}, \tag{24}$$

Focusing on the central point of oscillation, a variable y can be introduced to express the lateral position of the beam with respect to that point; the two peaks are displayed on the data acquisition hardware when the slit occurs at the same position (that of the backscattered beam center of symmetry). The corresponding equation are:

$$\begin{cases} y = f(\varphi_1) \\ y = f(\varphi_2) \\ \Delta\varphi = \varphi_2 - \varphi_1 \end{cases} \tag{25}$$

where f is the law expressing the motion of the slit a function of the phase. If we divide the cycle into a couple of intervals where f is monotonic, φ_1 and φ_2 occur respectively in the first and in the second interval. Introducing the piecewise inverse functions g and h to solve Equation (25), it holds:

$$\begin{cases} \varphi_1 = g(y) \\ \varphi_2 = h(y) \\ \Delta\varphi = \varphi_2 - \varphi_1 \end{cases} \Rightarrow\ h(y) - g(y) = \Delta\varphi \tag{26}$$

From Equation (26) the target position y as a function of the phase difference $\Delta\varphi$ of the two peaks can be derived. Considering now the *sensitivity* s, the following equation can be written:

$$s = \frac{\partial\Delta\varphi}{\partial y} = \frac{dh(y)}{dy} - \frac{dg(y)}{dy} = \frac{1}{\frac{df(\varphi_2)}{d\varphi_2}} - \frac{1}{\frac{df(\varphi_1)}{d\varphi_1}} \tag{27}$$

If the slit speeds v_1 and v_2 at the peaks are introduced, and keeping in mind the definition of phase, we get:

$$s = \frac{1}{v_2\frac{dt_2}{d\varphi_2}} - \frac{1}{v_1\frac{dt_1}{d\varphi_1}} = \frac{1}{v_2\frac{T}{2\pi}} - \frac{1}{v_1\frac{T}{2\pi}} = \frac{2\pi}{T}\left(\frac{1}{v_2} - \frac{1}{v_1}\right) = -\frac{4\pi}{v_H T}$$
$$\frac{1}{v_H} = \frac{1}{2}\left(\frac{1}{v_1} - \frac{1}{v_2}\right) \tag{28}$$

with v_{H} identifying the harmonic mean of the speeds in correspondence of the peaks. It is important to emphasize that between s and the slit speed when crossing the beam there is an inverse proportionality; in a purely sinusoidal motion with a centered target, $v_1 = -v_2 = A\omega$ (with A = oscillation amplitude and ω = angular speed), and this expresses an avoidable trade-off between sensitivity and measuring interval: having defined an oscillation frequency, a large amplitude allows a large measuring interval, but at the cost of the sensitivity. Moreover, the law of motion of a crank and connecting rod is not purely harmonic (35) (Figure 27); since the law of motion is expressed with a transcendental equation, the device response cannot be derived from Equation (26): this awareness forces us to calibrate the device, instead of proceeding analytically.

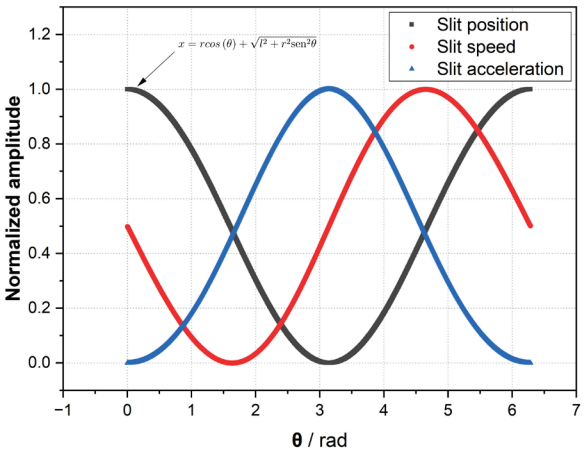

Figure 27. Plot showing the dependance of normalized slit position, speed and acceleration on crank angle θ, with l = 80 mm connecting rod and r = 5 mm crank radius.

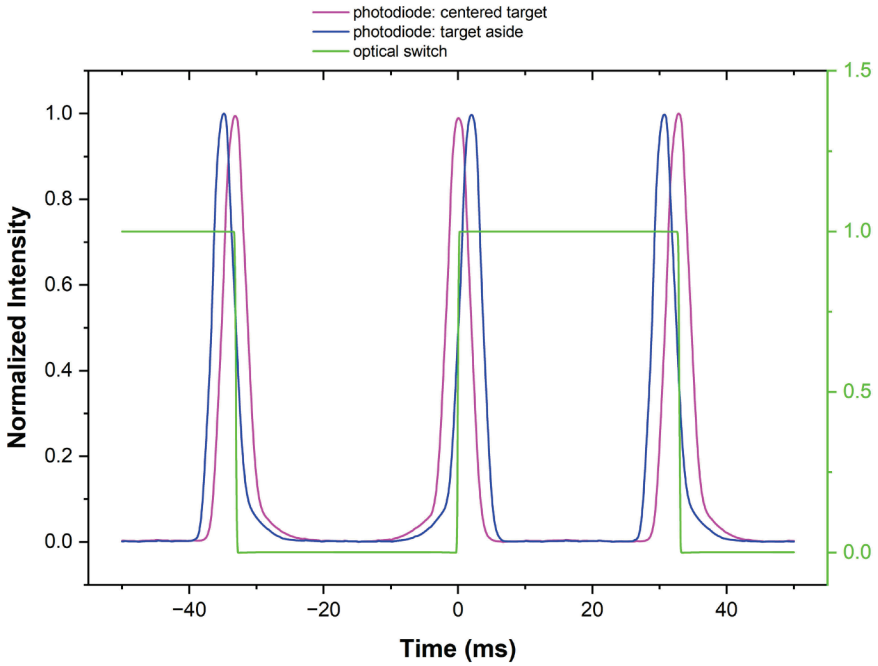

Figure 28. Normalized signals (photodiode: magenta – centered target and blue – 1 mm aside, digital switch: green) acquired by Prototype P2; each curve is the mean of 100 samples @ 1 MHz.

Figure 28 shows the normalized signals acquired by P2 prototype, with the time base given by an optical switch setting the phase scale and the photodiode signal captured in two positions of the sphere: at "central" position, and aside. Defining as "odd" the peaks on the descending fronts of the clock signal (slit moving left) and "even" those on the raising fronts (slit moving right), when moving the target aside the odd and the even peaks translated in opposite directions; the sought phase information could hence be inferred by quantifying this displacement observed in changing positions of the peaks in time. The elected mathematical tool for the phase derivation was the mutual cross-correlation, as it was done for P1. The distinction between odd and even peaks, possible thanks to the observation of the digital signal

(triggering the acquisition of the photodiode signal), allowed to set the sign of the instrument indication. Near the extremes of the measuring interval of the target some caution was required, since the peaks were prone to lose separation and to coalesce gradually, especially with the sphere placed at high distances (> 3 m). To face this problem, software thresholding and filtering were adopted as a countermeasure.

The achievable resolution was investigated following the same procedure used for P1 (Figure 29), and the best result was 1.67 µm at a sphere distance of 218 cm (Table 3), satisfactorily smaller than P1.

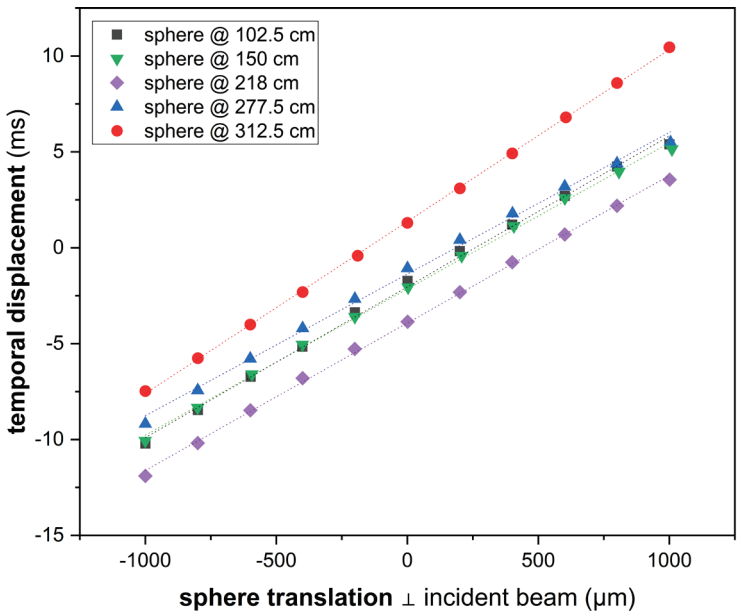

Figure 29. P2 Calibration curves at different distances of the target; sphere lateral position measured by TESA TESATRONIC TT60 LVDT.

Target distance *d* / mm	**Sensitivity *k*** / (µs/µm)	**Intercept** / ms	R^2	**Noise** σ_τ^{noise} / µs	**Resolution** / µm
1025	111.45	1.37	0.9980	0.024	2.67
1500	131.23	−2.15	0.9985	0.021	2.78
2180	129.99	−3.92	0.9991	0.013	1.67
2775	135.40	−1.37	0.9967	0.013	1.69
312.5	127.11	−2.03	0.9998	0.033	4.26

Table 3. P2 calibration results.

2.1.3 Third prototype ("P3"): description and characterization

The third evolution of the device was designed as a compact and portable version of the previous ones, possibly suitable to be installed onboard of machine tools. The

need to scale down all the maximum numbers components was fulfilled in part, since P3 remained a prototype still built for investigation. A mix of sturdy aluminum components, commercial (Thorlabs) steel stands and clamps, and 3D printed plastic parts was at the base of its design. Accurate alignment and fine adjustment of the key components (especially the slit and the photodiode, the metrological heart of the whole system), after an initial installation on the breadboard, were mandatory; to fulfil this requirement, all the degrees of freedom were identified and satisfied, also by means of the introduction of fine positioning facilities that helped for the purpose, adding redundancy beyond the expected needs. To achieve a nearly perfect 50 % duty cycle of the digital signal, a high precision translation stage was used for a fine adjustment of the optical switch with respect to the slit (Figure 30, Figure 31 and Figure 32).

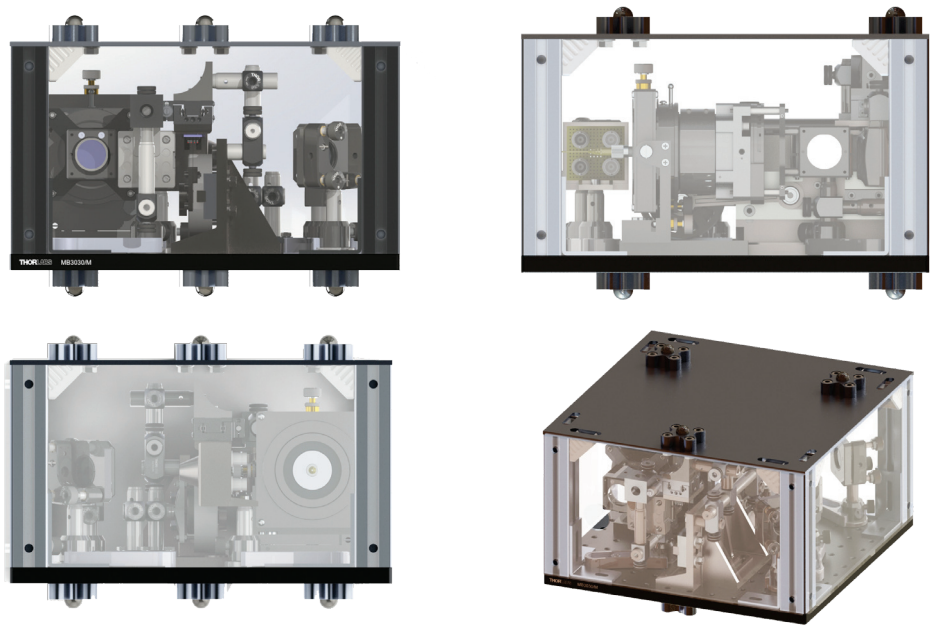

Figure 30. Some views of the rendered model of P3 prototype. Kinematic mounts are available on the top and bottom surfaces to enable reversal if required.

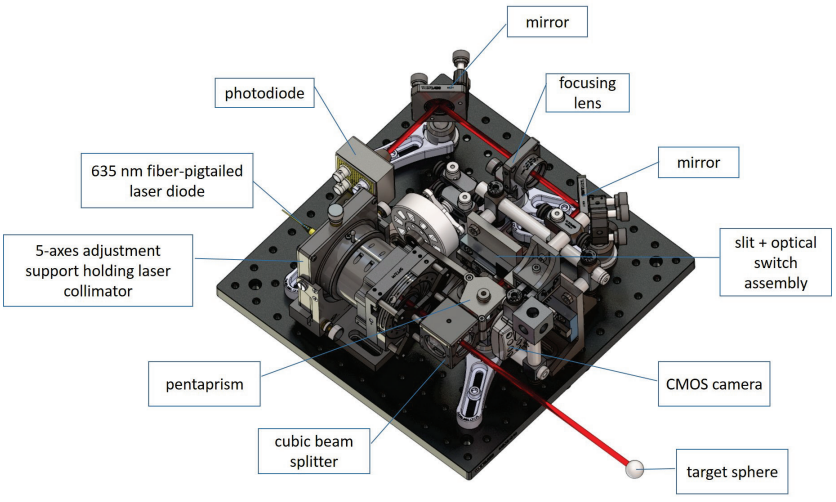

Figure 31. Rendered interior of P3, with the key components mounted on breadboard.

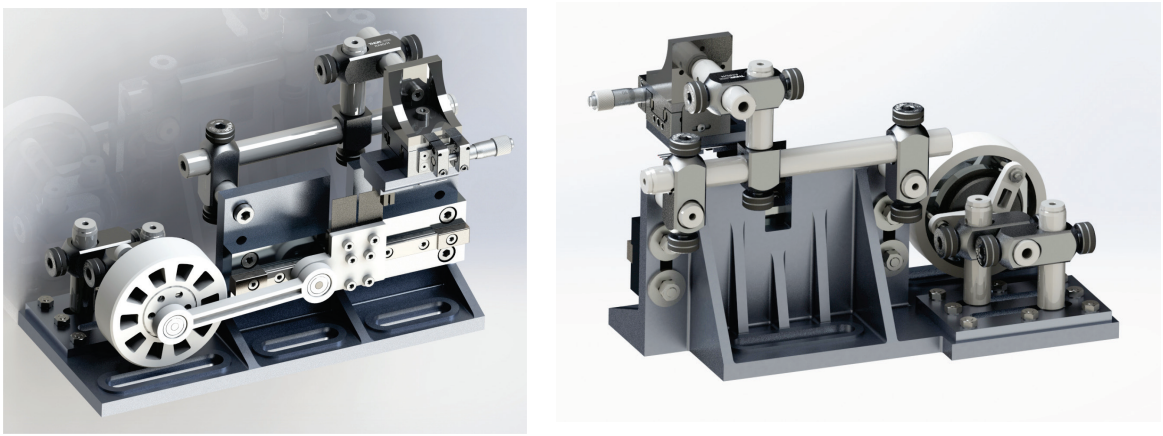

Figure 32. Front and back view of the rendered slit-optical switch assembly, with slider-crank linkage driven by hard disc motor.

P3 underwent a more thorough test than the previous prototypes. As well as the other straightness measurement devices, P3 compared a tested profile with a reference line; in our case, the reference line was the paraxial ray impinging on the sphere and backscattered from the same sphere, with the laws of Physics ensuring that the light rays are enough straight (in our distance range) at a high degree of accuracy. As the distance of the target varied, the peaks of the photodiode signal changed their shape, risking to introduce a systematic contribution in their processing; for this reason, taking advantage of a nearly perfectly straight stroke — the CMM carriage stroke —, P3 measured the straightness error of a virtually perfect straight line: each deviation from a zero indication should have been attributed to a systematic error of the instrument reference line. A high accuracy CMM (Leitz PMM-C 10 12107) available at INRIM was used for this validation. The longest usable stroke was 1.2 m, which fixed the maximum distance of the target. The device was hence installed on the CMM basement and the target attached to a stage with micrometer screws, with the position of the sphere measured by a high precision LVDT (Figure 33).

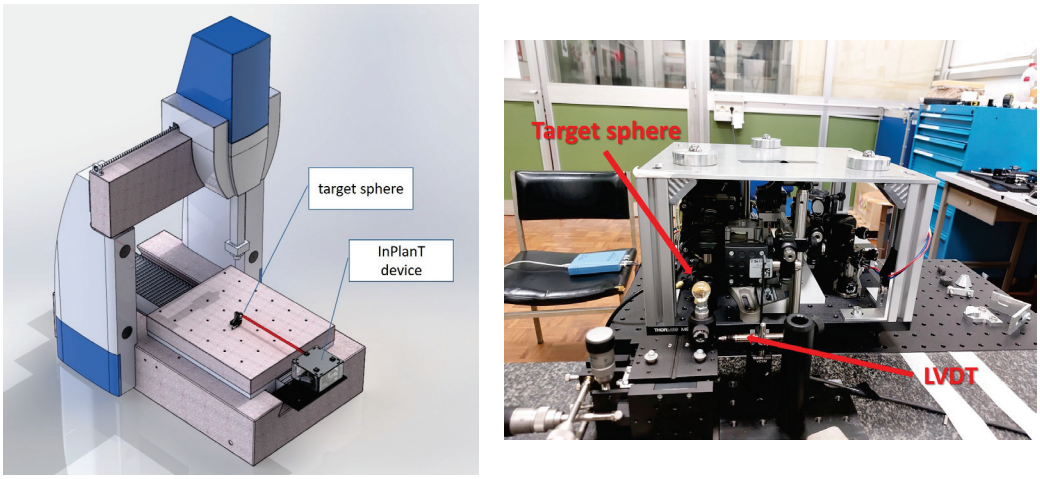

(**a**) (b)

Figure 33. (a): Render of the testing set up of P3, installed on the CMM; (b): view of the physical realization on the prototype mounted in the CMM, at INRIM facility.

In order to estimate the combined effects of the air turbulence in the laboratory and the vibrations generated by the slider-crank mechanism, an investigation was carried out consisting in the acquisition of the pattern of the backscattered signals by means of a CMOS camera, integrated into the device; the observation and the consequent processing of the images confirmed the need for averaging the signals, because of unavoidable micrometric fluctuations noticed during the test at different distances of the target: the plot in Figure 34 shows the coordinates of the image centers of mass ("CdM") with a still CMM at three different distances of the target (d = 0 mm, d = 600 mm, d = 1200 mm). The dispersion of the CdMs increases with the target distance: the calculated pooled standard deviations of the spots coordinates are $\sigma_{0\ mm}^{pooled} = 1.6\ \mu m$, $\sigma_{600\ mm}^{pooled} = 3.2\ \mu m$, $\sigma_{1200\ mm}^{pooled} = 4.3\ \mu m$.

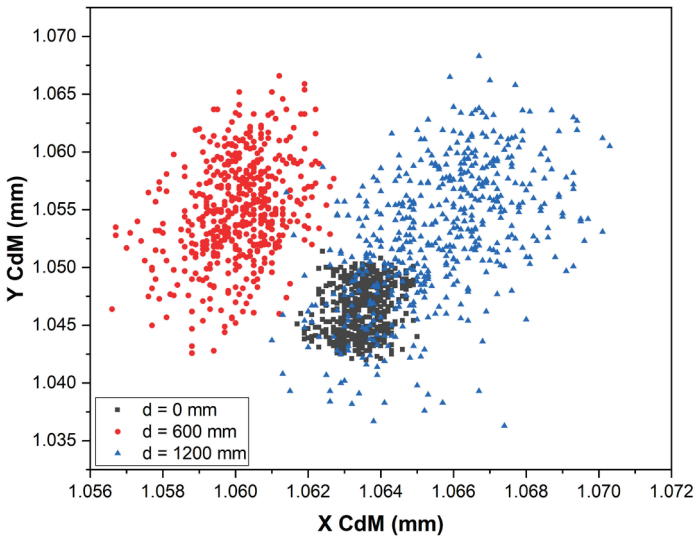

Figure 34. Detection of the combined effects of mechanical vibrations and air turbulence on backscattered images from the sphere. By performing an Orthogonal Distance Regression of the centers of mass of the three separate point clouds, the peak-to-valley straightness deviation can be quantified in ≃ 4.6 µm.

The alignment procedure of the device with respect to the CMM stroke was achieved by placing a flat object (typically a piece of paper) beyond the sphere, and keeping the attention fixed on the thin halo generated by the peripheral portion of the impinging beam; the absence of any relative movement of the same halo over the whole stroke was considered as satisfactory for the alignment. The conversion of the signal phase measurement into a lateral displacement measurement of the target was possible through calibration, in the following manner: with a least-squares best fit method, the linear response of the instrument was evaluated in 5 lateral positions of the target, 0.5 mm apart from each other, to cover a range of ±1 mm; this approach was repeated at 5 different distances of the sphere, in steps of 300 mm, to cover the whole range of (0 ÷ 1200) mm, so that at the end of the process a grid of points in a (2 × 1200) mm^2 region of space was available to be interrogated by a Python script in data post processing. Figure 35 and Table 4 show

that the sensitivity was quite stable over the full range of distances between device and target. The calibration lines proved to be essentially parallel to each other, but spread vertically, and this could be explained admitting a slight misalignment of the beam pointing on the target with respect to the CMM stroke; in addition to that, it must be kept in mind that the return beam is known to suffer a slight divergence (32): for this reason, even in presence of a perfectly collimated forward beam impacting on the target, the return beam cannot be schematized with just a single direction.

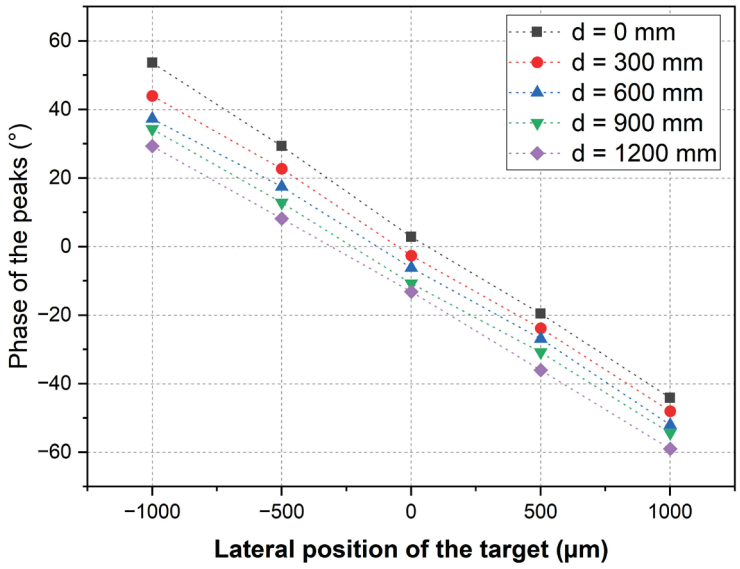

Figure 35. Calibration curves (in the phase domain instead of time domain, as in Figure 29) of P3 at different distances to the sphere.

Target distance ***d*** / mm	**Sensitivity** ***k*** / (10^{-3} °/µm)	**Intercept** / °	**R^2**
0	−48.9 ± 0.6	4.43 ± 0.47	0.9993
300	−46.1 ± 0.7	−1.53 ± 0.50	0.9991
600	−44.6 ± 0.9	−6.04 ± 0.68	0.9981
900	−44.2 ± 0.6	−9.73 ± 0.41	0.9993
1200	−44.2 ± 0.5	−14.11 ± 0.37	0.9994

Table 4. Results of the linear best fitting of the calibration data for P3.

The calibration results were then used in actual measurement, in this way: given a distance to the sphere, the curves in correspondence with the immediately longer and shorter distances (in the calibration table) were used to get two lateral displacements, in order to derive the actual device instrument indication as an interpolation between them.

The next step consisted in an independent scan of the full CMM stroke in 24 points in steps of 50 mm; for each step, the device indication was calculated by interpolation, as described above. Three different strategies of straightness deviation calculations were adopted, with different reference line (and consequent

peak-to-valley straightness deviations "STRt"): the least-squares reference line LS, the reference line joining the extreme points, and the mean minimum zone reference line MZ (36) (Figure 36).

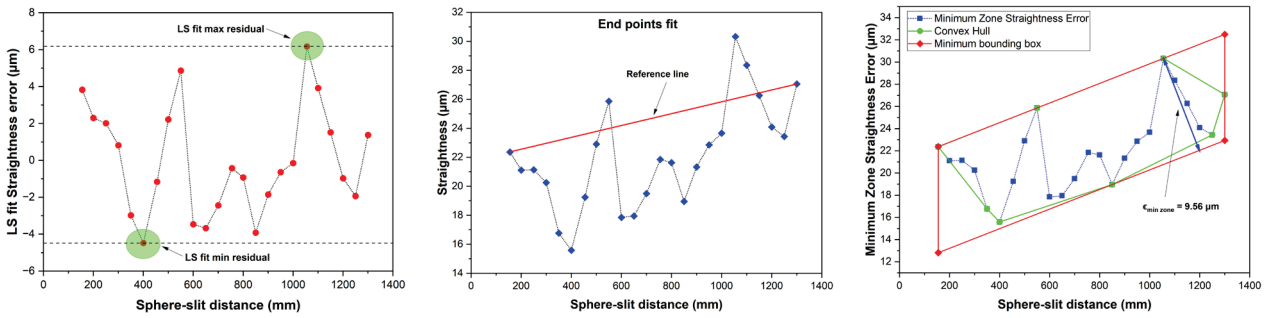

(a) (b) (c)

Figure 36. Characterization of the internal reference line for P3. Plots of the derived straightness deviations vs. the distance to target, with 3 different strategies: LS fit (a), end points fit (b) and minimum zone fit (c).

Reference Line	**Peak-to-Valley Straightness Deviation (STRt)** / µm
Least squares (LS)	±5.3
End points	±6.0
Mean minimum zone (MZ)	±4.8

Table 5. Calculated peak-to-valley STRt values.

In order to justify our choice of taking the CMM carriage stroke as a reference for the derivation of the instrument indication error, a direct measurement of the effective stroke straightness was performed with a comparison technique. An approach similar to the previous measurement was adopted, with a 5 MPix CMOS camera (with 2.2 µm pixel size) replacing the sphere and a Renishaw RLU10 laser unit as a source[8]: from the migrating center of mass of the laser spot (whose profile proved to be mantaining its simmetry along the investigated range) detected by the camera, the sought information on the "real" straightness deviation of the stroke were extracted. To reduce the impact of the air turbulence, the camera acquired the laser spot at 6 Hz for 100 s, and the centers of mass of the frames were averaged. The same positions explored by the sphere in the previous experiment were sampled by the camera. In Figure 37 a plot shows the results, and it is worth mentioning the fact that the first portion of the stroke (< 900 mm) is characterized by stable and plausible results, while the last portion is affected by oscillations due to the air turbulence (since we are sampling regions of space that are the furthest form the device); for this reason, it is correct to affirm that the straightness of the CMM X-

[8] https://www.renishaw.com/en/rlu-compact-laser-unit-with-fibre-optic-delivery--20999

carriage can be assessed within ±0.5 µm, which confirms the assumption of a nearly perfectly linear (for our needs) stroke.

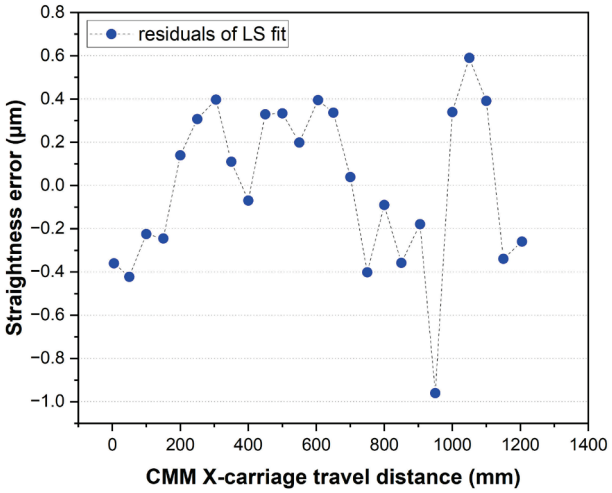

Figure 37. Straightness deviation of the CMM X-carriage. The LS fit reference line was subtracted, and the horizontal axis represents the stroke.

2.3 Last mechanical upgrade: tests and results

With the aim of improving the performances of the devices, some updates to the mechanical assembly were designed and implemented. Specifically, the heart of the slit driving mechanism — crank and connecting rod— consisted of 3D-printed elements linked together by a ball bearing, and another bearing allowed the linkage of the crank to the slit support: this chain of elements proved to be susceptible to wear out over time, due to the dynamic friction and to poor geometric accuracy inherent in the production process (fused deposition modeling); the clearance between the components caused by imperfect coupling had an impact on the signals to be processed, generating inconsistencies in their processing. A viable solution to this problem was seen in the replacement of the critical plastic parts and in a sturdier design of the mentioned components, machining them in solid aluminum and paying attention to their tolerances and ensuring better accuracy in their assembly (Figure 38); also the old bearings were replaced by a high quality pair of new bearings, in order to achieve maximum fluidity in the rotation and smoothness in the slit motion.

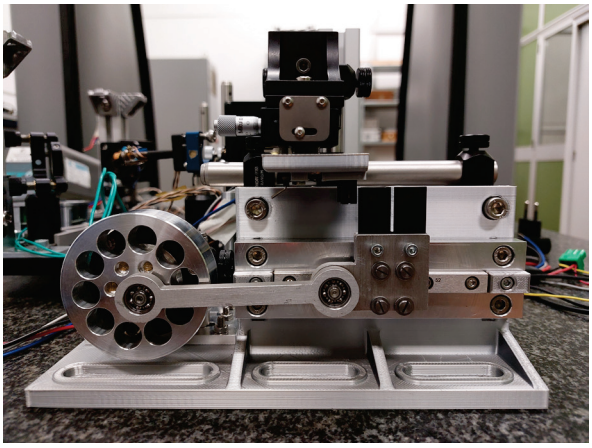

Figure 38. Picture showing the new aluminum machined parts, held in place by an oversized 3D printed plastic support.

Great care was also taken in the installation of the flywheel on the motor rotor, trying to minimize the runout error: a 120° service setup with bearings supported by micrometric screws and a LVDT making contact on the edge of the flywheel was equipped and tested as the screws were tightened (Figure 39); by iteratively tuning the assembly procedure, it was possible to achieve a ~ 60 µm maximum runout error (measured in 180° rotation of the flywheel itself) (Figure 40).

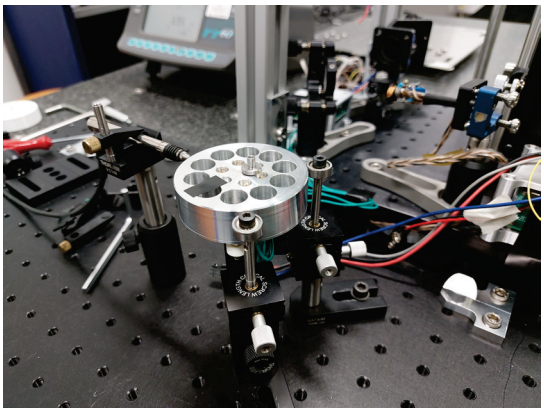

Figure 39. Set up for minimizing the run out error.

Figure 40. Minimum (on the left) and maximum (on the right) run out error in the flywheel installation.

At the end of the process, these mechanical efforts were paid off both in the nearly total absence of clearances (witnessed by a considerably reduced noise in working regime), and in an improved transmission of the motion to the slit.

2.3.1 Jitter evaluation

After the described step, in order to achieve a better knowledge of our device under a wide range of testing conditions before the necessary subsequent new calibration, we decided to investigate the observed frequency jitter in the acquired signals, inevitably occurring during the measurement process. As it is known in literature, jitter is a phenomenon affecting the correct interpretation of the electronic signals (Figure 41); it can be defined as a "deviation of significant instances of a signal from their ideal location in time" (37).

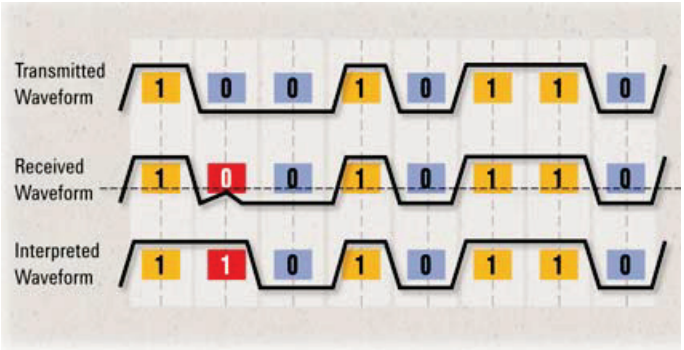

Figure 41. Possibility of misinterpretation of transmitted data due to jitter (source: (37)).

By convention, two categories identify the amount of timing variations, and they are known as jitter and wander on the base of the Fourier analysis: timing variations occurring at a slow rate are called wander, while jitter is related to variations occurring more rapidly; according to ITU-T Recommendation G.810 (08/96) "*Definitions and Terminology for Synchronization Networks*", the threshold separating wander from jitter is defined to be 10 Hz.
Often the sources of jitter can be placed into two distinct categories: bounded and unbounded, with the former reaching maximum and minimum phase deviation within a recognizable time interval, and the latter not capable of achieving the same behaviour within any time interval, theoretically approaching infinity; these types of jitter are respectively referred to as "deterministic" and "random" jitter. The total jitter on a signal, characterized by a phase error function $\varphi_i(t)$, is the cumulative sum of the aforementioned contributions:

$$\varphi_i(t) = \varphi_j(t)^D + \varphi_j(t)^R$$

In this equation, $\varphi_j(t)^D$, the deterministic component (distinguished by peak-to-peak value ${J_{PP}}^D$) can be calculated by summing maximum and minimum

phase/time displacements produced by bounded jitter sources together; the random component $\varphi_j(t)^R$ (related as a standard deviation value ${J_{RMS}}^R$ and assumed to follow a Gaussian distribution), is generated by all random noise sources shaping the signal. In this work there is no intention to explore extensively the concept and to propose a rigorous procedure to separate deterministic from random jitter in the collected signals, nevertheless an estimation of the overall jitter affecting the subsequent handling of the collected data can be an interesting exercise; our measurand is just the temporal displacements of the signals backscattered by the target, in a condition where the trigger for their acquisition is the "on/off" signal provided by the optical switch due to the rotation of the motor: an uneven rotation speed is responsible for adding unwanted noise in the time displacement measurement, and leading to under- or overestimating the calculated straightness error at the end of the process. In order to accomplish this task, the behaviour of the *period jitter* (that is the deviation of any clock period from its mean clock period within an observation window, therefore comparing the length of each period to the average period of an ideal clock), among the other forms of jitters (like *cycle-cycle jitter* and *time interval error* – TIE), was chosen for this investigation (Figure 42).

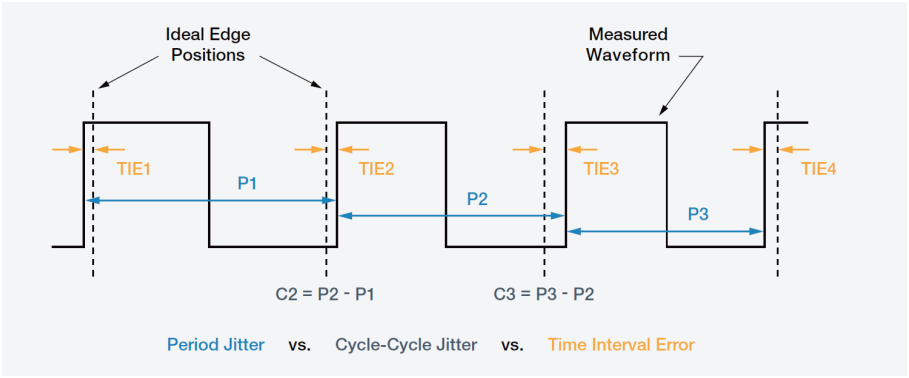

Figure 42. Different ways to measure the jitter (source: (38))

The acquisition settings for this test are shown in Figure 43; briefly, a collection of 1000 waveforms (containing at least an entire period of the square wave) were saved, each one storing 10000 samples at a frequency of 100 kHz in a time interval of 100 ms for each waveform, with a resolution of 10 µs; rotation speed of the motor during the test was set at 15 Hz, approximately.

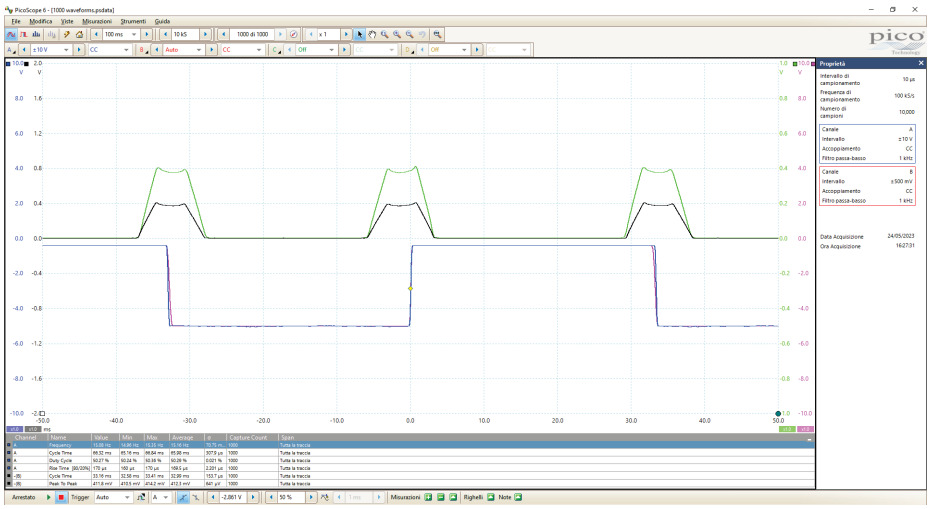

Figure 43. Acquisition settings chosen for jitter measurement.

By using a custom-made Python script working on all the collected waveforms, the rising and the descending fronts of the square waves were isolated and resolved in time in order to provide the periods on which statistical evaluations were performed, allowing to estimate the jitter affecting the signals. Figure 44 shows a plot of both the clock periods (roughly ranging from 65 ms to 67 ms) and the period jitter (in the approximate interval of ±1 ms), with the latter obtained by filtering out the DC component of the raw clock signal.

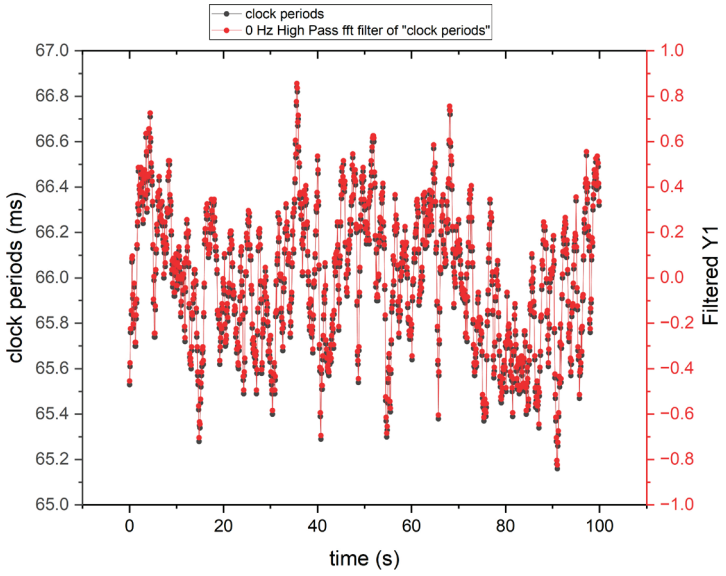

Figure 44. Plot of the clock periods (in black) and of the period jitter (in red), 1000 waveforms.

By performing a gaussian fitting of the filtered data points over the whole time interval (100 s) and performing a multiple peak analysis, the plot in Figure 45 could be generated.

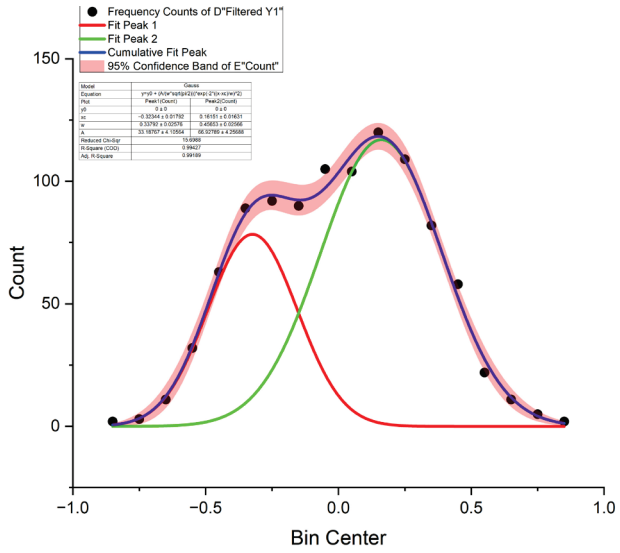

Figure 45. Multiple peak analysis of the filtered data points in a 100 s time interval. Horizontal scale is in ms.

Simple statistics on collected data (spread over 18 bins, ranging from -0.9 to 0.9 ms) suggested to be in presence of a distribution characterized by a bimodal nature rather than a single Gaussian curve, and allowed to create a histogram of the period jitter (Figure 46); this behaviour is typical of a signal affected by both random and deterministic jitter: the confirmation of this assumption lies in the evaluation of the power spectral density (PSD) of the same signal (Figure 47), where two peaks can be isolated in the 0 – 5 Hz band: the first at about 0.49 Hz (corresponding to a modulating signal with a periodicity of ~ 2 seconds, clearly visible during the real time acquisitions of samples), and another at ~ 3.6 Hz, pertinent to a weaker modulation; both of the modulating signals are likely generated by the motor driver, in the absence of any other mechanical or electric perturbative source. Figure 48 shows the Allan deviation of the filtered jitter period.

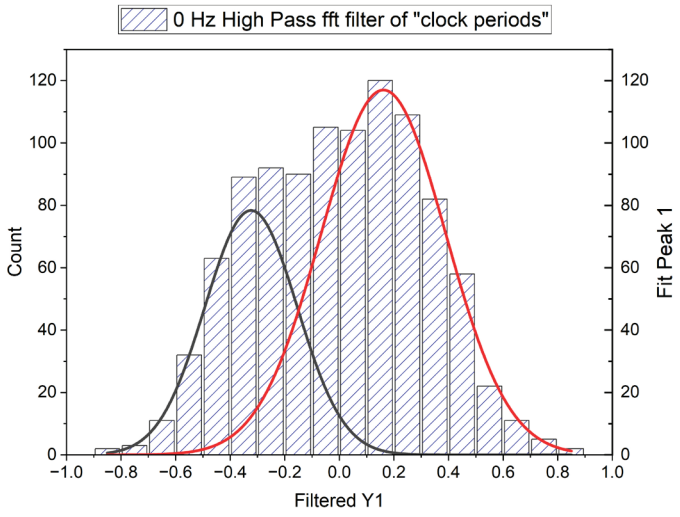

Figure 46. Histogram of the period jitter for the 1000 waveforms acquired.

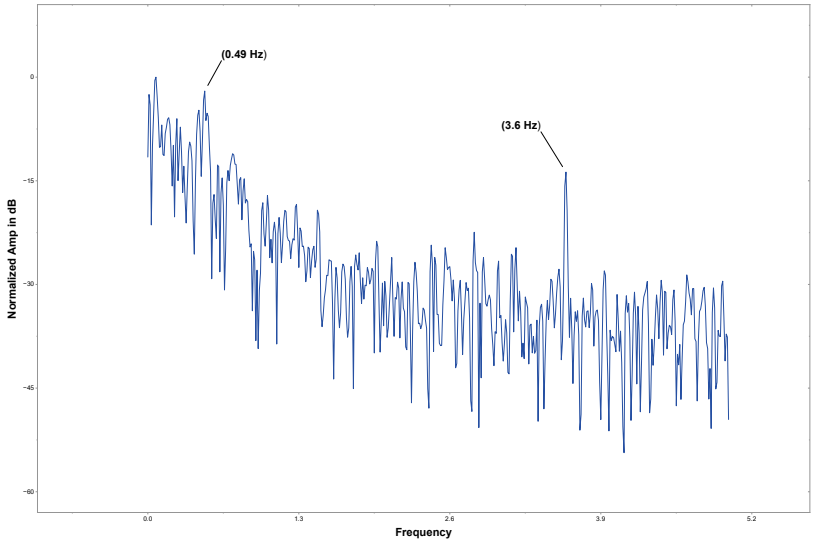

Figure 47: PSD of the period jitter signal, with two peaks (at 0.49 Hz and 3.6 Hz) which can be discerned above the noise.

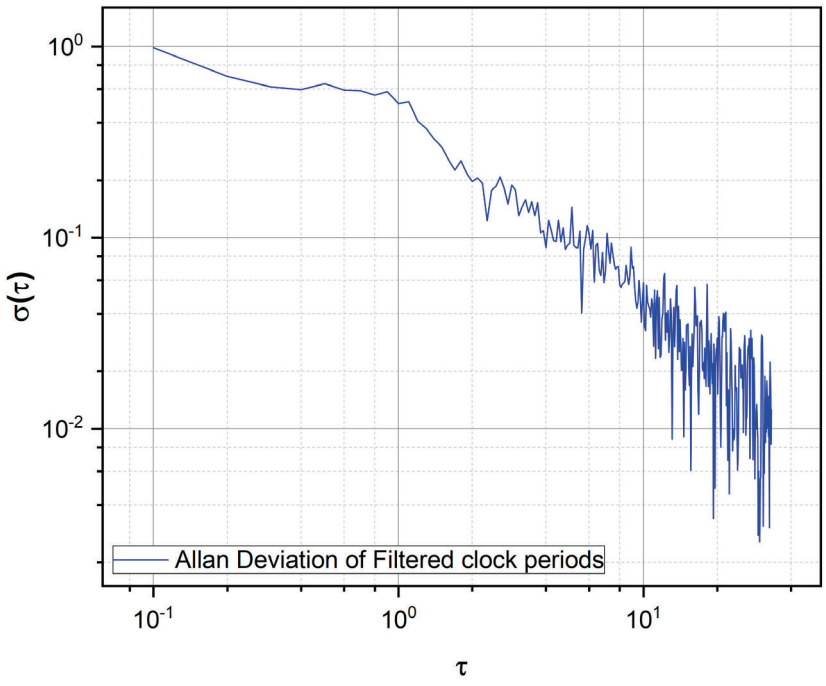

Figure 48. Plot with Allan deviation of the period jitter examined in 1000 waveforms.

Peak-to-peak deterministic jitter ${J_{PP}}^{D}$ (39) can be evaluated by taking into consideration the distribution in the histogram plotted in Figure 46: performing some statistics on it allowed to estimate its contribution in 1.68 ms, while the random jitter J^R shows to be represented by a Gaussian curve with a 0.46 ms standard deviation; this means that the total peak-to-peak jitter, assuming a bit error rate (BER) of 10^{-3} (just one over 1000 samples), can be estimated by the formula:

$$J_{total} = RMS\ Multiplier \times J^R + {J_{PP}}^{D} \cong 4.52 \text{ ms}$$

BER	RMS Multiplier Data, "DTD=0.5"	RMS Multiplier Clock, "DTD=1"
10^{-3}	6.180	6.582
10^{-4}	7.438	7.782
10^{-5}	8.530	8.834
10^{-6}	9.507	9.784
10^{-7}	10.399	10.654
10^{-8}	11.224	11.462
10^{-9}	11.996	12.218
10^{-10}	12.723	12.934
10^{-11}	13.412	13.614
10^{-12}	14.069	14.260
10^{-13}	14.698	14.882
10^{-14}	15.301	15.478
10^{-15}	15.883	16.028

Table 6. BER with its Appropriate RMS Multiplier.

(choosing the RMS multiplier from first column of Table 6 (40)).

In order to have a more robust statistic and to improve the resolution in the same frequency band, with the aim of better estimating the amount of jitter disturbing our measurements another test was performed; this time, each acquisition file consisted in 2000 samples (100 ms each one) of the signal clock, sampled at 20 kHz and with a resolution of 50 µs, for a total of 8192 waveforms containing at least a whole period of the square wave: these settings matched the maximum amount of data that could be acquired due to the limited buffer size of the Picoscope). By applying the same methodology described before, the results of the acquisitions are shown in Figure 49, Figure 50, Figure 51, Figure 52 and Figure 53.

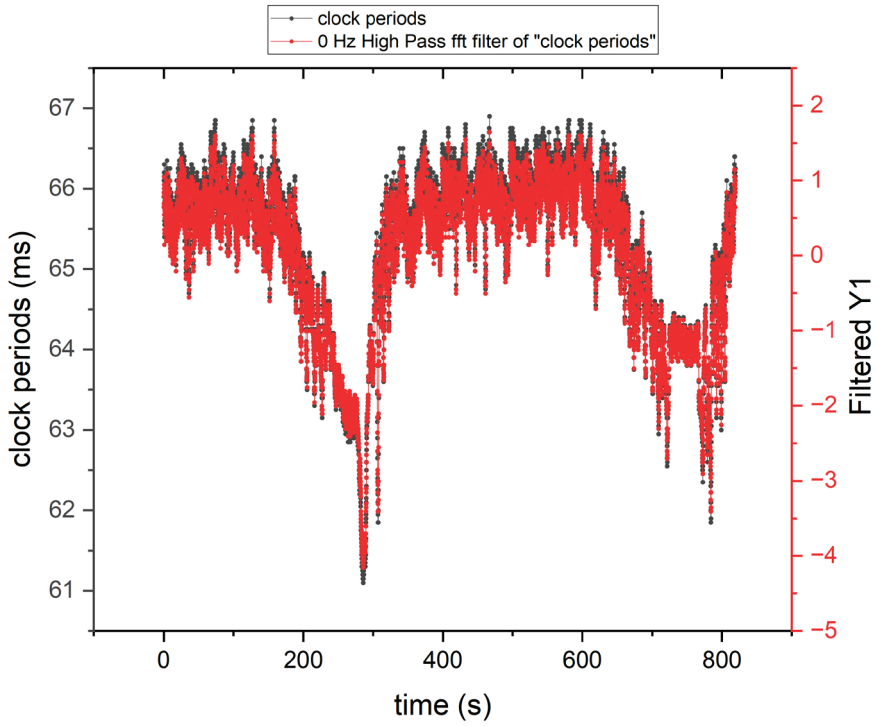

Figure 49. Plot of the clock periods (in black) and of the period jitter (in red), 8192 waveforms.

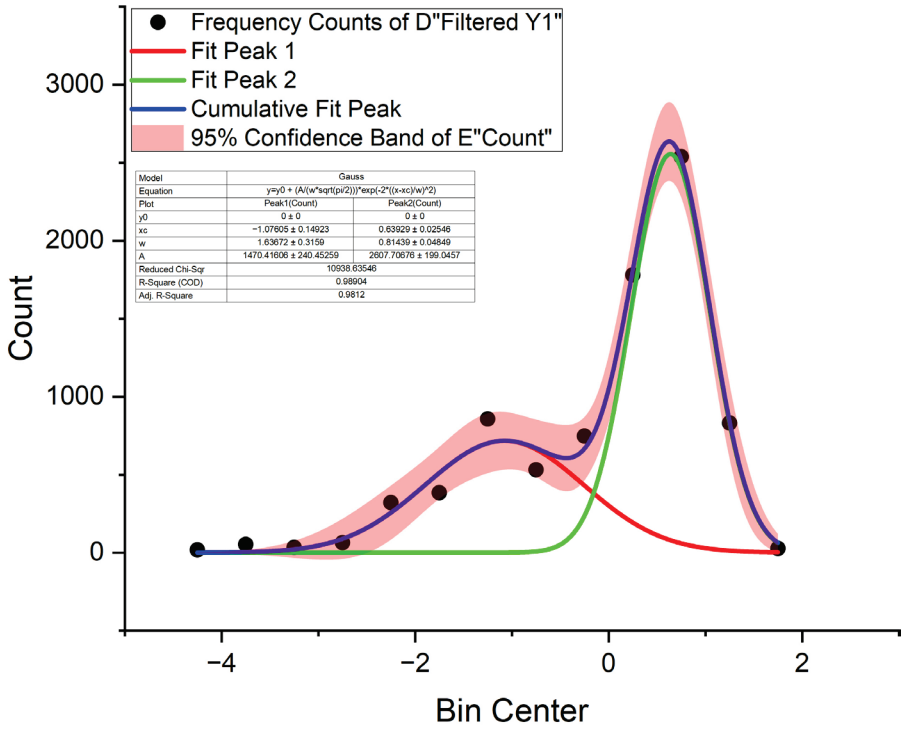

Figure 50. Multiple peak analysis of the filtered data points in a 819 s time interval.

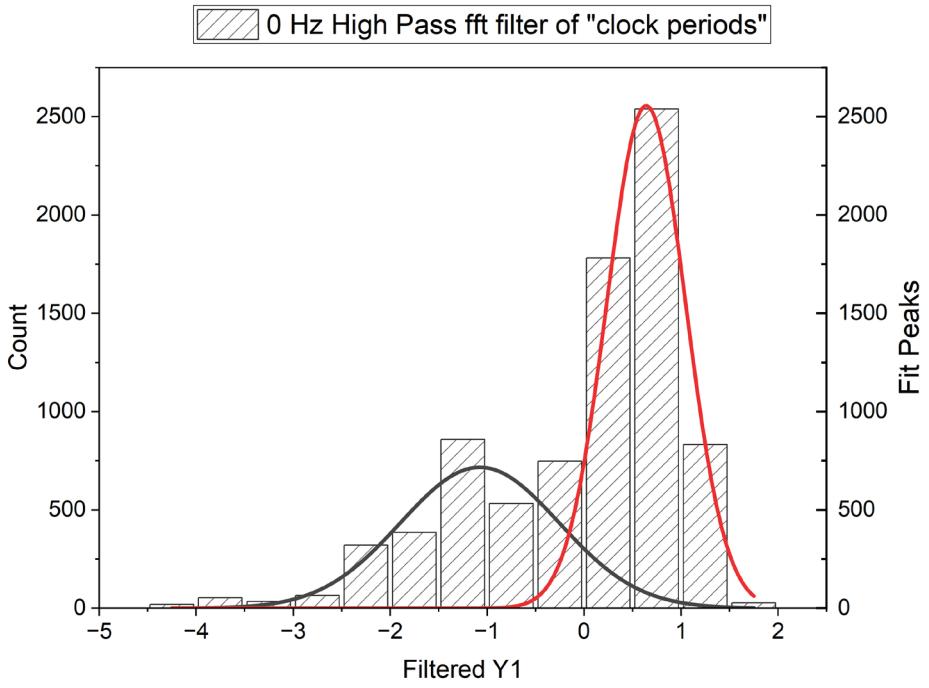

Figure 51. Histogram of the period jitter for the 8192 waveforms acquired.

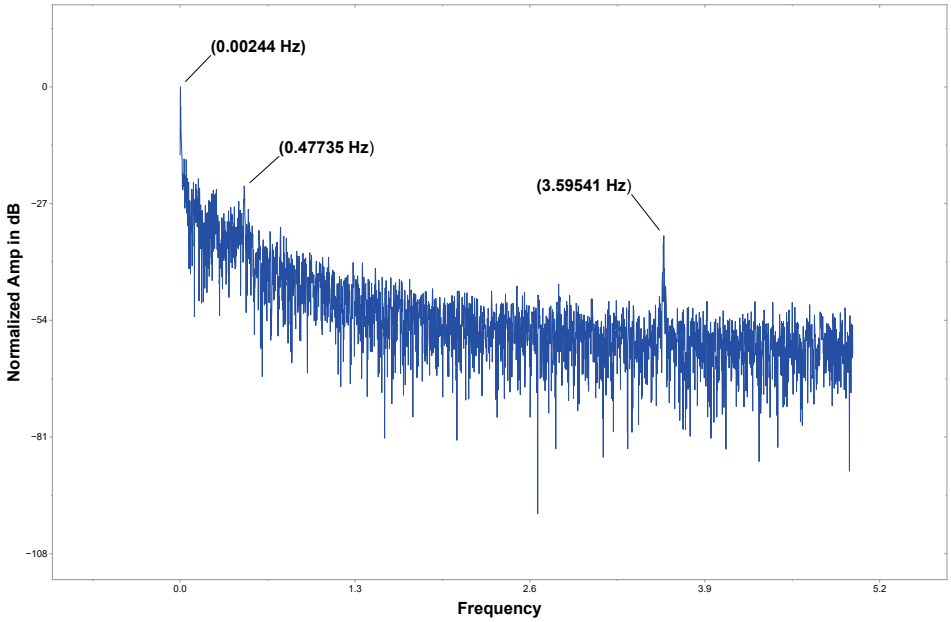

Figure 52. PSD of the period jitter signal, with three peaks (at 0.002 Hz, 0.477 Hz and 3.595 Hz) standing out above the noise.

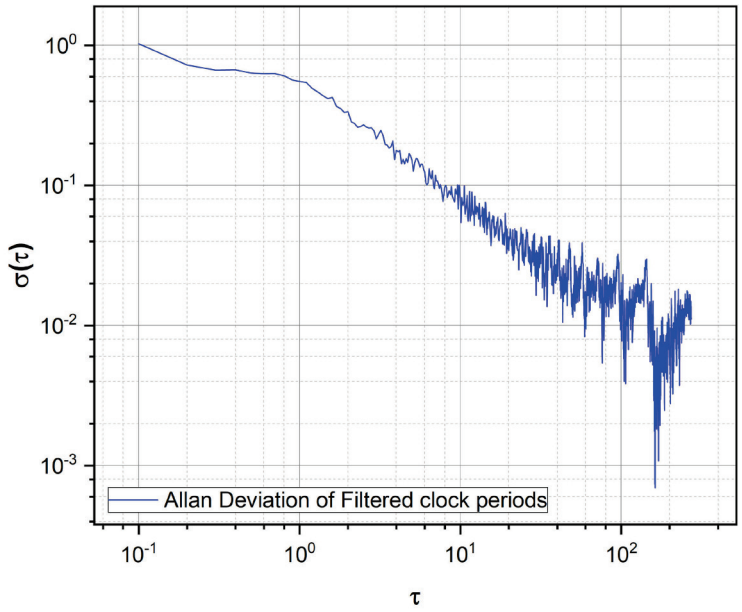

Figure 53. Plot with Allan deviation of the period jitter examined in 8192 waveforms.

PSD of the new data confirm the same deterministic component in the jitter, at the same frequencies of ~ 0.48 and 3.6 Hz as seen before, and the appearance of a new strong peak at lower frequency, at 0.002 Hz, accounting for a slow modulation of the clock signal by means of a perturbation with a period of ~ 410 s (also barely visible in the PSD of the period jitter signal in Figure 47). Overall jitter contributions can be estimated by adding together deterministic and random components, with the same formula used before:

$$J_{total} = RMS\ Multiplier \times J^R + {J_{PP}}^D \cong 11.82 \text{ ms}$$

with $RMS\ Multiplier = 7.438$ (from Table 6), $J^R = 0.81\ ms$ and ${J_{PP}}^D = 5.8$ ms

For what concerns the acquisitions effectively used for the characterization of the upgraded device, it was established that a population of only 100 samples of both the clock and the cross-correlation signal should be collected in order to perform the necessary calculations (that will be explained in the next paragraph); with such a poor resolution the distinction of the two components of the jitter resulted very difficult (Figure 54, Figure 55, Figure 56), however leading to an estimation of ${J_{PP}}^D$ in 0.5 ms and of J^R in 0.18 ms; choosing a *RMS Multiplier* equal to 4.653 (corresponding to the probability error of 0.01 (41)), total jitter could be estimated in 1.34 ms: this quantity can be seen as a rough estimation of the main contribution to uncertainty in the evaluation of the cross-correlations of the even and odd peaks of the windowed photodiode signals, triggered by the clock signal.

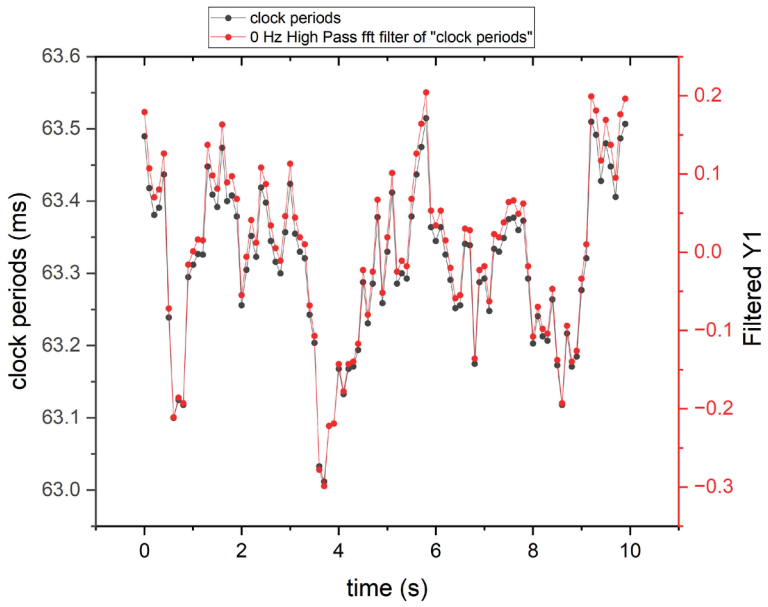

Figure 54. Plot of the clock periods (in black) and of the period jitter (in red), 100 waveforms.

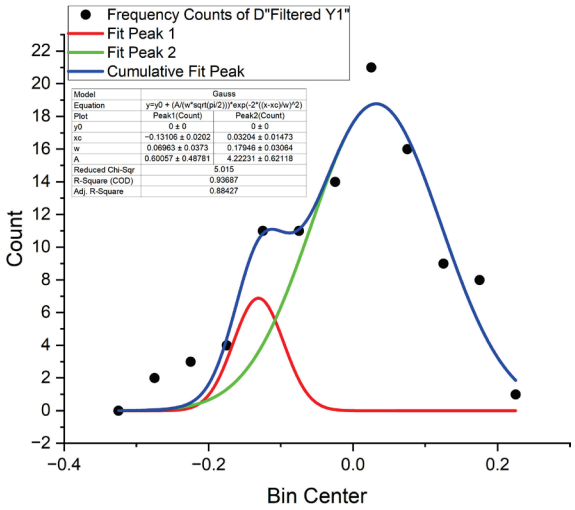

Figure 55. Multiple peak analysis of the filtered data points in a 10 s time interval.

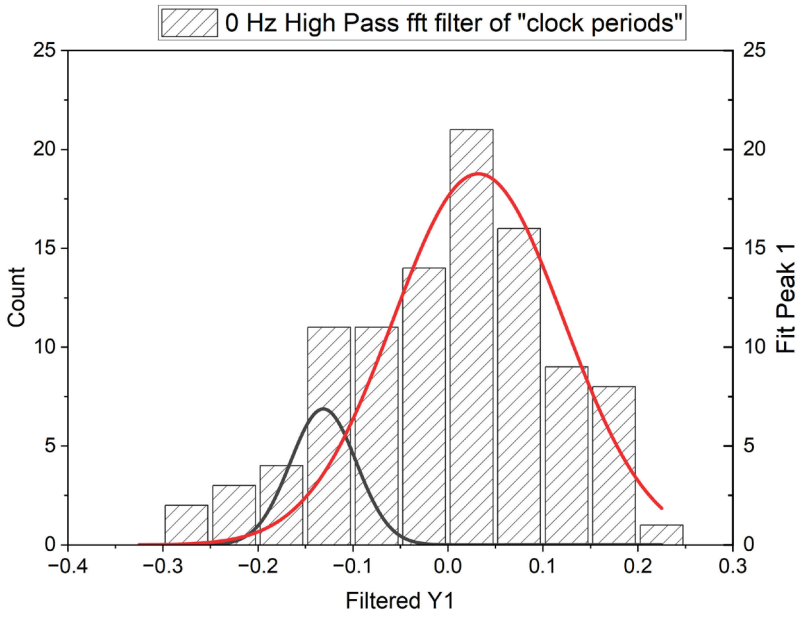

Figure 56. Histogram of the period jitter for the 100 waveforms acquired.

2.3.2 Calibration procedure

Clock signals revealed to be affected by jitter, whose composite nature allowed it to be separated into deterministic and random contributions; they were quantified with a statistic approach in different test conditions, in order to provide a basis for an estimation of the uncertainty occurring in our measurements. Since crossing the 50 % threshold of the clock signal maximum amplitude was the trigger for the acquisition of the photodiode signal, the presence of jitter inexorably affected the timestamps of the calculated cross-correlations of the photodiode signal, introducing some unwanted noise in the subsequent calculations. In order to face this problem, the coherence of clock and cross-correlation signals was evaluated; clock and photodiode signals are normally in a specific phase relation —ideally constant in time—, depending on the lateral position of the target, but clock and cross-correlation signals disclose their synchrony when plotted together (Figure 57).

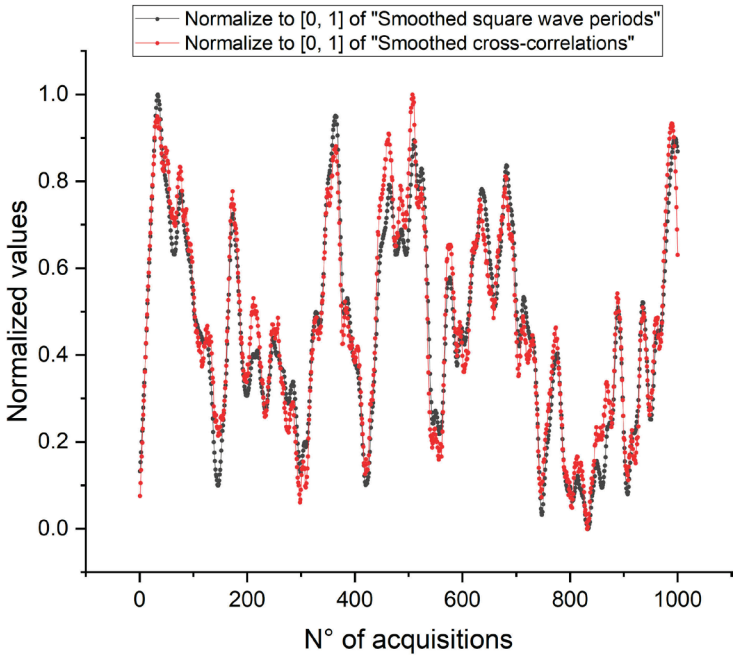

Figure 57. Plot of smoothed and normalized clock and cross-correlation signals (data coming from same acquisition of the same 1000 samples described in the previous paragraph).

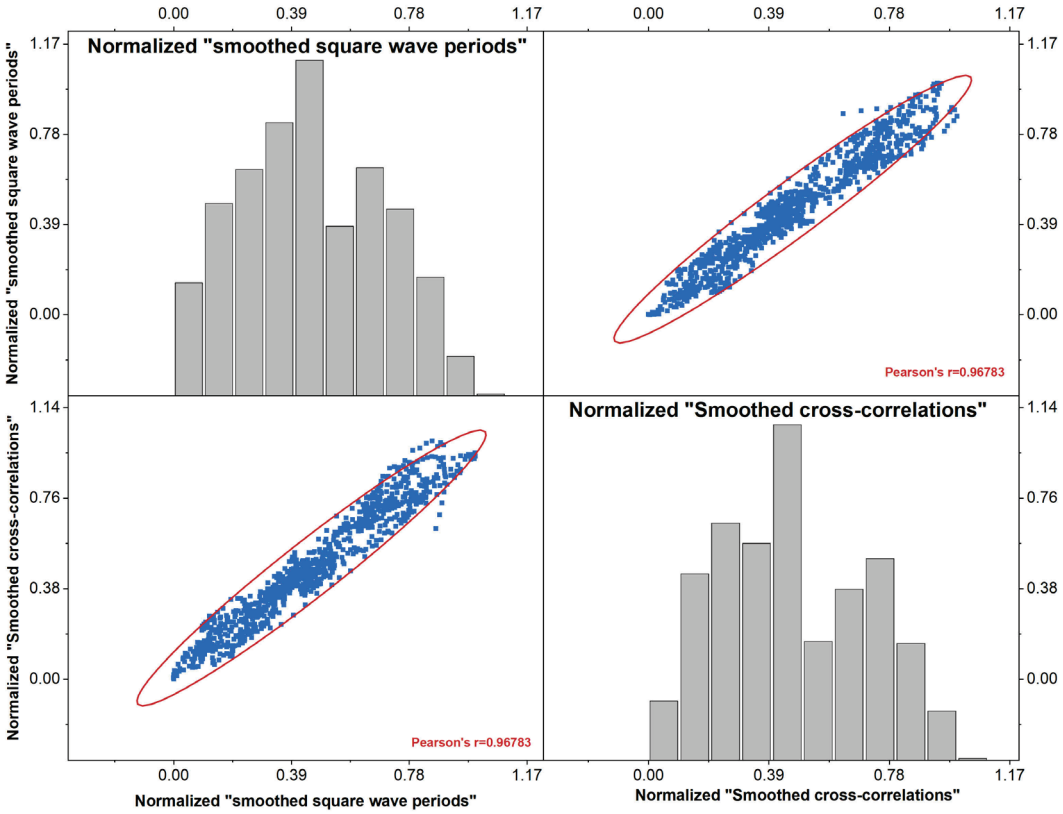

Figure 58. Scatter matrices of clock and cross-correlation signals, with 95 % confidence ellipse and histograms of the couple of distributions on the diagonals.

Scatter matrices of these signals (Figure 58) point out the strong correlation between them, also confirmed by the Pearson's r coefficient ($\cong 0.97$); this awareness allows us to define another measurand, that turned out to be eligible to replace the rough cross-correlation signal used so far for calibrating the device: the cross-correlations normalized on the clock signal periods, so that the noise induced by the jitter even in presence of a still target tends to be cancelled out by averaging on a sufficient amount of acquired waveforms of both clock and photodiode signals. Adopting such a strategy, the main contribution to the dispersion of the calculated values of the new measurand is the turbulence of air, that cannot be compensated and is primarily responsible for adding totally random components to the collected photodiode signals; an upgraded Python script (reported in Appendix A, with its flowchart in Figure 73) takes this necessary modification into account, generating the sought outputs.
Also in the context of this calibration process, five mutual distances between target and device were investigated, ranging from 0 mm to 1200 mm (plus a constant offset of 470 mm, due to the experimental layout equipped on the CMM, as shown in Figure 59), with the sphere occupying five different lateral positions (from - 500 µm to 500 µm) to unbalance the system and trigger the straightness sensitivity of the instrument; the overall strategy can be schematized in the generation of a grid of 25 calibration points sampling a narrow rectangle of space (1 mm wide and 1200 mm long) explored by the sphere in the process (Table 7).

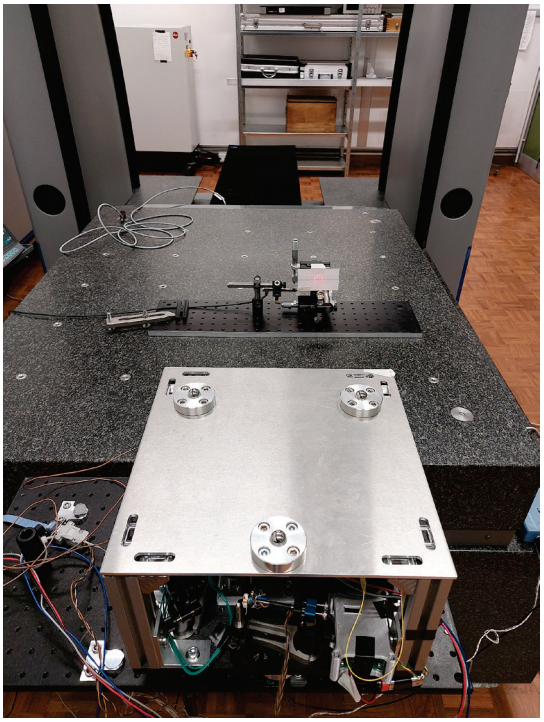

Figure 59. Set up on the CMM and initial position ($d = 0$ mm, "null" lateral displacement of the sphere) for the calibration of the device.

Lateral sphere displacements (μm)	d = 0 mm									
	Photodiode signal (V)	t_clock (ms)	σ_{t_clock} (ms)	t_cross-corr (ms)	$\sigma_{t\_cross-corr}$ (ms)	t_cross-corr/t_clock	$\sigma_{t\_cross-corr/t\_clock}$	f_clock *(Hz)*	Δϕ *(°)*	Pearson
-500	6.31E-01	6.64E+01	2.78E-01	-6.42E+00	3.23E-02	-9.66E-02	2.67E-04	1.51E+01	-1.74E+01	9.91E-01
-250	6.35E-01	6.65E+01	2.22E-01	-4.31E+00	1.97E-02	-6.48E-02	2.18E-04	1.50E+01	-1.17E+01	9.58E-01
0	6.08E-01	6.63E+01	3.11E-01	-2.13E+00	1.85E-02	-3.21E-02	2.43E-04	1.51E+01	-5.77E+00	8.97E-01
250	6.47E-01	6.63E+01	3.25E-01	5.04E-02	1.95E-02	7.60E-04	2.93E-04	1.51E+01	1.37E-01	5.72E-01
500	6.52E-01	6.66E+01	2.57E-01	2.22E+00	2.00E-02	3.33E-02	2.77E-04	1.50E+01	6.00E+00	8.71E-01

Lateral sphere displacements (μm)	d = 300 mm									
	Photodiode signal (V)	t_clock (ms)	σ_{t_clock} (ms)	t_cross-corr (ms)	$\sigma_{t\_cross-corr}$ (ms)	t_cross-corr/t_clock	$\sigma_{t\_cross-corr/t\_clock}$	f_clock *(Hz)*	Δϕ *(°)*	Pearson
-500	5.35E-01	6.67E+01	3.79E-01	-6.04E+00	4.13E-02	-9.06E-02	3.00E-04	1.50E+01	-1.63E+01	9.92E-01
-250	5.54E-01	6.59E+01	3.48E-01	-3.96E+00	2.76E-02	-6.01E-02	2.49E-04	1.52E+01	-1.08E+01	9.86E-01
0	5.42E-01	6.65E+01	3.01E-01	-1.96E+00	2.16E-02	-2.95E-02	3.04E-04	1.50E+01	-5.32E+00	6.37E-01
250	5.60E-01	6.65E+01	2.52E-01	1.37E-01	1.74E-02	2.05E-03	2.61E-04	1.50E+01	3.70E-01	4.07E-01
500	5.67E-01	6.65E+01	1.81E-01	2.26E+00	1.81E-02	3.40E-02	2.71E-04	1.50E+01	6.12E+00	3.74E-01

Lateral sphere displacements (μm)	d = 600 mm									
	Photodiode signal (V)	t_clock (ms)	σ_{t_clock} (ms)	t_cross-corr (ms)	$\sigma_{t\_cross-corr}$ (ms)	t_cross-corr/t_clock	$\sigma_{t\_cross-corr/t\_clock}$	f_clock *(Hz)*	Δϕ *(°)*	Pearson
-500	4.63E-01	6.64E+01	2.38E-01	-5.90E+00	2.93E-02	-8.88E-02	2.83E-04	1.51E+01	-1.60E+01	9.58E-01
-250	4.75E-01	6.64E+01	3.31E-01	-3.92E+00	3.07E-02	-5.90E-02	3.36E-04	1.51E+01	-1.06E+01	9.45E-01
0	4.76E-01	6.61E+01	3.16E-01	-1.84E+00	1.99E-02	-2.79E-02	2.80E-04	1.51E+01	-5.02E+00	6.48E-01
250	4.88E-01	6.67E+01	2.62E-01	2.20E-01	1.95E-02	3.30E-03	2.92E-04	1.50E+01	5.93E-01	-3.57E-01
500	4.88E-01	6.65E+01	1.87E-01	2.27E+00	1.98E-02	3.41E-02	2.91E-04	1.50E+01	6.14E+00	5.05E-01

Lateral sphere displacements (μm)	d = 900 mm									
	Photodiode signal (V)	t_clock (ms)	σ_{t_clock} (ms)	t_cross-corr (ms)	$\sigma_{t\_cross-corr}$ (ms)	t_cross-corr/t_clock	$\sigma_{t\_cross-corr/t\_clock}$	f_clock *(Hz)*	Δϕ *(°)*	Pearson
-500	4.09E-01	6.65E+01	2.85E-01	-5.74E+00	4.32E-02	-8.63E-02	4.47E-04	1.50E+01	-1.55E+01	9.70E-01
-250	4.19E-01	6.63E+01	2.66E-01	-3.77E+00	2.50E-02	-5.69E-02	2.89E-04	1.51E+01	-1.02E+01	9.67E-01
0	4.18E-01	6.64E+01	2.75E-01	-1.70E+00	2.70E-02	-2.56E-02	3.73E-04	1.51E+01	-4.60E+00	6.85E-01
250	4.31E-01	6.62E+01	2.21E-01	3.08E-01	1.77E-02	4.65E-03	2.68E-04	1.51E+01	8.37E-01	-9.78E-02
500	4.29E-01	6.65E+01	2.81E-01	2.31E+00	2.12E-02	3.47E-02	2.96E-04	1.50E+01	6.24E+00	7.59E-01

Lateral sphere displacements (μm)	d = 1200 mm									
	Photodiode signal (V)	t_clock (ms)	σ_{t_clock} (ms)	t_cross-corr (ms)	$\sigma_{t\_cross-corr}$ (ms)	t_cross-corr/t_clock	$\sigma_{t\_cross-corr/t\_clock}$	f_clock *(Hz)*	Δϕ *(°)*	Pearson
-500	3.66E-01	6.62E+01	2.88E-01	-5.55E+00	3.27E-02	-8.38E-02	3.39E-04	1.51E+01	-1.51E+01	9.27E-01
-250	3.80E-01	6.63E+01	2.83E-01	-3.51E+00	2.45E-02	-5.30E-02	2.80E-04	1.51E+01	-9.54E+00	9.39E-01
0	3.77E-01	6.64E+01	2.48E-01	-1.52E+00	2.73E-02	-2.28E-02	3.89E-04	1.51E+01	-4.11E+00	5.14E-01
250	3.89E-01	6.61E+01	3.81E-01	4.88E-01	1.70E-02	7.39E-03	2.55E-04	1.51E+01	1.33E+00	7.09E-01
500	3.85E-01	6.64E+01	2.82E-01	2.47E+00	2.28E-02	3.72E-02	3.03E-04	1.51E+01	6.70E+00	8.15E-01

Table 7. Results obtained by processing the acquired data of clock periods and photodiode signals in the 25 positions explored by the sphere during calibration; the occasional low or even negative values of the Pearson coefficient may indicate some turbulence perturbating the acquisitions.

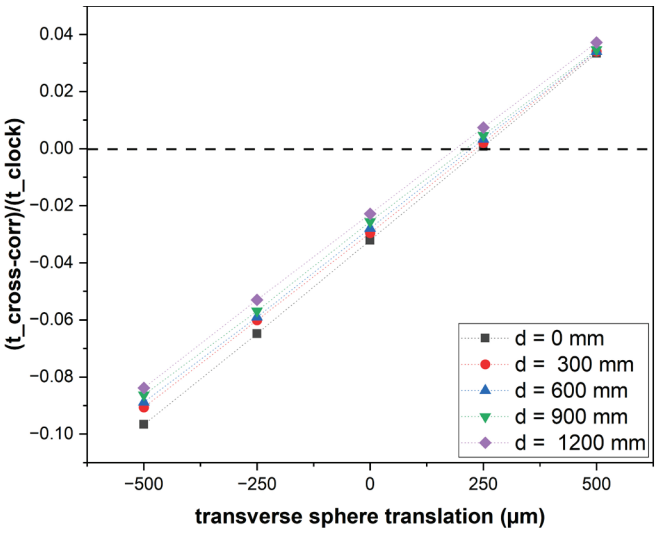

Figure 60. Calibration curves of the upgraded P3 device.

	Intercept				Slope				Statistics	
	Value	Standard Error	95% LCL	95% UCL	Value	Standard Error	95% LCL	95% UCL	R-Square (COD)	Adj. R-Square
t_cross-corr/t_clock	-0.03188	0.00015	-0.03237	-0.03139	0.00013	4.34407E-7	0.00013	0.00013	0.99997	0.99996
t_cross-corr/t_clock	-0.02884	0.00028	-0.02972	-0.02795	0.00012	7.85186E-7	0.00012	0.00013	0.99988	0.99984
	-0.02766	0.0002	-0.02829	-0.02703	0.00012	5.62239E-7	0.00012	0.00013	0.99994	0.99992
	-0.02588	0.00021	-0.02655	-0.02521	0.00012	5.93224E-7	0.00012	0.00012	0.99993	0.9999
	-0.02301	0.00014	-0.02346	-0.02255	0.00012	4.05074E-7	0.00012	0.00012	0.99997	0.99996

Table 8. Summary of the parameters calculated through linear fitting (target distances increasing from top to bottom) of the normalized cross-correlations.

The obtained values of the measurand $\frac{t_{cross-corr}}{t_{clock}}$ for all the 25 positions of the sphere were thence plotted, as shown in Figure 60, and the sought linear dependencies from the transverse sphere translations were deduced by least square fitting of the data (Table 8). Looking again at Figure 60, it is interesting to highlight two details: since the five curves have slightly different slopes, they seem to intersect in a region of space external to the calibration range (> 500 µm); secondly, what it is more important, there is the fact that each calibration curve shows a specific abscissa of transverse position corresponding to a null value of the cross-correlation (Figure 61).

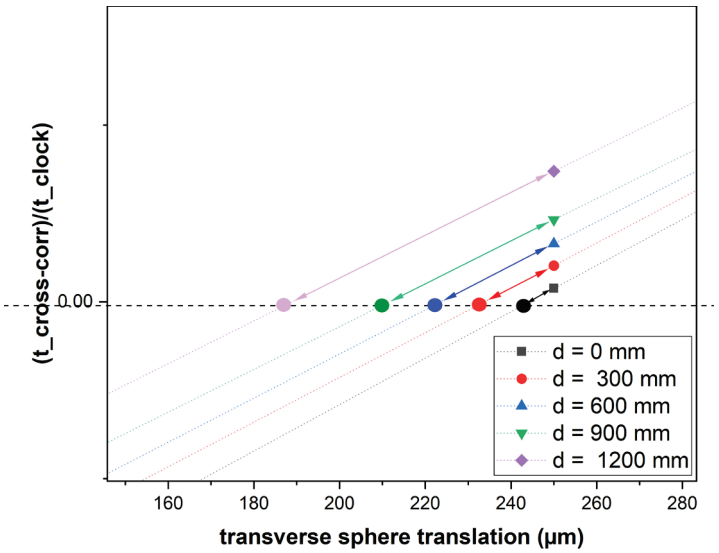

Figure 61. Magnification of plot in Figure 60 showing the behaviour of the calibration curves near the null ordinate value.

By inverting each calibration curve, extracting the abscissa at which $t_{cross-corr}$ has a null value and assuming that the corresponding transverse sphere translation ΔS_{sphere} is a linear function of the distance d of the sphere, a new linear equation can be deduced (fit parameters in Figure 62):

$$\Delta S_{sphere} = 246.35\ \mu m - 0.04\ \frac{\mu m}{mm} \cdot d$$

This relation expresses the amount of lateral displacement to be imposed to the target in order to keep the value of the cross-correlation of the photodiode signal null, exploring increasing distances of the same target from the device; reversing the perspective, this equation also quantifies the correction as a function of d to be applied to the position of (the support carrying) the slit, orthogonal to the backscattered beam, for the same condition to occur: through this analysis the extent of the intrinsic mechanical misalignment of the device was then estimated. Remembering that the initial alignment of the sphere in the beam was carried out in a qualitative way (looking at the best circular symmetry of the luminous halo of the sphere projected onto a rear screen, like in Figure 59), it turns out that the error made in the positioning of the target at its minimum distance is about a quarter of a millimeter, as it can be inferred from the same equation: something that makes perfect sense, since that procedure was performed with the maximum accuracy allowed by human eye. Another aspect that emerged from the data that deserves to be mentioned was the exponential decaying nature of the photodiode signal amplitudes, as a function of sphere distance and of its lateral displacement (Figure 63).

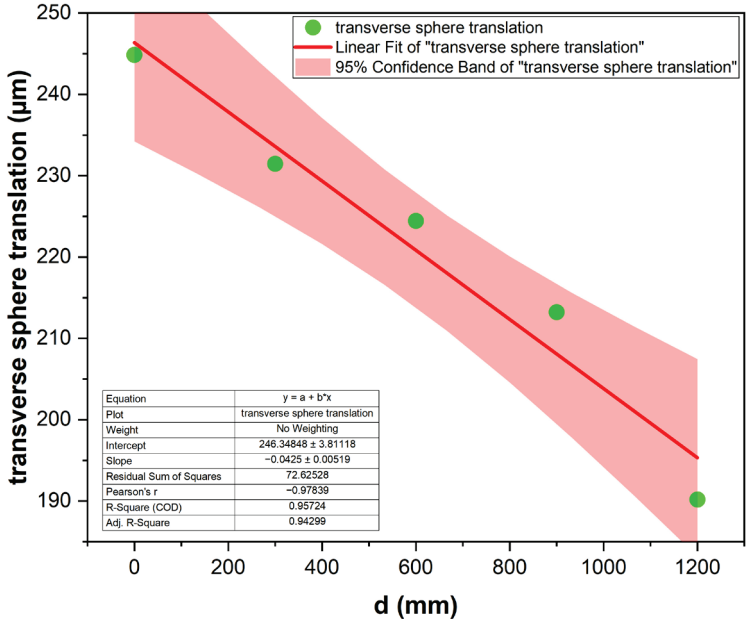

Figure 62. Linear fit to estimate the mechanical misalignment of the device.

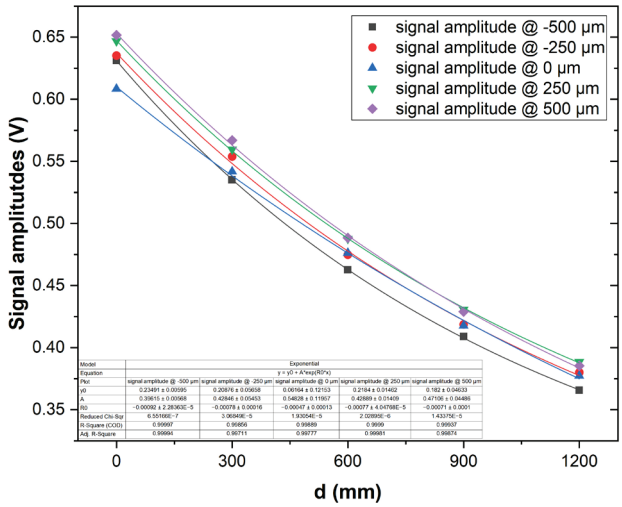

Figure 63. Photodiode signal amplitudes as a function of sphere distance and lateral displacement, and their exponential fit.

2.3.3 Straightness deviation estimation

Next step was aimed to the estimation of the indication error of the device, with the same strategy used in the context of the previous version of the device itself. 25 positions of the target were explored in the range (0 ÷ 1200) mm (with an initial offset of 470 mm because of the chosen installation layout), with the sphere moving along an almost ideal straight line traveled by the CMM X-carriage[9] (Figure 64, Figure 65).

[9] According to CMM error map, t_{xy} is within the range [-1 ÷ 0.4] µm.

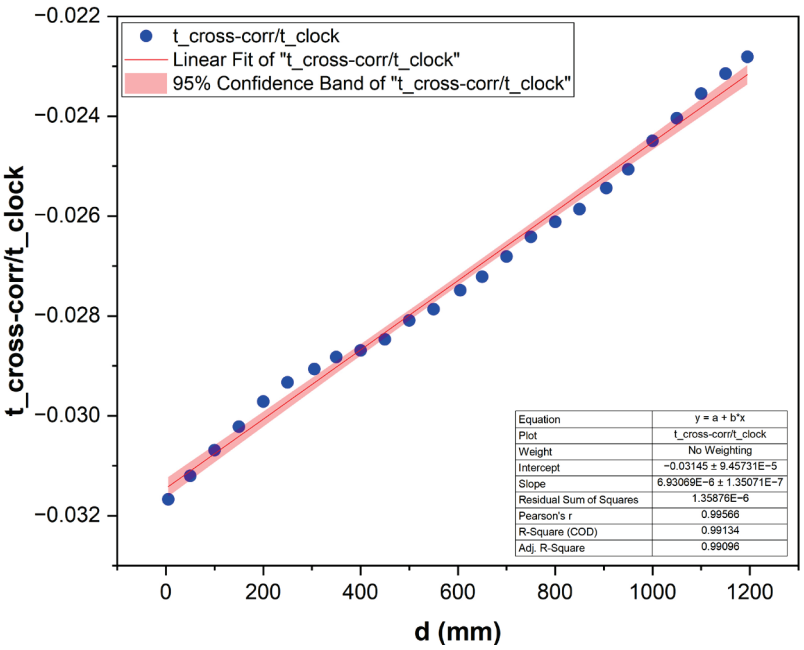

Figure 64. Linear fit of the normalized $t_{cross-corr}$ values in the 25 positions occupied by the sphere in its path along an ideal straight line.

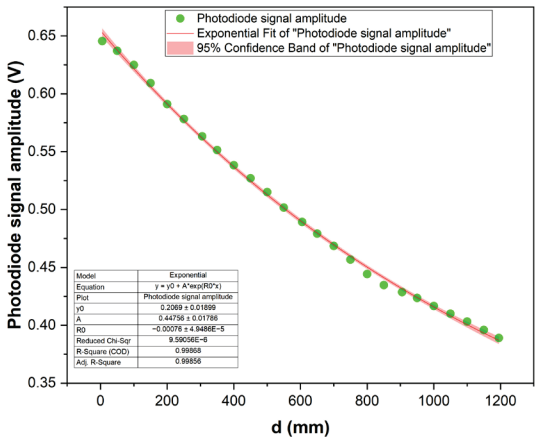

Figure 65. Exponential fit of the photodiode signal amplitude as a function of the distance of the sphere from the device

In order to quantify the maximum indication error of the device, the calibration parameters calculated before at only five distances were used to perform a linear interpolation to estimate the response of the device at the untested distances of the sphere; so, starting from the linear relation

$$t_{cross-corr,norm} = A + B \cdot \Delta S$$

with ΔS = transverse position of the sphere, by inverting this equation we get:

$$\Delta S = -\frac{A}{B} + \frac{t_{cross-corr,norm}}{B} = \alpha + \beta \cdot t_{cross-corr,norm}$$

where $[\alpha] = [\beta] =$ µm. Taking advantage of the fitting parameters already obtained by calibration (resumed in Table 9) and converted into the coefficients α and β (Table 10), it was easy to assemble a look-up table for the estimation of the

resulting straightness (Table 11), perform linear fit (Figure 66) and then plot the residuals of the linear fit (Figure 67); some simple statistics applied on the calculated residuals allowed to estimate the indication error of the device (its own straightness error, according to least square fitting) in 4.4 µm.

d / mm	**A**	**B** / µm^{-1}
0	-0.032	1.302E-04
300	-0.029	1.246E-04
600	-0.028	1.232E-04
900	-0.026	1.214E-04
1200	-0.023	1.209E-04

Table 9. Parameters of the calibration for upgraded P3.

α / µm	β / µm
244.818	7679.371
231.515	8027.551
224.475	8115.500
213.255	8240.151
190.247	8268.016

Table 10. Coefficients used for the interpolation.

d / mm	$\frac{t_{cross-corr}}{t_{clock}}$	p[10]	**STR "before"**[11] / µm	**STR "after"**[12] / µm	**STR res**[13] / µm	**residuals**[14] / µm
5	-0.032	0.017	1.622	-22.709	1.216	1.811
50	-0.031	0.167	5.230	-18.937	1.202	1.655
100	-0.031	0.333	9.180	-14.807	1.184	1.480
150	-0.030	0.500	12.786	-11.038	0.874	1.012
200	-0.030	0.667	16.660	-6.988	0.895	0.875
250	-0.029	0.833	19.601	-3.914	0.006	-0.172
305	-0.029	0.017	-1.770	-11.366	-1.930	-2.281
350	-0.029	0.167	0.168	-9.406	-1.428	-1.920
400	-0.029	0.333	1.221	-8.342	-1.967	-2.617
450	-0.028	0.5	3.016	-6.527	-1.756	-2.563
500	-0.028	0.667	6.047	-3.463	-0.293	-1.258
550	-0.028	0.833	7.847	-1.644	-0.062	-1.185
605	-0.027	0.017	1.429	-13.216	1.185	-0.111

[10] Interpolation factor; $p = \frac{d_{sphere} - d_{calibration,before}}{d_{calibration,\text{after}''} - d_{calibration,before}}$

[11] Straightness "before"; $STR_{before} = \alpha_{before} + \beta_{before} \cdot \frac{t_{cross-corr}}{t_{clock}}$

[12] Straightness "after"; $STR_{after} = \alpha_{after} + \beta_{after} \cdot \frac{t_{cross-corr}}{t_{clock}}$

[13] Resulting straightness; $STR_{res} = STR_{before}(1 - p) + p \cdot STR_{after}$

[14] Residuals of linear fit of "Resulting straightness" STR_{res}

650	-0.027	0.167	3.633	-10.979	1.198	-0.240
700	-0.027	0.333	6.922	-7.640	2.068	0.472
750	-0.026	0.500	10.122	-4.390	2.866	1.113
800	-0.026	0.667	12.566	-1.908	2.917	1.006
850	-0.026	0.833	14.615	0.172	2.579	0.511
905	-0.025	0.017	3.664	-20.052	3.269	1.027
950	-0.025	0.167	6.752	-16.955	2.801	0.417
1000	-0.024	0.333	11.445	-12.246	3.548	1.007
1050	-0.024	0.500	15.165	-8.513	3.326	0.628
1100	-0.024	0.667	19.233	-4.432	3.457	0.600
1150	-0.023	0.833	22.547	-1.106	2.837	-0.177
1195	-0.023	0.983	25.312	1.669	2.063	-1.093

Table 11. Results of the linear interpolation for the straightness evaluation of the collected data.

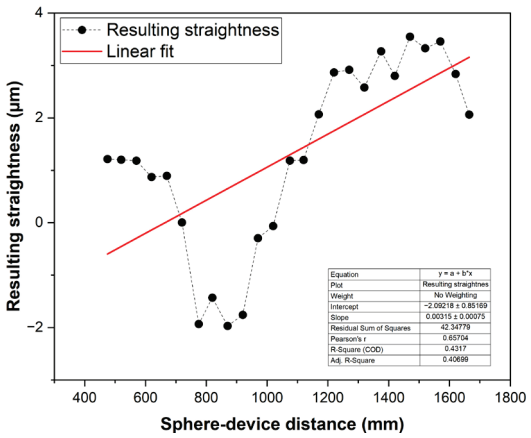

Figure 66. Calculated straightness by least square fitting of "STR res".

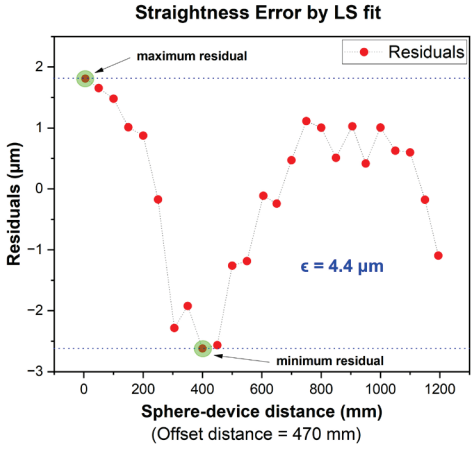

Figure 67. Straightness error calculated by least square fitting.

The calculation of the straightness error of the device by "end points" fit, using data collected in Table 12, led to a value of 5.1 µm (Figure 68). Besides, by implementing in a Python script the concept of the minimum zone found in

literature to get the height of the minimum area box (42) drawn around the convex hull (43) of the residuals of the least square fit, a smallest value of 4.1 µm was obtained (Figure 69); this quantity is comparable to the one extrapolated through the totally different experimental strategy described in Figure 34. Table 13 summarizes the values of the straightness deviation STRt calculated according to the three different strategies just explained.

A[15]	B[16] / µm	δ_i [17] / µm
7.116E-04	1.216E+00	-0.004
		-0.050
		-0.103
		-0.449
		-0.464
		-1.388
		-3.363
		-2.893
		-3.467
		-3.292
		-1.864
		-1.669
		-0.461
		-0.481
		0.354
		1.116
		1.131
		0.759
		1.409
		0.908
		1.620
		1.363
		1.458
		0.802
		-0.004

Table 12. Parameters used for evaluation of straightness error by "end points" fit.

[15] $A = \frac{STR_{res,last} - STR_{res,first}}{d_{sphere,last} - d_{sphere,first}}$

[16] $B = STR_{res,first}$

[17] $\delta_i = STR_{res} - \frac{A \cdot d_{sphere} + B}{\sqrt{1+A^2}}$

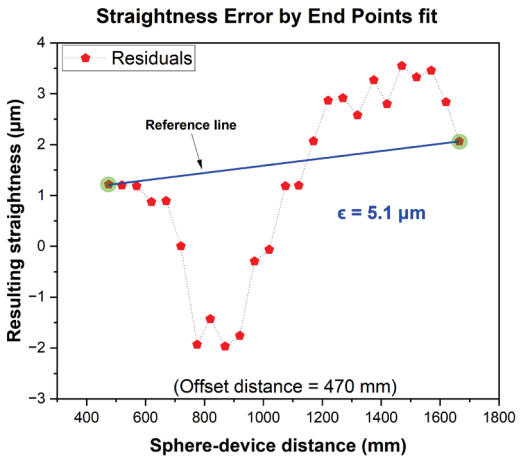

Figure 68. Straightness error of the device calculated according the End Points Fit strategy.

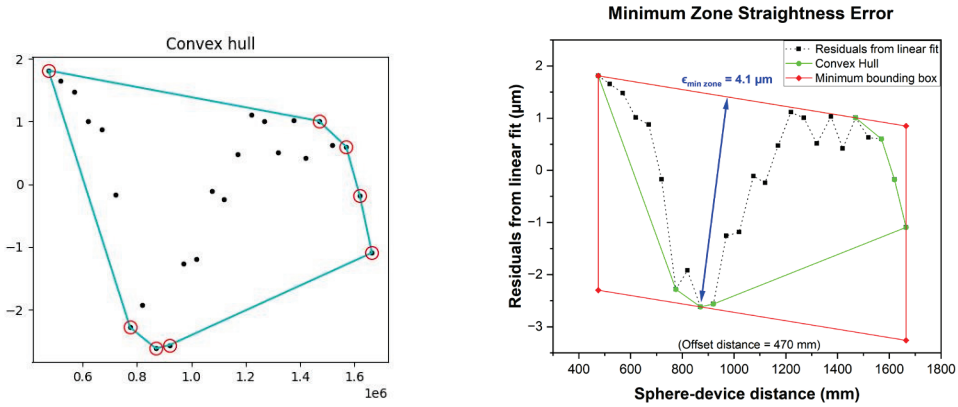

Figure 69. Plots showing the convex hull of the residuals of the least square fit (on the left), and minimum bounding box surrounding the residuals of the fit.

Reference line/ Strategy for calculation	Peak-to-valley straightness deviation (STRt) / µm
Least Squares	±2.2
End Points	±2.5
Minimum zone	±2.1

Table 13. Results of the peak-to-valley straightness deviation (STRt).

2.3.4 Straightness measurement of simulated path

Last test conducted in order to evaluate the performances of the device consisted in the estimation of the straightness deviation of the "path" of the same sphere in 25 sequential positions, sampling a full cycle of a sinusoid projected onto the same rectangle of 2D space used for the calibration. In order to do so, the chosen lateral

positions of the sphere were accurately imposed by using a translation stage with micrometer screws and measured from time to time with the TESA TESATRONIC TT60 LVDT with the resolution of 0.1 μm, and, statically at each elected position, the same acquisition strategy described for calibration was followed. Table 14 shows the results of the measurements, with the column "ΔS_{sphere}" labelling the effective lateral positions of the target as measured by LVDT.

d_{sphere} (mm)	ΔS_{sphere} (μm)	t_clock (ms)	σ_{t_clock}	t_cross-corr (ms)	$\sigma_{t\_cross\text{-}corr}$	t_cross-corr/t_clock	σ_{norm}	f_clock (Hz)	Δϕ (°)	Pearson
0	0.0	64.46	0.51%	-2.04	-1.05%	-0.032	-0.90%	15.51	-5.70	0.94
50	129.4	63.07	0.39%	-0.88	-2.12%	-0.014	-2.07%	15.86	-2.51	0.58
100	250.0	65.92	0.41%	0.12	15.54%	0.002	15.50%	15.17	0.34	0.29
150	353.6	66.52	0.34%	1.02	1.75%	0.015	1.77%	15.03	2.77	0.51
200	433.0	66.20	0.38%	1.71	1.12%	0.026	1.08%	15.11	4.66	0.66
250	483.0	66.15	0.42%	2.13	0.98%	0.032	0.87%	15.12	5.80	0.93
300	500.0	66.43	0.39%	2.28	0.94%	0.034	0.85%	15.05	6.19	0.78
350	483.0	65.81	0.51%	2.10	1.04%	0.032	0.93%	15.20	5.74	0.83
400	433.0	63.68	0.40%	1.63	1.13%	0.026	1.17%	15.70	4.62	0.56
450	353.6	63.86	0.41%	1.03	1.82%	0.016	1.81%	15.66	2.91	0.78
500	250.0	66.11	0.49%	0.21	9.37%	0.003	9.33%	15.13	0.58	0.31
550	129.4	66.05	0.32%	-0.77	-2.25%	-0.012	-2.19%	15.14	-2.10	0.45
600	0.0	66.27	0.43%	-1.84	-1.15%	-0.028	-1.06%	15.09	-4.99	0.73
650	-129.4	66.41	0.38%	-2.89	-0.82%	-0.043	-0.67%	15.06	-7.82	0.84
700	-250.0	66.01	0.33%	-3.86	-0.59%	-0.058	-0.49%	15.15	-10.52	0.90
750	-353.6	66.51	0.44%	-4.69	-0.82%	-0.071	-0.65%	15.03	-12.70	0.89
800	-433.0	66.47	0.43%	-5.28	-0.78%	-0.079	-0.61%	15.04	-14.30	0.94
850	-483.0	65.70	0.33%	-5.56	-0.64%	-0.085	-0.50%	15.22	-15.24	0.90
900	-500.0	63.68	0.15%	-5.47	-0.51%	-0.086	-0.48%	15.70	-15.47	0.66
950	-483.0	63.90	0.63%	-5.34	-0.89%	-0.084	-0.62%	15.65	-15.04	0.92
1000	-433.0	65.94	0.54%	-5.11	-0.67%	-0.078	-0.42%	15.17	-13.96	0.95
1050	-353.6	66.15	0.52%	-4.44	-0.87%	-0.067	-0.57%	15.12	-12.07	0.93
1100	-250.0	66.49	0.69%	-3.57	-0.90%	-0.054	-0.55%	15.04	-9.65	0.96
1150	-129.4	66.21	0.34%	-2.56	-0.81%	-0.039	-0.75%	15.10	-6.96	0.61
1200	0.0	65.65	0.43%	-1.51	-1.39%	-0.023	-1.31%	15.23	-4.14	0.62

Table 14. Results of the straightness measurement of the sphere sampling a sinusoid projected onto a plane parallel to XY coordinate plane.

Since we sampled the explored longitudinal range of (0 ÷ 1200) mm in more points than the ones available from calibration, in order to express the dependance of the normalized cross-correlation both on the longitudinal distance and on the lateral displacement a least square fitting with a 2 variables function was performed; in the absence of a suitable mathematical model to be guided by, with the aim of statistically managing the calculated values, the choice fell on a two-dimensional polynomial function:

$$z = z_0 + ax + by + cx^2 + dy^2 + fxy$$

By replacing x, y and z respectively with ΔS_{sphere}, d_{sphere} and $\frac{t_{cross-corr}}{t_{clock}}$, the 25 values of the available normalized cross-correlations were fitted, with the results reported in the plot shown in Figure 70; having thereby quantified the parameters of the polynomial function, it was easy to reverse the equation in order to solve it with respect to ΔS_{sphere}:

$$\Delta S_{sphere} = \frac{-(f d_{sphere} + a) + \sqrt{(f d_{sphere} + a)^2 - 4c\left(z_0 - \frac{t_{cross-corr}}{t_{clock}} + b d_{sphere} + d \cdot {d_{sphere}}^2\right)}}{2c}$$

In this way, we can rely on a relation expressing the expected values of the lateral displacement of the sphere on the basis of the *a priori* knowledge of cross-correlation values of the photodiode signal and the exact longitudinal distance of the sphere itself (with ΔS_{true} and $\frac{t_{cross-corr}}{t_{clock}}$ almost perfectly in phase, as shown in Figure 71). Expected values of lateral displacements of the target as a function of sphere distance and photodiode signals were collected in Table 15, and the differences ϵ between the expected and true values were plotted in Figure 72, with an overall *indication error* $\varepsilon_{res} = max(\epsilon) - min(\epsilon) = 14.1$ µm .

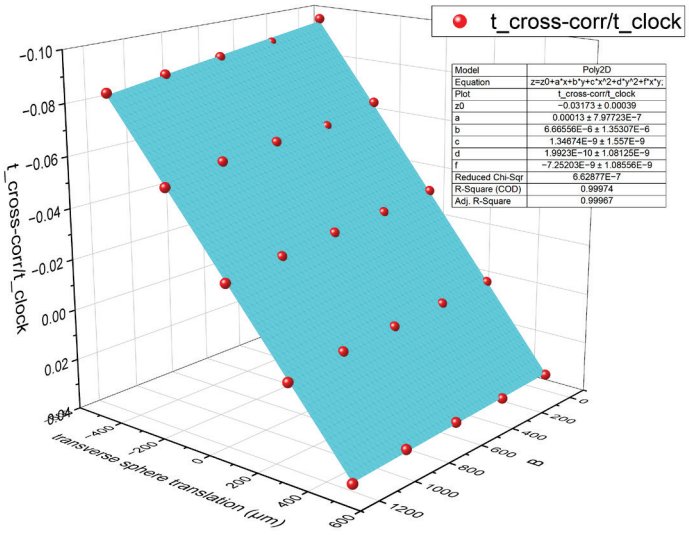

Figure 70. Polynomial surface fit of the 25 calibration points.

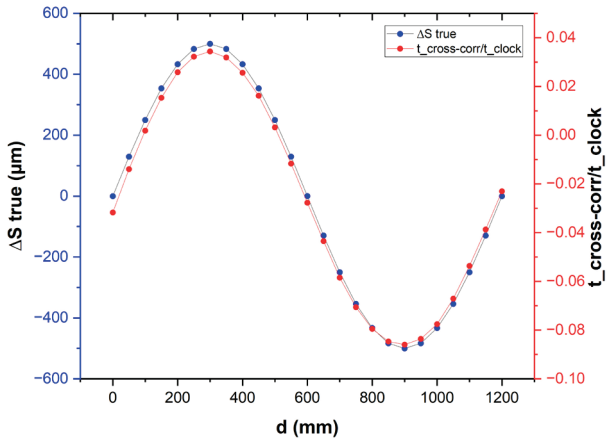

Figure 71. Plot showing the good phase correlation ($\Delta\varphi \cong 0.05$ rad) between the true lateral displacements of the target and the normalized cross-correlations of the photodiode signal.

ΔS expected / µm	**ΔS true** / µm	**difference ε** /µm
0.4	0.0	0.4
136.1	129.4	6.7
257.2	250.0	7.2
360.6	353.6	7.0
441.0	433.0	8.0
489.5	483.0	6.6
505.1	500.0	5.1
484.4	483.0	1.4
433.7	433.0	0.7
357.1	353.6	3.5
252.1	250.0	2.1
131.2	129.4	1.8
-0.4	0.0	-0.4
-130.7	-129.4	-1.3
-256.1	-250.0	-6.1
-358.7	-353.6	-5.2
-436.0	-433.0	-2.9
-482.9	-483.0	0.0
-497.9	-500.0	2.1
-482.8	-483.0	0.1
-436.9	-433.0	-3.9
-353.7	-353.6	-0.1
-245.4	-250.0	4.6
-124.0	-129.4	5.4
3.7	0.0	3.7

Table 15. Expected and true values of lateral displacements of the target.

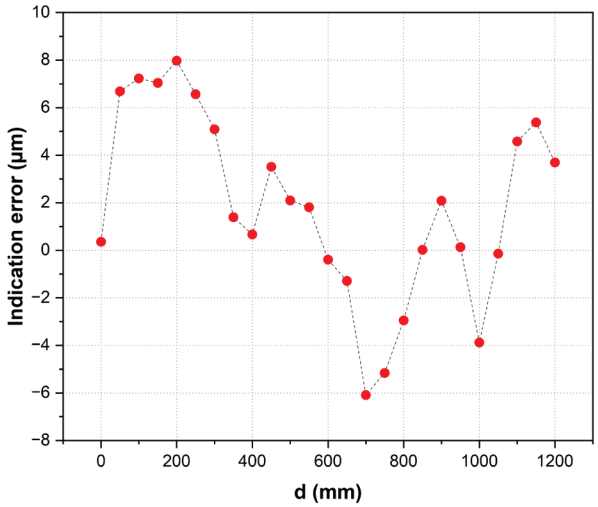

Figure 72. Indication error of the device in the range $(-500, 500)$ µm × $(0,1200)$ mm (with the usual longitudinal offset of 470 mm to be added to the horizontal scale).

2.3 Conclusions

At the end of this thesis work, three different versions of a device for measuring the 1D straightness of a path in space were designed, realized and tested; the design principles were based on a totally new concept, with a special glass sphere used as a target of a laser beam impinging on it, to be placed on the profile where the measurement is intended to be carried out. The driving principle is the mechanical modulation of the backscattered beam, which allows micrometric detection of the beam center and, consequently, of the lateral target position. The device was characterized up to a distance of ~1.7 m, taking advantage of a high accuracy CMM for the fine positioning of the target. A maximum indication error of ±2.1 μm was demonstrated, together with a good linearity of its response over a ±0.5 mm measuring interval and a peak-to-peak indication error of ±7 μm on a straightness measurement over a sinusoidal virtual path. The overall dimensions of the instrument are (300 × 300 × 175) mm^3: its size is quite compact to be used as a portable device to measure straightness of real machined profiles, and is prone to be further miniaturized. In order to be effectively installed onboard a machine tool, some improvements are foreseen in future work:

- The alignment procedure of the slit with respect to the reflected beam should be refined, and the addition of a stage for micrometric positioning of the assembly supporting the slit should be contemplated; although the target pointing was satisfactory (with the halo "perfectly" centered on the sphere shadow), the two peak signals detected by the photodiode were not equidistant (at the resolution allowed by the DAQ acquisition system). An improvement of the alignment procedure is expected to refine the calibration curves behaviour shown in Figure 60, reducing their spread.
- The instrument was calibrated and tested only up to a distance less than 2 m, whereas a longest range (up to ~3 m) is of interest for industrial applications in the machine tools context. In order to express its potential, the instrument should be calibrated and tested in a larger facility; the air turbulence, as it is known, is a factor affecting the accuracy and the repeatability of contactless measurements (especially at significative distances), but strategies can be implemented to face the drawbacks connected to conducting experiments in non-cooperative environments. Hopefully, keeping in mind the characteristics of the signal backscattered form the sphere (32), the capabilities of the instrument can be pushed up to ≃ 3 m without losing too much resolution with respect to the current best configuration; for longer distances, significant changes to the opto-mechanical set up must be evaluated in order to deal with the diverging beam returning from the sphere.
- The instrument is designed to be sensitive to one direction only, e.g., to the straightness deviation as projected in a horizontal plane, but the straightness of a 3D path should be fully evaluated in two dimensions by projecting it onto a plane; this is achievable, in principle, by rotating the device 90° and repeating

the procedure. This is a limitation due to the choice of a modulating the signal by an oscillating slit, which is difficult to extend to two dimensions. This restriction could be overcome by a totally different strategy for the mechanical modulation. Moreover, in a context where the intended use of the device is mainly “1-D”, the possibility of replacing the ball lens with another type of retroreflector should be investigated: in this case, in fact, the main advantage of the sphere —the possibility to sense it over almost the entire solid angle— is only partially exploited: a corner cube could, in principle, be fit for the purpose, at the expense of redesigning the whole strategy of signal processing.

References

1. ISO 12780-1:2011. *Geometrical Product Specification (GPS)—Straightness—Part 1: Vocabulary and Parameters of Straightness.* Geneva, Switzerland : s.n., 2011.

2. *Straightness measurement of large machine guideways.* Ptaszynski, W., et al. 2011, Metalurgija, Vol. 50, p. 281–284.

3. *Evaluation of straightness and flatness tolerances using the minimum zone.* Mark T. Traband, Sanjay Joshi, Richard A. Wysk, Tom M. Cavalier. 3, 1989, Manufacturing review, Vol. 2, p. 189-195.

4. *An exact minimum zone solution for three-dimensional straightness evaluation problems.* Huang, Jyunping. 3, 1999, Precision Engineering, Vol. 23, p. 204-208.

5. *Genetic algorithm-based form error evaluation.* Cui, Changcai & Li, Bing & Huang, Fugui & Zhang, Rencheng. 2007, Measurement Science and Technology.

6. *Particle swarm optimization.* Eberhart, J. Kennedy and R. Perth, WA, Australia : s.n., 1995. ICNN'95 - International Conference on Neural Networks.

7. *Non-contacting straightness measurement to nanometre accuracy.* Virdee, M.S. 1995, International Journal of Machine Tools and Manufacture, Vol. 35, p. 157-164.

8. *Measurement of straightness error of machine guideways using autocollimator.* Ankit, R. Vaishnani. 2019, Journal of Emerging Technologies and Innovative Research, Vol. 6, p. 76-81.

9. *Straightness measurements for accelerator structures.* Schwarz, W. Tsukuba, Ibaraki 14–17 November 1995 : National Laboratory for High Energy Physics, 1996. International Workshop on Accelerator Alignment. p. 477-490.

10. Raghavendra, N.V. e Krishnamurthy, L. *Engineering Metrology and Measurements.* Oxford : Oxford University Press, 2013.

11. *A Straightness Error Compensation System for Topography Measurement Based on Thin Film Interferometry.* Su, H., et al. 2021, Photonics , Vol. 8.

12. *A Method for Measurement of Workpiece form Deviations Based on Machine Vision.* Zhang, W., et al. 2022, Machines, Vol. 10.

13. Elshennawy, A.K. e Jing, F.-S. *A Simple Method for Measuring Straightness of Coordinate Measuring Machines.* National Institute of Standards and Technology. Gaithersburg : National Bureau of Standards, 1988.

14. *Reversal technique applied to the measurement of straightness errors.* Di Giacomo, B., de Magalhães, R.D.C.A. e Paziani, F.T. São Paulo, Brazil : s.n., 2003. 17th International Congress of Mechanical Engineering.

15. *Exact straightness reconstruction for on-machine measuring precision workpiece.* Yin, Z.-Q. e Li, S.-Y. 4, 2005, Precision Engineering, Vol. 29, p. 456-466.

16. *Heterodyne interferometric system with subnanometer accuracy for measurement of straightness.* Wu, Chien-ming. 19, 2004, Applied Optics, Vol. 43, p. 3812-3816.

17. *Development of a straightness measurement and compensation system with multiple right-angle reflectors and a lead zirconate titanate-based compensation stage.* Chien-Hung Liu, Jui-Hung Chen, Yun-Feng Teng. 11, 2009, Review of Scientific Instruments, Vol. 80.

18. *Two-dimensional straightness measurement based on optical knife-edge sensing.* Chen Wang, Fenghe Zhong, Jonathan D. Ellis. 9, 2017, Review of Scientific Instruments, Vol. 88.

19. *A novel laser straightness measurement method with beam bend compensation.* Fengling You, Bin Zhang, Qibo Feng. 17, 2011, Optik, Vol. 122, p. 1530-1534.

20. *A New Method for On-line Measurement of the Straightness Error of Machine Tools Using an Acceleration Sensor.* Kuo Liu, Yiming Cui, Zhisong Liu et al. 2021.

21. LUMINAR—Large Volume Metrology in Industry. [Online] https://www.euramet.org/research-innovation/search-research-projects/details/?tx_eurametctcp_project[project]=1159&tx_eurametctcp_project[controller]=Project&tx_eurametctcp_project[action]=show.

22. *Cartesian approach to large scale coordinate measurement: InPlanT.* Pisani, M., Balsamo, A. e Francese, C. Tsukuba, Japan : s.n., 2014. 11th IMEKO Symposium LMPMI2014 (Laser Metrology for Precision Measurement and Inspection in Industry).

23. LaVA—Large Volume Metrology Applications. [Online] https://www.euramet.org/research-innovation/search-research-projects/details/project/large-volume-metrology-applications.

24. ISO 230-2:2014. *Test code for machine tools — Part 2: Determination of accuracy and repeatability of positioning of numerically controlled axes.* 2014.

25. *Error Compensation of Coordinate Measuring Machines.* G. Zhang, R. Veale, T. Charlton, B. Borchardt, R. Hocken. 1, 1985, CIRP Annals, Vol. 34.

26. *Three Dimensional Metrology.* R. Hocken, J.A. Simpson, B. Borchardt, J. Lazar, C. Reeve, P. Stein/R. Young. 1977, CIRP Annals.

27. *Effects of Arbitrary Coefficients of CMM Error Maps on Probe Qualification.* Balsamo, A. 1, 1995, CIRP Annals, Vol. 4.

28. *Geometric Error Measurement and Compensation of Machines.* S. Sartori, G.X. Zhang. 2, 1995, CIRP Annals, Vol. 44.

29. Balsamo, A. Parameter intrinsic identifiability of error models: the case of geometrical errors of CMMS. [aut. libro] M. G. Cox, E. Filipe, F. Pavese, D. Richter P. Ciarlini. *Advanced Mathematical and Computational Tools in Metrology V.* Singapore : s.n., 2001, p. 392.

30. —. *Mappe d'errore di CMM a corpo rigido: teoria, trasformazioni e gradi di libertà.* INRIM. 2014.

31. Egidi, A. *Attenuation of back-scattered optical signals by off-axis and variable aperture slits–A simulation.* INRIM. 2021.

32. *High-Index Glass Ball Retroreflectors for Measuring Lateral Positions.* Egidi, A., Balsamo, A. e Pisani, M. 5, 2019, Sensors, Vol. 19.

33. *Investigation on Modulation-Based Straightness Measurement.* Egidi, A., et al. 6, s.l. : MDPI, 2023, Sensors, Vol. 23.

34. Myszka, David H. *Machines & Mechanisms: Applied Kinematic Analysis.* s.l. : Pearson College Div, 2012.

35. *Kinematics and Load Formulation of Engine Crank.* Nigus, Hailemariam. 2015, Mechanics, Materials Science & Engineering Journal.

36. *Evaluation of straightness and flatness error using computational geometric techniques.* Samuel, G. e Shunmugam, M. 13, 1999, Computer-Aided Design, Vol. 31.

37. Hancock, Johnnie. Jitter—Understanding it, Measuring It, Eliminating It Part 1: Jitter Fundamentals. [Online] 2004. https://www.highfrequencyelectronics.com/Apr04/HFE0404_Hancock.pdf.

38. Understanding and Characterizing Timing Jitter. *www.tektronix.com.* [Online] 2012. https://download.tek.com/document/55W_16146_5_MR_Letter.pdf.

39. Measuring Jitter in Digital Systems. [Online] 2008. https://people.ece.ubc.ca/robertor/Links_files/Files/Application_Note_1448-1.pdf.

40. Peak-to-Peak Jitter Calculations. [Online] https://www.renesas.com/us/en/document/apn/838-peak-peak-jitter-calculations.

41. RMS to Peak-peak Jitter Calculator. [Online] https://www.sitime.com/rms-peak-peak-jitter-calculator.

42. Rusnack, William. MinimumBoundingBox. [Online] 2016. https://bitbucket.org/william_rusnack/minimumboundingbox/src/master/.

43. Gherman, Dinu. Finding the convex hull of a set of 2D points (Python recipe) . *ActiveState.* [Online] 2001. https://code.activestate.com/recipes/66527/.

44. ISO 230 1:2012. *Test code for machine tools — Part 1: Geometric accuracy of machines operating under no-load or quasi-static conditions.* 2012.

Appendix A

- Python code written to extract the periods of the clock signals:

```
# coding=utf-8
import pandas as pd
from scipy.signal import find_peaks
import matplotlib.pyplot as plt
import numpy as np
import numpy
from scipy.ndimage import gaussian_filter1d
import glob
import os
from alive_progress import alive_bar

path = "D:/INRiM/LaVa/Acquisizioni/Picoscope biella-
manovella/set up compatto presso CMM/stabilità motore/5-6-
23/2047 waveforms_10 kS,10 us/20230605-0001"
csv_files = glob.glob(os.path.join(path, "*.csv"))

start = -45
stop = 45

f_poq = open('periodi_oq.txt', 'w')

with alive_bar(len(csv_files)) as bar:
    for i, f in enumerate(csv_files):
        data = pd.read_csv(f, delimiter=';', low_memory=False)
        data_new = data.iloc[3:]
        df = pd.DataFrame(data_new, columns=['Tempo', 'Canale
A', '-(B)'])
        tempi = np.array(df['Tempo'].values, dtype=float)
        ampiezze_clock = np.array(df['Canale A'].values,
dtype=float)
        segnale_digit = np.array(np.transpose([tempi,
ampiezze_clock]))

        segnale_clock_tronc = segnale_digit[(tempi >= start) &
(tempi <= stop)]
        tempi_tronc = segnale_clock_tronc[:, 0]
        ampiezze_clock_tronc = segnale_clock_tronc[:, 1]

        inv_x = -
np.gradient(gaussian_filter1d(segnale_clock_tronc[:, 1], 5
        peaks, _ = find_peaks(inv_x,
height=0.8*np.max(np.abs((inv_x))))
        pos_max = np.take(tempi_tronc, peaks)

        delta_t = np.abs(numpy.diff(pos_max))
        print(delta_t)

        try:
            print(delta_t[0], file=f_poq)

        except IndexError:
            print(f'File {i} skipped/n'
```

```
        bar()

f_poq.close()

periodi_clock = np.loadtxt('periodi_oq.txt')
plt.figure()
plt.plot(periodi_clock, marker='o', linestyle='dashed',
linewidth=2, markersize=12)
plt.title("periodi del segnale digitale")
plt.ylabel('tempo (ms)')
plt.show()

periodo_clock_medio = np.average(periodi_clock)
sigma_clock = np.std(periodi_clock)
print('periodo clock medio in ms =',
np.round(periodo_clock_medio, 3))
print('sigma periodo clock in ms =', np.round(sigma_clock, 3))
```

- Python code written to calibrate the InPlanT device and estimate its indication error:

```
# coding=utf-8
import pandas as pd
from scipy.signal import find_peaks
import matplotlib.pyplot as plt
import numpy as np
import numpy
from scipy.ndimage import gaussian_filter1d
import glob
import os
from alive_progress import alive_bar
import scipy.signal
import scipy.stats
from scipy.signal import savgol_filter

path = "D:/INRiM/LaVa/Acquisizioni/Picoscope biella-
manovella/set up compatto presso CMM/misure LaVA_29-5-23/misura
finale di rettilineità/d = 1200 mm_0 um/20230529-0004"
csv_files = glob.glob(os.path.join(path, "*.csv"))

start = -45  # istante iniziale per lo studio, in ms. Aprire
prima il file csv per capire dove troncare (devono starci solo 3
picchi interi del segnale del fotodiodo)
stop = 45  # istante finale

def lag_finder(picco_sinistro, picco_centrale, picco_destro):
    nsamples = len(picco_centrale)
    delay_arr = numpy.linspace(-tempi_tronc[-1], tempi_tronc[-
1], nsamples)

    correlation_sin = scipy.signal.correlate(picco_sinistro,
picco_centrale, mode='same') / np.sqrt(
        scipy.signal.correlate(picco_sinistro, picco_sinistro,
mode='same')[int(nsamples / 2)] *
scipy.signal.correlate(picco_centrale, picco_centrale,
mode='same')[int(nsamples / 2)])
```

```
    correlation_dx = scipy.signal.correlate(picco_destro,
picco_centrale, mode='same') / np.sqrt(
        scipy.signal.correlate(picco_centrale, picco_centrale,
mode='same')[int(nsamples / 2)] *
scipy.signal.correlate(picco_destro, picco_destro,
mode='same')[int(nsamples / 2)])

    delay_1 = delay_arr[np.argmax(correlation_sin)]
    print('picco sinistro è ' + str(delay_1) + ' ms sfasato
rispetto a picco centrale')
    delay_2 = delay_arr[np.argmax(correlation_dx)]
    print('picco destro è ' + str(delay_2) + ' ms sfasato
rispetto a picco centrale')
    delay = delay_1 + delay_2
    return delay

# creo 3 files in cui andrò a scrivere man mano le quantità di
mio interesse:
max_segnali = open('max_segnali.txt', 'w')
f_cc = open('crosscorr.txt', 'w')
f_poq = open('periodi_oq.txt', 'w')


with alive_bar(len(csv_files)) as bar: # genera una barra che
mostra l'avanzamento nel processamento dei files
    for i, f in enumerate(csv_files):
        # read the csv file
        data = pd.read_csv(f, delimiter=';', low_memory=False)
        data_new = data.iloc[3:] # non considero le prime 3
righe del csv
        df = pd.DataFrame(data_new, columns=['Tempo', 'Canale
A', '-(B)'])
        tempi = np.array(df['Tempo'].values, dtype=float)
        ampiezze_clock = np.array(df['Canale A'].values,
dtype=float) # il trigger del Picoscope deve stare sul fronte di
salita del segnale dello switch ottico!
        ampiezze_fotodiodo= np.array(df['-(B)'].values,
dtype=float)
        segnale_digit = np.array(np.transpose([tempi,
ampiezze_clock]))
        segnale_fotodiodo= np.array(np.transpose([tempi,
ampiezze_fotodiodo]))

        segnale_clock_tronc = segnale_digit[(tempi >= start) &
(tempi <= stop)]  # acquisizione max è di 100 ms
        segnale_fotodiodo_tronc = segnale_fotodiodo[(tempi >=
start) & (tempi <= stop)]
        tempi_tronc = segnale_clock_tronc[:, 0]
        ampiezze_clock_tronc = segnale_clock_tronc[:, 1]
        ampiezze_fotodiodo_tronc = segnale_fotodiodo_tronc[:, 1]

        inv_x = -
np.gradient(gaussian_filter1d(segnale_clock_tronc[:, 1], 5))  #
derivo il segnale dopo aver fatto un po' di smoothing e poi ne
cambio il segno (sono sui fronti discendenti del clock!)
        peaks, _ = find_peaks(inv_x,
height=0.8*np.max(np.abs((inv_x))))  # considera solo i picchi
più alti in modulo della quantità specificata (pari all' 80% del
massimo del segnale).
```

```
        pos_max = np.take(tempi_tronc, peaks) #  restituisce i
tempi associati alle posizioni dei massimi (ovvero dei minimi):
        #print('N° cicli interi contenuti in intervallo
temporale scelto:', len(pos_max)/2)

        # ricavo gli intervalli temporali fra i fronti di
salita:
        delta_t = np.abs(numpy.diff(pos_max))

        segnale_max = np.max(ampiezze_fotodiodo_tronc)
        print("massimo del segnale, in V:", segnale_max)
        # faccio due sogliature sul segnale del fotodiodo a %
arbitrarie dell'ampiezza massima per eliminare il rumore in
basso e in alto, in 2 passaggi:
        threshold_low = 0.1 # soglia in basso
        threshold_high = 0.9 # soglia in alto
        segnale_thresholded_low =
np.where(ampiezze_fotodiodo_tronc <= threshold_low *
segnale_max, 0,
ampiezze_fotodiodo_tronc) # in basso soglio ad una % pari a
threshold_low * 100, tenendo conto dei casi dove c'è più rumore
        # (quando i picchi si avvicinano troppo l'uno all'altro
serve infatti una % molto più alta)
        segnale_thresholded_high =
np.where(ampiezze_fotodiodo_tronc >= threshold_high *
segnale_max, threshold_high * segnale_max,

ampiezze_fotodiodo_tronc) # in alto, ad una % pari a
threshold_high * 100
        segnale_thresholded = np.where(ampiezze_fotodiodo_tronc
<= threshold_low * segnale_max, segnale_thresholded_low,
                                       segnale_thresholded_high)
# combino le due sogliature in basso e in alto, generando un
segnale sintetico di forma trapezoidale e quasi simmetrico

        # devo ora separare i 3 picchi in 3 file diversi,
ciascuno contenente un solo picco.
        # Per farlo, identifico la posizione di ciascun picco (è
solo di servizio...non interviene nei calcoli successivi):
        x = segnale_thresholded
        peaks_fotodiodo, _ = find_peaks(x, width=100)
        value = np.take(x, peaks_fotodiodo)
        # trovo le posizioni temporali dei 3 picchi (su segnale
non sogliato):
        ascisse_temp = np.take(segnale_clock_tronc[:, 0],
peaks_fotodiodo)

        # genero quindi ora 3 file con un picco ciascuno,
tenendo conto della posizione dei picchi trovati sopra:
        # (sulla base della larghezza temporale dei picchi, che
alla frequenza circa 13 Hz è di circa 20 ms);
        # a frequenze più alte del motore, i picchi sono più
stretti

        larghezza_picco = 20 # ms, (sovrastimata) VERIFICARE
ogni volta!
        picco_sinistro = np.where(tempi_tronc <=
(ascisse_temp[0] + larghezza_picco / 2), segnale_thresholded, 0)
        picco_centrale = np.where(
            (tempi_tronc > ascisse_temp[1] - larghezza_picco /
2) & (tempi_tronc <= ascisse_temp[1] + larghezza_picco / 2),
```

```
            segnale_thresholded, 0)
        picco_destro = np.where(tempi_tronc > (ascisse_temp[2] -
larghezza_picco / 2), segnale_thresholded, 0)

        crosscorr_ris = lag_finder(picco_sinistro,
picco_centrale, picco_destro)

        try:
            print(segnale_max, file=max_segnali)
            print(delta_t[0], file=f_poq)
            print(crosscorr_ris, file=f_cc)
        except IndexError:
            print(f'File {i} skipped/n')

        bar()

f_cc.close()
f_poq.close()
max_segnali.close()

massimi = np.loadtxt('max_segnali.txt')
media_massimi = np.average(massimi)

periodi_clock = np.loadtxt('periodi_oq.txt')
plt.figure()
plt.plot(periodi_clock, marker='o', linestyle='dashed',
linewidth=2, markersize=12)
plt.title("periodi del segnale digitale")
plt.ylabel('tempo (ms)')
plt.show()

periodo_clock_medio = np.average(periodi_clock)
sigma_clock = np.std(periodi_clock)
print('periodo clock medio in ms =',
np.round(periodo_clock_medio, 3))
print('sigma periodo clock in ms =', np.round(sigma_clock, 3))

crosscorr = np.loadtxt('crosscorr.txt')
plt.figure()
plt.plot(crosscorr, marker='o', linestyle='dashed', linewidth=3,
markersize=15)
plt.title("entità cross-correlazioni picchi")
plt.ylabel('tempo (ms)')
plt.show()

crosscorr_media = np.average(crosscorr)
sigma_crosscorr = np.std(crosscorr)
print('entità cross-correlazione media, in ms =',
np.round(crosscorr_media, 3))
print('sigma cross-correlazione, in ms =',
np.round(sigma_crosscorr, 3))

norm = np.abs(crosscorr/periodi_clock)
np.savetxt("cross correlazioni normalizzate su clock.txt", norm)
norm_media = np.average(norm)
sigma_norm = np.std(norm)

frequenza_onda_quadra_media = 1000*(1./periodo_clock_medio)
print("il motore gira in media a",
np.round(frequenza_onda_quadra_media, 3), "Hz")
periodo_segnale_sfera = periodo_clock_medio/2.
```

```
print("periodo medio segnale sfera =",
np.round(periodo_segnale_sfera, 3), "ms")
fase_angolare_media = np.degrees(np.pi *
crosscorr_media/periodo_clock_medio)
print("sfasamento angolare medio sfera rispetto a clock =",
np.round(fase_angolare_media, 3), "gradi")

savgol_clock = savgol_filter(periodi_clock, window_length=25,
polyorder=3)

savgol_crosscorr = np.abs(savgol_filter(crosscorr,
window_length=25, polyorder=3))

np.savetxt("clock smoothed.txt", savgol_clock)
np.savetxt("crosscorr smoothed.txt", savgol_crosscorr)

clock_norm = (savgol_clock-
np.min(savgol_clock))/(np.max(savgol_clock)-
np.min(savgol_clock))
savgol_norm = (savgol_crosscorr-
np.min(savgol_crosscorr))/(np.max(savgol_crosscorr)-
np.min(savgol_crosscorr))
np.savetxt("clock smoothed + norm.txt", clock_norm)
np.savetxt("crosscorr smoothed + norm.txt", savgol_norm)

pearson, p = scipy.stats.pearsonr(clock_norm, savgol_norm)
print('coefficiente di Pearson =', np.round(pearson, 3))

np.savetxt("parametri di interesse.txt", (media_massimi,
periodo_clock_medio, sigma_clock, crosscorr_media,
sigma_crosscorr, norm_media, sigma_norm,
frequenza_onda_quadra_media, fase_angolare_media, pearson))
```

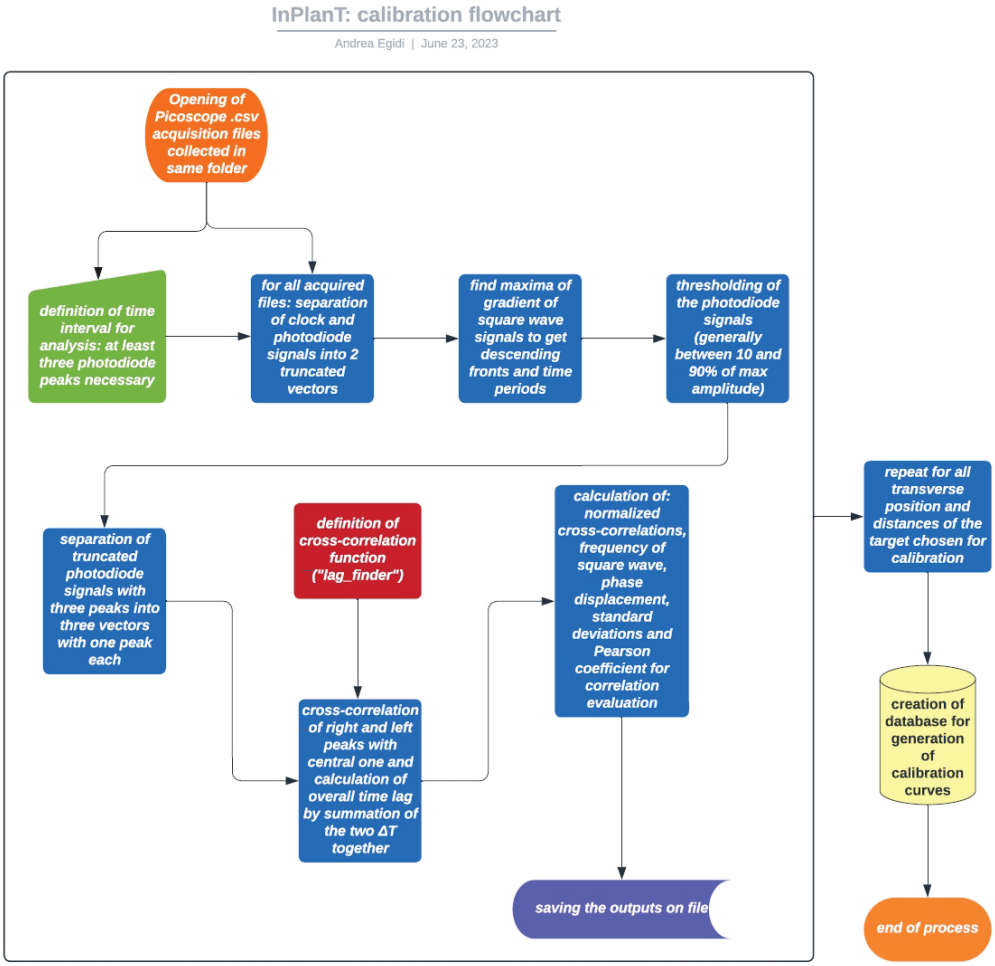

Figure 73. Flowchart illustrating the Python script used for the calibration of the device.